Violence and volume:

an experimental study of CO_2 driven eruptions of Colli Albani

Dissertation

zur Erlangung des mathematisch-naturwissenschaftlichen Doktorgrades

„Doctor rerum naturalium“

der Georg-August-Universität Göttingen

im Promotionsprogramm Geowissenschaften

der Georg-August University School of Science (GAUSS)

vorgelegt von

Christin Kleest

aus Schwedt (Oder), Deutschland

Göttingen, 2021

Betreuungsausschuss

Prof. Dr. Sharon Webb	Abteilung Mineralogie Geowissenschaftliches Zentrum Göttingen Georg-August-Universität Göttingen
Dr. Sara Fanara	Abteilung Mineralogie Geowissenschaftliches Zentrum Göttingen Georg-August-Universität Göttingen
Dr. Kirsten Techmer	Abteilung Mineralogie Geowissenschaftliches Zentrum Göttingen Georg-August-Universität Göttingen

Mitglieder der Prüfungskommission

Referentin:

Prof. Dr. Sharon Webb	Abteilung Mineralogie Geowissenschaftliches Zentrum Göttingen Georg-August-Universität Göttingen

Korreferent:

Prof. Dr. Max Wilke	Institut für Geowissenschaften AG Mineralogie, Universität Potsdam

Weitere Mitglieder der Prüfungskommission:

Prof. Dr. rer. nat. Francois Holtz	Institut für Mineralogie AG Petrologie, Leibniz Universität Hannover
apl. Prof. Dr. Harald Behrens	Institut für Mineralogie AG Petrologie, Leibniz Universität Hannover
Dr. Burkhard Schmidt	Abteilung Mineralogie Geowissenschaftliches Zentrum Göttingen Georg-August-Universität Göttingen
Dr. Kirsten Techmer	Abteilung Mineralogie Geowissenschaftliches Zentrum Göttingen Georg-August-Universität Göttingen

Tag der mündlichen Prüfung: 04.02.2022

Abstract

This thesis presents the first rheological investigations of melts from the Colli Albani Volcanic District (CAVD) near Rome (Italy). Despite their silica-poor (< 45 wt%) and ultrapotassic composition – indicating a low viscosity melt –, the volcanic events unexpectedly showed mainly an explosive eruptive style emitting large volumes of pyroclastic material. Such eruptions usually occur in highly viscous melts.

The magma chamber of the CAVD is seated in a thick carbonate sequence getting assimilated by the melt and suppling the magma with CaO and a CO_2-rich fluid.

Viscosity and calorimetric measurements are performed with synthetic melts with the compositions of the two largest eruptions of the CAVD: the Pozzolane Rosse (PR) and the Pozzolane Nere (PN) event. To study the rheologic PR melt evolution during magma storage and ascent, 7 wt% CaO were subtracted from the erupted PR composition (PR-CaO) representing the melt before the contamination by the carbonate wall rock. Since the pyroclastic products of the PR event contain mainly leucite crystals, 4 mol% $KAlSi_2O_6$ are removed from the PR composition to investigate the viscosity of the residual melt (PR-Leu). The compositions of the melts range from foiditic (PR and PR-CaO) to tephritic (PR-Leu) to tephri-phonolitic (PN) up to a further phonolitic melt with the composition from the "white pumice" of the AD 79 Vesuvius eruption (WPVe).

Three series of measurements are done: to get an overview to the rheological features in general, investigated glasses are synthesised in air and investigated. Since the CAVD melts are Fe-rich, further melts are made with the half amount (PR-0.5Fe, PR-Leu-0.5Fe and PN-0.5Fe) and with 30 wt% (PR-0.7Fe) of the original Fe content and Fe-free (PR-Fe and PN-Fe) to avoid crystallisation effects during measurements. Fe^{2+} was replaced by Mg^{2+} and Fe^{3+} was replaced by Al^{3+}.

To address the enrichment of the melts with a CO_2-rich fluid, the rheology of PR-0.5Fe and PR-Leu-0.5Fe, PN-0.5Fe as well as the WPVe melts made in an internally heated pressure vessel are investigated as a function of CO_2 concentrations up to ~0.50 wt% CO_2. A third series of viscosity measurements is done with two different Fe ratios in the melts affecting their viscosities. The PR-0.5Fe, PR-Leu-0.5Fe, PN-0.5Fe and the WPVe melts are re-equilibrated in a gas mixing furnace with H_2/CO_2 controlling the oxygen fugacities of $10^{-4.00}$ and $10^{-7.00}$ bar and hence the Fe speciation. Viscosity and calorimetric measurements were done in the glass transition range T_g from 600 - 820 °C and viscosities range from ~$10^{8.5}$ to ~$10^{13.5}$ Pa s. The measurements indicate a viscosity decrease during PR melt evolution: the contamination of the

carbonate host rock lowers the PR melt viscosity due to an enrichment in CaO. The viscosity of the residual melt PR-Leu decreases as a consequence of the depletion in SiO_2 and Al_2O_3 caused by leucite crystallisation. An enrichment of CO_2 affects the viscosities and calorimetric T_g slightly to negligibly. However, disintegrating and foaming of the samples during measurements before reaching T_g partly prevent reliable statements for PR-0.5Fe and PN-0.5Fe. In contrast, a CO_2 content of ~0.07 wt% and ~0.50 wt% decreases T_g^{12} by 14 °C and 5°C for the WPVe and PR-Leu-0.5Fe melt, respectively.

An increase of Fe^{2+}/Fe_{tot} from ~0.42 to ~0.76 for the CAVD melts results in a decrease in T_g^{12} from ~5 °C, ~30 °C and up to ~50 °C for PR-Leu-0.5Fe, PR-0.5Fe and PN-0.5Fe, respectively, with the highest drop in T_g^{12} for the most polymerised melt.

Although all melts investigated in the presented thesis are nominally anhydrous (< 0.5 wt% H_2O), they contain up to 0.23 wt% H_2O. It is shown that these small amounts of H_2O have a stronger decreasing effect on the viscosities than an increase in CO_2 or Fe^{2+}/Fe_{tot} investigated in this study.

Regarding the PR eruption, it is assumed to have a low viscosity residual liquid melt after the crystallisation of up to 60 vol% leucite. The entry of the CO_2-rich fluid exceeds the CO_2 solubility of the melt resulting in bubble formation and buoyancy of the resulting magma. Both processes – the former one leads to a dramatic increase of the magma viscosity and the latter one builds up pressure within the magma – are consequently assumed to feed the explosivity of the PR eruption and the high volume of erupted material.

Zusammenfassung

Diese Arbeit präsentiert die ersten rheologischen Untersuchungen von Schmelzen aus dem Vulkangebiet Albaner Berge (CAVD) nahe Rom (Italien). Trotz ihrer SiO_2-armen (< 45 Gew.-%) und hoch K-haltigen Zusammensetzung – was auf eine Schmelze mit niedriger Viskosität hindeutet – zeigten die Vulkanausbrüche unerwarteterweise hauptsächlich einen explosiven Eruptionsstil, der große Mengen an pyroklastischem Material förderte. Solche Eruptionen treten üblicherweise in hochviskosen Schmelzen auf.

Die Magmakammer des CAVD befindet sich in einer dicken Karbonatsequenz, die von der Schmelze assimiliert wird und das Magma an CaO und einem CO_2-reichen Fluid anreichert. Viskositäts- und Kalorimetriemessungen werden an synthetischen Schmelzen mit den Zusammensetzungen der beiden größten Eruptionen des CAVD durchgeführt: dem Pozzolane Rosse (PR) und dem Pozzolane Nere (PN) Ausbruch. Um die rheologische Entwicklung der PR-Schmelze während Magmenspeicherung und -aufstieg zu untersuchen, wurden 7 Gew.-% CaO von der eruptierten PR-Zusammensetzung (PR-CaO) abgezogen, die die Schmelze vor der Kontamination durch das Karbonatgestein repräsentiert. Da die pyroklastischen Produkte des PR-Ausbruchs hauptsächlich Leuzitkristalle enthalten, werden 4 Mol-% $KAlSi_2O_6$ von der PR-Zusammensetzung abgezogen, um die Viskosität der Restschmelze (PR-Leu) zu untersuchen. Die Zusammensetzungen der Schmelzen reichen von foiditisch (PR und PR-CaO) über tephritisch (PR-Leu) und tephri-phonolithisch (PN) hin zu einer weiteren phonolitischen Schmelze mit der Zusammensetzung des „weißen Bimsgesteins“ vom Ausbruch des Vesuvs 79 n. Chr. (WPVe).

Drei Messreihen werden durchgeführt: um einen Überblick über die rheologischen Eigenschaften im Allgemeinen zu bekommen, werden die untersuchten Gläser in Luft synthetisiert und gemessen. Da die CAVD-Schmelzen Fe-reich sind, werden zusätzliche Schmelzen mit der halben Konzentration (PR-0.5Fe, PR-Leu-0.5Fe und PN-0.5Fe) und mit 30 Gew.-% (PR-0.7Fe) des originalen Fe-Gehalts und Fe-frei (PR-Fe und PN-Fe) hergestellt, um Kristallisationseffekte während der Messungen zu vermeiden. Fe^{2+} wurde durch Mg^{2+} und Fe^{3+} wurde durch Al^{3+} ersetzt.

Um der Anreicherung der Schmelze mit einem CO_2-reichen Fluid gerecht zu werden, wird die Rheologie von der PR-0.5Fe- und der PR-Leu-0.5Fe-, PN-0.5Fe- sowie der WPVe-Schmelze, die in einem intern beheizten Druckgefäß hergestellten werden, als Funktion von CO_2-Konzentrationen bis zu ~0,50 Gew.-% CO_2 untersucht. Eine dritte Serie von

Viskositätsmessungen wird mit zwei unterschiedlichen Fe-Verhältnissen in den Schmelzen durchgeführt, die ihre Viskositäten beeinflussen. Die PR-0.5Fe-, PR-Leu-0.5Fe-, PN-0.5Fe- und die WPVe-Schmelzen werden in einem Gasmischungsofen mit H_2/CO_2, was die Sauerstofffugazitäten von $10^{-4.00}$ and $10^{-7.00}$ bar und folglich die Fe-Spezies kontrolliert, re-equilibriert. Viskositäts- und Kalorimetriemessungen wurden im Glasübergangsbereich T_g von 600 - 820 °C und im Viskositätsbereich von ~$10^{8.5}$ to ~$10^{13.5}$ Pa s durchgeführt. Die Messungen deuten auf eine Viskositätsabnahme während der Entwicklung der PR-Schmelze hin: die Verunreinigung durch das karbonatische Umgebungsgesteins senkt die Viskosität der PR-Schmelze aufgrund einer Anreicherung an CaO. Die Viskosität der Restschmelze PR-Leu sinkt als Folge der Verarmung an SiO_2 und Al_2O_3 durch Leuzitkristallisation. Eine Anreicherung an CO_2 beeinflusst die Viskositäten und die kalorimetrische T_g geringfügig bis vernachlässigbar. Allerdings verhindert ein Zerspringen und Aufschäumen der Proben während der Messungen noch vor Erreichen von T_g zum Teil zuverlässige Aussagen für PR-0.5Fe und PN-0.5Fe. Im Gegensatz dazu verringert ein CO_2-Gehalt von ~0,07 Gew.-% und ~0,50 Gew.% T_g^{12} um 14 °C bzw. 5 °C für die WPVe- bzw. PR-Leu-0.5Fe-Schmelze.

Ein Anstieg von Fe^{2+}/Fe_{tot} von ~0,42 auf ~0,76 für die CAVD-Schmelzen führt zu einer Abnahme von T_g^{12} von ~5 °C bzw. ~30 °C bzw. bis zu ~50 °C für PR-Leu-0.5Fe, PR-0.5Fe bzw. PN-0,5Fe, wobei der höchste Abfall von T_g^{12} für die am stärksten polymerisierte Schmelze ermittelt wurde. Obwohl alle in der vorliegenden Arbeit untersuchten Schmelzen nominell wasserfrei sind (< 0,5 Gew.-% H_2O), enthalten sie bis zu 0,23 Gew.-% H_2O. Es wird gezeigt, dass diese geringen H_2O-Mengen einen stärkeren viskositätsreduzierenden Einfluss haben als die in dieser Studie untersuchten Erhöhungen von CO_2 oder Fe^{2+}/Fe_{tot}.

Hinsichtlich der PR-Eruption wird eine niedrigviskose Restschmelze nach der Kristallisation von bis zu 60 Vol.-% Leuzit angenommen. Der Eintrag des CO_2-reichen Fluids übersteigt die CO_2-Löslichkeit der Schmelze, was zu Blasenbildung und Auftrieb des resultierenden Magmas führt. Somit wird angenommen, dass beide Prozesse – ersterer führt zu einem dramatischen Anstieg der Magmaviskosität und letzterer baut Druck innerhalb des Magmas auf – die Explosivität der PR-Eruption und das hohe Volumen an Eruptionsmaterial speisen.

Acknowledgement

The present work marks the end of a temporally small but important chapter in my life.
The scientific part of this chapter was an amazing and wonderful one. In spite of many failed experiments, the success after (sometimes) long periods made me nearly fly. For the possibility to make this experience I am greatly grateful to Prof. Dr. Sharon Webb who create this project and supported me over the whole time whenever I needed a discussion. Additionally, she organised the funding for the first 3 years and the following 3 months. Thanks for it!
Another great colleague in this department who I thank a lot is Bettina Schlieper-Ludewig. She introduced and helped me with all the experimental and methodical things implying the viscosity and the calorimetric measurements and especially the tricky method of the determination of the Fe speciation.
Dr. Burkhard Schmidt is a further colleague who enables a lot of experiments. Although he is always busy, he had always time when I became desperate – independently of the kind of problem. Furthermore, he discussed the results with me in detail. Great thanks!
I also thank Dr. Kirsten Techmer for her support at the SEM and the kind talks when we met here in the department.
And there is another person who sugared my daily life at work: the nice Petra Wolfrath working in the "background". It is a great advance to have her in this department.
But there are a lot of further people who I would like to thank: Marina for her inspiring help and discussion during the measurements at the EMPA and the CS analyser, Alex for his technical support, Prof. Dr. Thomas Müller for the kind and encouraging words and spirit and all the other kind and helpful colleagues in this department and alumni as Max and Sara.
Additionally, I am grateful to all members of my thesis committee that they take the extra time for this thesis and the disputation.
And besides my life as PhD student, I had a couple of friends who facilitated my time during this PhD chapter and I want to thank them a lot and for the "chewed ears" that I did to them.
Last but not least, I am grateful to my parents encouraging me at any stage in my life as a PhD student – and before.

Table of Content

List of abbreviations

Abbreviation	Meaning
AD	anno Domini
AG	Adam-Gibbs
BO	bridging oxygen
BP	before present
CS	carbon sulphur
DSC	differential scanning calorimetry
CAVD	Colli Albani Volcanic District
DGG1	Na_2O-CaO-SiO_2 float glass from the Deutsche Glastechnische Gesellschaft
DRE	dense-rock equivalent (in km^3)
FTIR	Fourier transform infrared spectroscopy
GRD08	viscosity model of Giordano et al. (2008)
IHPV	internally heated pressure vessel
IR	infrared
MIR	mid-infrared
MORB	mid-ocean ridge basalt
NBO	non-bridging oxygen
NIR	near-infrared
NNO	Ni-NiO buffer
PN	composition of the Pozzolane Nere eruption
PN-2vol% magnetite	PN minus 2 vol% Fe_3O_4
PN-0.5Fe	composition of the PN minus 50 mol% Fe

Abbreviation	**Meaning**
PN-Fe	Fe- free composition of the PN
PR	composition of the Pozzolane Rosse eruption
PR-2vol% magnetite	PR minus 2 vol% Fe_3O_4
PR-0.5Fe	composition of the PR minus 50 mol% Fe
PR-0.7Fe	composition of the PR minus 70 mol% Fe
PR-Fe	Fe- free composition of the PR
PR-CaO	composition of Pozzolane Rosse minus 7 wt% CaO
PR-Leu	composition of Pozzolane Rosse minus 4 mol% $KAlSi_2O_6$
PR-Leu-0.5Fe	composition of PR-Leu minus 50 mol% Fe
SEM	scanning electron microscopy
TAS	total alkali ($Na_2O + K_2O$) vs SiO_2 (in wt%)
UV	ultraviolet
VFT	Vogel-Fulcher-Tammann
VIS	visible light
WPVe	composition of the “white pumice” from Vesuvius AD 79 eruption

List of physical symbols, constants and parameters

Symbol	Meaning	Unit
a	parameter of the Maier-Kelley-Fit	$J\ g^{-1}\ K^{-1}$
A	sample weight in air	kg
A	peak height of the IR absorbance	absorbance units
A	parameter of the Arrhenian equation	$\log_{10}$ Pa s
A_{AG}	pre-exponential constant of the AG theory	Pa s
A_{Arr}	pre-exponential constant of the Arrhenian equation	Pa s
A_e	pre-exponential constant of the AG theory	$\log_{10}$ Pa s
A_{VFT}	constant of the VFT equation	$\log_{10}$ Pa s
atm	physical atmosphere	1 atm = 1.013 bar
b	parameter of the Maier-Kelley-Fit	$J\ g^{-1}\ K^{-2}$
B	parameter of the Arrhenian equation	K
B	sample weight in distilled water	kg
B_e	parameter of the Adam-Gibbs theory	$J\ mol^{-1}$
B_{VFT}	parameter of the VFT equation	K
c	parameter of the Maier-Kelley-Fit	$J\ g^{-1}\ K$
c	concentration	wt%
C_{VFT}	parameter of the VFT equation	K
C_p^{conf}	configurational heat capacity	$J\ mol^{-1}\ K^{-1}$
c_{pg}	heat capacity of the glass	$J\ g^{-1}\ K^{-1}$
C_{pg}	heat capacity of the glass ($C_{pg} = c_{pg}\ M$)	$J\ mol^{-1}\ K^{-1}$
c_{pl}	heat capacity of the liquid	$J\ g^{-1}\ K^{-1}$
C_{pl}	heat capacity of the liquid ($C_{pl} = c_{pl}\ M$)	$J\ mol^{-1}\ K^{-1}$

Symbol	Meaning	Unit
d	thickness	m
E_A	activation energy	J mol^{-1}
f	constant in η_{rel} equation (Einstein 1906)	dimensionless
F	force	N
fO_2	oxygen fugacity	bar
G	elastic shear modulus	Pa
G_∞	elastic shear modulus at infinite frequency	Pa
K_{Onset}	shift factor	
l	penetration distance	m
m	fragility	dimensionless
M	molar mass	g mol^{-1}
$m_{Arrhenian}$	fragility corresponding to the Arrhenian equation	dimensionless
m_{VFT}	fragility corresponding to the VFT equation	dimensionless
P	pressure	Pa
ppm	parts per million by weight	dimensionless
q	cooling rate	°C s^{-1}
r	radius	m
R	gas constant	8.314 J K^{-1} mol^{-1}
S^{conf}	configurational entropy	J mol^{-1} K^{-1}
t	time	s, min or h
T	temperature	K
T´	a temperature below the glass transition range	K
T^*	a temperature above the glass transition range	K
T_f	fictive temperature	K

Symbol	Meaning	Unit
T_f'	limiting fictive temperature	K
T_g	glass transition temperature	K
T_g^9	temperature at which the viscosity is 10^9 Pa s	K
T_g^{12}	temperature at which the viscosity is 10^{12} Pa s	K
T_g^{Onset}	temperature at the beginning of the glass transition determined by calorimetric measurements	K
X	chemical composition	wt% and mol%
X_{SiO_2}	mole fraction of the SiO_2 content	dimensionless
γ	$(Na_2O + K_2O + CaO + MgO + FeO)/(Na_2O + K_2O + CaO + MgO + FeO + Al_2O_3 + Fe_2O_3)$	dimensionless
Δ	difference	
ε	absorption coefficient	l mol^{-1} cm^{-1}
η	viscosity	Pa s
η_0	time-independent viscosity	Pa s
η_{eff}	effective viscosity	Pa s
η_{melt}	viscosity of the melt	Pa s
η_{rel}	relative viscosity	dimensionless
$\eta(T_{erupt})$	viscosity at the temperature of eruption	Pa s
ρ	density	g cm^{-3}
ρ_{H_2O}	density of distilled H_2O	g cm^{-3}
σ	standard deviation	
τ	relaxation time	s
τ_0	vibration frequency at infinite temperature	s
φ	bubble fraction	dimensionless

Preface

This research is initiated by Prof. Dr. Sharon Webb and the funding of the first 3 years was given by the Deutsche Forschungsgemeinschaft with the grant No. WE 1801/15-1 and the following 3 months were financed by the Georg-August-Universität Göttingen.

The present thesis consists of 5 chapters: an introduction giving an overview of the actual state of research to viscosity the main feature of melts with that this thesis handles.

The following Chapters 2 and 3 are articles both published in a scientific journal. Chapter 4 contains a manuscript submitted to a scientific journal. Since every manuscript has its own publishing history, different author contributions or other specification, these Chapters 2 – 4 have an extra brief preface.

The contents presented in the Chapters 2 and 3 are identical to the publications in the journals. The figure and table and equation numbers are the same as in the published articles. Consequently, numerations start always at 1 within every new Chapter. This form is consequently held throughout the whole thesis additionally for the Chapters 1 and 4 and 5 not published (yet).

In contrast, the layout of the publications in Chapters 2 and 3 are not that as in the published versions to address a uniform “design” within the whole thesis.

1 Introduction

Viscosity of silicate melts

Rheology concerns the flowing features of a material. The viscosity of a melt describes the resistance of the material to flow. It strongly depends on temperature, melt composition including volatile content and its crystal fraction and strain rate (i.e. Dingwell and Webb 1989; Webb 1997; Takeuchi 2011).
Pressure slightly affects viscosity – both increasing and decreasing viscosity (Bottinga and Richet 1995). This effect is, however, negligible in comparison with the drastic temperature and compositional induced viscosity changes (i.e. Vetere et al. 2010; Misiti et al 2011; Whittington et al. 2000).

Temperature dependence of viscosity

The structure of a silicate melt seeks an equilibrium to the conditions to which the melt is exposed and attempts to re-equilibrate as soon as the environmental conditions change. The timescale of the re-equilibration of the structure depends on temperature T and the melt viscosity η at the given temperature. The relaxation time τ and the viscosity η are linked by the Maxwell relation:

$$\tau(T) = \frac{\eta(T)}{G} \quad (1)$$

with τ – temperature dependent relaxation time in s, η – temperature dependent viscosity in Pa s and G – elastic shear modulus found to be 10 ± 0.5 GPa (Dingwell and Webb 1989). With increasing temperature, the relaxation time decreases resulting in a reduction in viscosity (i.e. Richet 1984; Dingwell and Webb 1989; Webb 1997). Over a relatively short temperature range – i.e. in the glass transition range T_g at which a melt changes its rheological properties from a liquid to a glass-like behaviour as a function of time and vice versa –, the temperature dependence of viscosity can be expressed by the Arrhenian equation:

$$\eta(T) = A_{Arr} \exp(\frac{E_A}{R\,T}) \quad (2)$$

with η – temperature dependent viscosity in Pa s, A_{Arr} – pre-exponential constant, E_A – activation energy in J mol^{-1}, R – gas constant, T – temperature in Kelvin (i.e. Bockris et al. 1955; Shaw 1972; Urbain et al. 1982). Over a wide temperature range (> 1000 K), the logarithm of viscosity ($\log_{10}$ η) vs inverse temperature does not follow a straight line as given by the Arrhenian equation (Eq. 2). Therefore, the Vogel-Fulcher-Tammann equation:

$$log_{10}\eta = A_{VFT} + \frac{B_{VFT}}{T - C_{VFT}} \quad (3)$$

with η – temperature dependent viscosity in Pa s, A_{VFT} – constant, B_{VFT} and C_{VFT} – parameters, T – temperature in Kelvin (i.e. Bockris et al. 1955; Shaw 1972; Urbain et al. 1982) can be used to describe the $\log_{10}$ η data as a function of inverse temperature.
For a robust extrapolation of high viscosity data (i.e. in the T_g range) to higher temperatures, the Adam-Gibbs theory is used based on the equation:

$$\eta(T) = A_{AG} \exp\left(\frac{B_e}{T\, S^{conf}}\right) \quad (4)$$

with η – temperature dependent viscosity in Pa s, A_{AG} – pre-exponential constant representing the viscosity at infinite temperature, B_e – parameter, T – temperature in Kelvin, S^{conf} – temperature dependent configurational entropy in J mol^{-1} K^{-1} defined by:

$$S^{conf}(T) = S^{conf}\left(T_g^{12}\right) + \int_{T_g^{12}}^{T} \frac{C_p^{conf}}{T} dT \quad (5)$$

with C_p^{conf} – configurational heat capacity in J mol^{-1} K^{-1} given as:

$$C_p^{conf} = C_{pl} - C_{pg} \quad (6)$$

with C_{pl} – heat capacity of the liquid in J mol^{-1} K^{-1} and C_{pg} – heat capacity of the glass in J mol^{-1} K^{-1} (i.e. Adam and Gibbs 1965; Richet 1984; Webb 2008). S^{conf} is assumed to be constant at temperatures below T_g^{12}. The heat capacities are determined by the differential scanning calorimetry (DSC) (Fig. 1) and B_e as well as S^{conf} are fitted by combining the viscosity and the calorimetric data.
A further feature that can be determined by the DSC measurements is the limiting fictive temperature T_f' defined as the temperature at which the melt structure reaches equilibrium with

the ambient temperature for the last time during cooling. Hence, the melt structure gets frozen at T_f' and depends on the cooling rate of the glass (i.e. Scherer 1984; Moynihan 1995; Webb 1997).

Narayanaswamy (1971) and Moynihan et al. (1976) used the relationship between the temperature dependent heat capacity C_p and the temperature dependent fictive temperature T_f to calculate the limiting fictive temperature T_f' from the heat capacity curve with matching cooling- and heating-rates (DeBolt et al. 1976):

$$\left.\frac{dT_f}{dT}\right|_T = \frac{[C_p(T) - C_{pg}(T)]|_T}{[C_{pl}(T) - C_{pg}(T)]|_{T_f}} \tag{7}$$

$$\Rightarrow \int_{T'}^{T^*} \left[C_p(T) - C_{pg}(T)\right] dT = \int_{T_f'}^{T^*} \left[C_{pl}(T) - C_{pg}(T)\right] dT_f \tag{8}$$

with T_f – fictive temperature, T – temperature in Kelvin, C_p – heat capacity as a function of temperature, C_{pg} – unrelaxed glassy heat capacity as a function of temperature, C_{pl} – relaxed liquid heat capacity as a function of temperature, T_f' – limiting fictive temperature, T^* – a temperature above the glass transition region at which the heat capacity is equal to the equilibrium heat capacity, T′– a temperature below the glass transition region at which the heat capacity is that of the unrelaxed glass. Equation 8 is shown graphically in Fig. 1. The unrelaxed glassy heat capacity C_{pg} is extrapolated to higher temperature using the Maier-Kelley equation:

$$C_{pg}(T) = a + bT + cT^{-2} \tag{9}$$

with a, b and c as parameters, T – temperature in Kelvin (Maier and Kelley 1932).

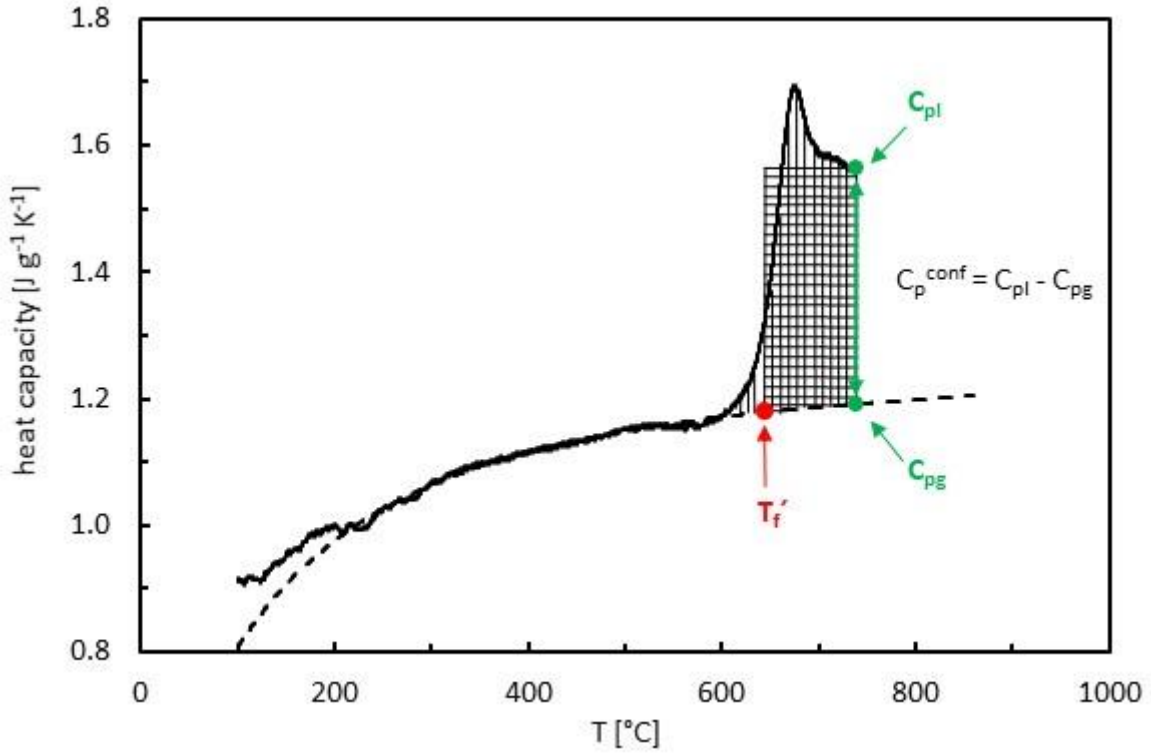

Fig. 1 Heat capacity curve vs temperature from a DSC measurement. C_p^{conf} is the difference of the liquid heat capacity C_{pl} and the extrapolated glassy heat capacity C_{pg} (presented as the dotted line). The left-hand side of Eq. 8 is illustrated by vertical stripes and the right-hand side of Eq. 8 is illustrated by horizontal stripes. The left-hand side is equal to the right-hand side at the marked temperature T_f'.

The temperature dependence of the viscosity of silicate melts is more pronounced in the low temperature – high viscosity range by varying orders of magnitude than in the high temperature – low viscosity range where the viscosities converge (i.e. Richet 1984; Whittington et al. 2000, 2001).

The curvature of $\log_{10} \eta$ vs inverse temperature (Eq. 3 and 4) over a wide temperature range is strongly affected by the composition: the higher the SiO_2 content of a melt the lower the deviation from the Arrhenian behaviour (i.e. Urbain et al. 1982; Richet 1984; Whittington et al. 2000).

All geological relevant processes concerning volcanic eruptions pass through the T_g range which occur in the vicinity of 10^{12} Pa s for magmatic flow processes (i.e. Dingwell and Webb 1989; Webb 1997; Vona et al. 2011). The micropenetration technique is a suitable method to determine the viscosity of a melt in the T_g range. For the determination of the viscosity at a given temperature, this method uses the penetration depth of a single sphere forced into the double polished and face parallel sample (Fig. 2 and 3) by the equation:

$$\eta = \frac{0.1875\ Ft}{r^{0.5} l^{1.5}} \tag{10}$$

with η –viscosity in Pa s, F – applied force in N, t – time in s, r – radius of the penetrating sphere in m, l – distance of indent in m (Pocklington 1940; Tobolsky and Taylor 1963; Dingwell et al. 1992).

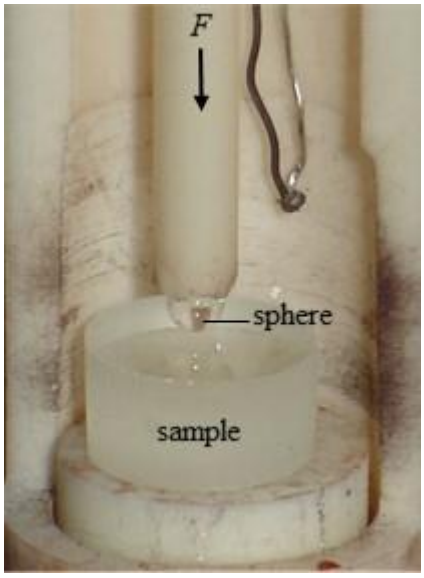

Fig. 2 Initial setting in the sample holder with the sphere on the cylindrical sample.

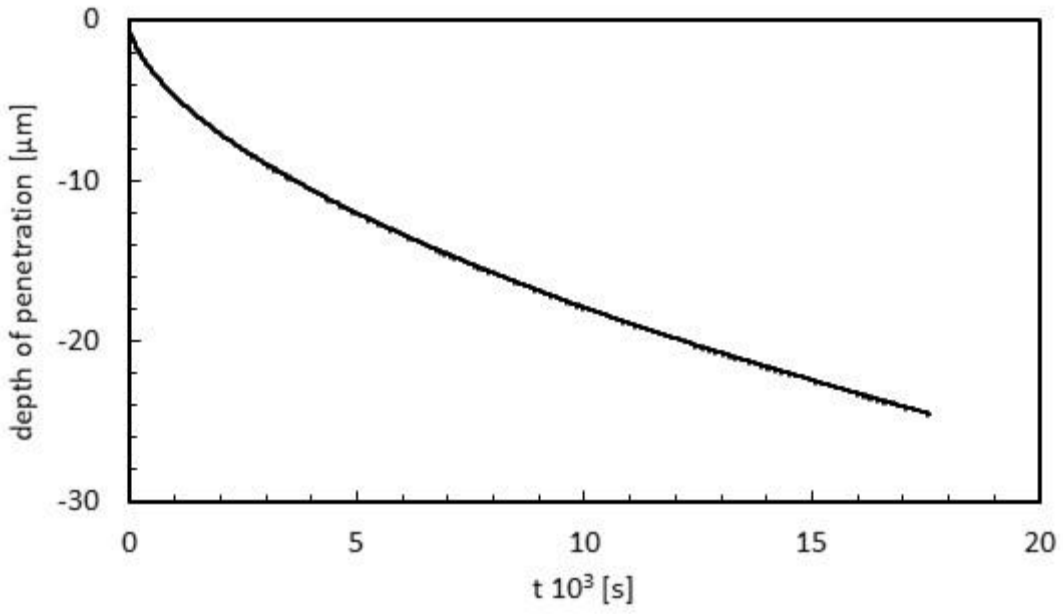

Fig. 3 Example of a penetration curve of the sphere into the sample with time at a given temperature. Data with time scales less than 100 τ are not considered for the determination of viscosity.

Compositional dependence of viscosity

In silicate melts, the network forming cation Si^{4+} is surrounded by four oxygen atoms to create SiO^{4+} tetrahedra. The SiO^{4+} tetrahedra - the fundamental component in silicate melts - are connected by their oxygen atoms[1] and build a three-dimensional network. The Si-O bonds are the strongest bonds within a multi component melt structure and hence their response upon heating to increasing temperature is slowest and a higher activation energy is required to break down these bonds to initiate viscous flow (i.e. Brückner 1970; Mysen et al. 1982; Webb 1997; Toplis 1998). Thus, there is a positive correlation between high polymerised SiO_2-rich melts and its viscosity (i.e. Bockris et al. 1955; Brückner 1970; Shaw 1972; Urbain et al. 1982; Richet 1984; Toplis et al. 1997; Takeuchi 2011). Tetrahedrally coordinated Si^{4+} can be replaced by Al^{3+} leaving a negative charge (i.e. Zachariasen 1932; Mysen et al. 1982; Webb et al. 2007). To compensate this charge deficit, insignificant amounts of Al^{3+} turn in a higher coordination (i.e. Webb et al. 2007; Liu et al. 2016; Novikov et al. 2017) or, however, most of the tetrahedrally coordinated and hence network forming Al^{3+} get charge balanced by mono- or bivalent cations such as K^+, Na^+, Ca^{2+}, Mg^{2+} (i.e. Mysen et al. 1982; Toplis et al. 1997; Webb 2007). In peraluminous[2] melts in which no more charge balancing cations are available, charge balanced tri-clusters form consisting of one Al-tetrahedron and two Si-tetrahedra bonded by one common oxygen atom (i.e. Toplis et al. 1997; Webb 2004; Webb 2005). Consequently, peraluminous melts are highly polymerised resulting in high viscosities. As soon as a melt composition gets metaluminous[3] to peralkaline[4], the mono- and bivalent cations that are not required to balance the charge deficit – induced by Al^{3+} or other trivalent cations – behave as network modifiers by breaking down the BOs of the tetrahedra to form non-bridging oxygens[5] resulting in a depolymerisation of the melt structure and consequently lowering the melt viscosity (i.e. Mysen et al. 19982; Toplis et al. 1997; Webb 2004). Generally, the more network modifiers in a silicate melt exist, the higher the degree of depolymerisation and hence, the lower the viscosity. This effect is non-linear whereby the viscosity of a more polymerised melt is greatly reduced by a further addition of network modifiers than that of a more depolymerised melt (i.e. Webb 2004). Not only the amount of network modifiers has to be considered but also the nature of the network modifying cation is important. Looking only at the alkali and alkaline-earth species, the viscosity is reduced – accompanied with a lower activation energy for viscous

[1] an oxygen bonded to two network forming cations connecting two tetrahedra is called bridging oxygen (BO)
[2] peraluminous = $Al_2O_3 > CaO + Na_2O + K_2O$ (in mole fraction) (Petro et al. 1979)
[3] metaluminous = $CaO + Na_2O + K_2O > Al_2O_3 > Na_2O + K_2O$ (in mole fraction) (Petro et al. 1979)
[4] peralkaline = $Al_2O_3 < Na_2O + K_2O$ (in mole fraction) (Petro et al. 1979)
[5] a non-bridging oxygen is briefly denominated NBO

flow – in order of most reducing effect to less reduced viscosity by Li → Na → K → Rb → Cs (Bockris et al. 1955; Hess et al. 1995; Toplis 1998) and Ba → Sr → Ca → Mg → Be (Urbain et al. 1982; Hess et al. 1996; Webb 2011), respectively.

Among multivalent components, Fe is the most abundant one in silicate melts. Corresponding to terrestrial conditions of the crust and upper mantle, it can exist as ferrous Fe^{2+} and ferric Fe^{3+}. Fe^{3+} is mainly tetrahedrally coordinated when sufficient charge balancers exist but could also be higher coordination (i.e. Kress and Carmichael 1991; Lange and Navrotsky 1992; Mysen and Richet 2005; Wilke 2005; Borisov et al. 2017). The incorporation of Fe^{2+} is often octahedrally, however, it could additionally be less coordinated (i.e. Mysen and Richet 2005; Wilke 2005; Stabile et al. 2016). Nevertheless, it is assumed that Fe^{3+} behaves as a network former whereas Fe^{2+} acts as a network modifier. Consequently, both cations affect the viscosity oppositely: Fe^{3+} increases the viscosity whereas Fe^{2+} reduces the viscosity of a silicate melt wherefore the Fe ratio is important to know (i.e. Urbain et al. 1982; Webb 2005; Di Genova et al. 2017). The Fe ratio itself depends on melt composition, temperature, pressure and oxygen fugacity fO_2. Increasing temperature and/or decreasing fO_2 – representing more reduced conditions – increases the Fe^{2+} species while simultaneously decreasing Fe^{3+} in a melt resulting in a drop in melt viscosity (i.e. Kress and Carmichael 1991; Dingwell 1991; Di Genova et al. 2017). In more polymerised melts, Fe^{2+}/Fe^{3+} is higher than in less polymerised melts due to the charge balancing function of Fe^{2+} (Borisov et al. 2015). As soon as all charge deficits – induced by trivalent network formers – are compensated the residual Fe^{2+} depolymerise the melt structure by forming NBOs resulting in a decrease in viscosity (i.e. Dingwell and Virgo 1988; Webb 2005). In more depolymerised melts in which network modifiers are abundant, the network forming species Fe^{3+} is favoured which is charge balanced by the mono- and/or bivalent cations (Thornber et al. 1980; Borisov et al. 2015). The presence of H_2O in a melt additionally promotes the oxidised species Fe^{3+} by its reduction to H_2 which is, however, restricted to reduced conditions at low pressure where H_2 is able to migrate through and degas out of the melt (Cottrell and Kelley 2011).

H_2O and CO_2 dependence of viscosity

H_2O is the most abundant volatile in silicate melts (i.e. Whittington et al. 2000; Bourgue and Richet 2001; Robert et al. 2013). Depending on the total H_2O concentration H_2O^{tot}, it is dissolved as molecular H_2O^{mol} or/and as the hydroxyl group OH^-. The latter one is the predominant species with $H_2O^{tot} < 0.5$ wt% but its predominance decreases with increasing H_2O^{tot}. OH^- concentration levels off when H_2O^{tot} exceeds approx. 3-4 wt% and subsequently

H_2O^{mol} is the dominant species (i.e. Stolper 1982; Silver et al. 1990; Ohlhorst et al. 2001). The viscosity of a silicate melt is strongly affected by H_2O since H_2O^{mol} dissociates by consuming BOs under the formation of NBOs reducing the polymerisation of the structure (i.e. Mysen et al. 1982; Stolper 1982 and references therein; Richet et al. 2000) or additionally by the substitution of a charge balancing cation by H^+ weakening the strong BOs (i.e. Kohn et al. 1989). Both processes reduce the viscosity of a melt. The non-linear decreasing trend of the viscosity follows the occurrence of OH^- in the melt: the viscosity drop is strongest within the first amounts of H_2O^{tot} up to 1 wt% – mainly existing as OH^-. By further addition of H_2O its speciation becomes successively more H_2O^{mol} and the viscosity continues to decrease more slightly up to approx. 2 wt% H_2O^{tot} and flattens out at higher H_2O^{tot} contents (Stolper 1982; Dingwell et al. 1996; Whittington et al. 2000, 2001). At a given H_2O^{tot}, H_2O^{mol}:OH^- ratio increases with increasing SiO_2 content of a melt (i.e. Silver et al. 1990; Ohlhorst et al. 2001). However, H_2O decreases the viscosity in a similar way as alkalis or even more effective (Hess et al. 1995; Dingwell et al. 1996; Richet et al. 2000; Whittington et al. 2001). This drop in melt viscosity provoked by H_2O is more pronounced for more polymerised than for less polymerised melts based on their anhydrous counterparts (i.e. Persikov 1991; Whittington et al. 2000; Robert et al. 2013). Additionally, the viscosity reducing effect of H_2O is stronger in the low-temperature – high-viscosity range (i.e. T_g) than at higher temperatures (Whittington et al. 2000, 2001; Robert et al. 2013).

CO_2[6] is the second most abundant volatile in magmatic systems after H_2O (i.e. Blank and Brooker 1994; Bourgue and Richet 2001; Morizet et al. 2007). It is mainly dissolved as molecular CO_2^{mol} or as carbonate CO_3^{2-} (Fine and Stolper 1986; Blank and Brooker 1994; Guillot and Sator 2011). Under strongly reduced conditions, also CO and/or other carbon species can be dissolved in melts holding a high CO_2 solubility (i.e. Blank and Brooker and references therein; Ni and Keppler 2013). However, the CO:CO_2 ratio is very small and these small amounts of CO will be oxidised during magma ascent and are therefore irrelevant for volcanic near-surface processes. The CO_2 speciation strongly depends on melt composition. CO_3^{2-} is the product of the linkage of CO_2^{mol} with a reactive oxygen of the melt (Thibault and Holloway 1994; Morizet et al. 2007; Guillot and Sator 2011). As there is a great affinity of CO_2 to NBOs under formation of CO_3^{2-}, CO_3^{2-} is the only species in highly depolymerised, SiO_2-poor melts and its fraction decreases with increasing degree of polymerisation and SiO_2 content. Simultaneously, CO_2^{mol} increases and is the dominant or even only species in highly polymerised melts (i.e. Blank and Brooker 1994; Guillot and Sator 2011; Ni and Keppler 2013).

[6] CO_2 means the total amount of carbon without considering any speciation

The viscosity of silicate melts appears to be slightly reduced or even unaffected by the presence of CO_2 in a melt (i.e. Brearley and Montana 1989; White and Montana 1990; Bourgue and Richet 2001; Di Genova et al. 2014; Kleest and Webb 2021). To the current state of science, a detailed mechanism of the incorporation of CO_2 in the melt structure is not clearly identified. Some studies suggest that CO_2^{mol} is bonded weakly to BOs whereas CO_3^{2-} is integrated in the melt network by chemical bonds and favours the environment of network modifying cations especially Ca^{2+} (i.e. Blank and Brooker 1994; Guillot and Sator 2011; Ni and Keppler 2013). Other investigations propose a decoupled arrangement of CO_2 or even a carbonate melt subnetwork within the silicate melt – created by CO_3^{2-} and mono- and/or bivalent cations of the melt – whereat both networks are immiscible (i.e. Morizet et al. 2007; Morizet et al. 2017 and references therein). Although the degree of polymerisation of the silicate melt network increases with increasing CO_2 content due to the formation of the carbonate melt subnetwork, the contrasting measured decrease of T_g is explained by the extremely low viscosity of the carbonate melt subnetwork affecting the detected viscosity noticeably stronger than the increase of viscosity due to the of higher degree of polymerisation of the silicate melt structure.

In general, compositional induced processes resulting in lowering the degree of polymerisation of a melt accompanied by a decrease in viscosity are more distinct at lower temperatures (i.e. at T_g) than in the high temperature – low viscosity range (i.e. Hess et al. 1995; Webb 1997; Whittington et al. 2000) and are more pronounced for initially more polymerised melts (i.e. Bockris et al. 1955; Webb 2005; Whittington et al. 2000; Kleest and Webb 2021).

Crystal dependence of viscosity

Solid particles in a melt significantly affect rheology. The viscosity of a crystal bearing melt increases as a function of crystallinity as well as the size and shape (i.e. Vetere et al. 2010; Vona et al. 2011) and the surface roughness of the crystals (i.e. Campagnola et al. 2016). Within the first few vol% of crystals when the melt behaves like a dilute suspension without any particle interaction, the viscosity increases slightly or even negligibly. At elevated crystal contents, the grains get more and more connected with each other resulting in a non-linear increase of the melt viscosity (i.e. Stevenson et al. 1996; Costa 2005; Vetere et al. 2010; Vona et al. 2011; Campagnola et al. 2016). Additionally, the more elongated the particles in a melt the stronger is the viscosity increase due to their higher interaction with respect to spherical grains of the same volume (i.e. Stevenson et al. 1996; Vetere et al. 2010; Vona et al. 2011). The influence of textural features on the viscosity increase is stronger at higher crystal contents than at lower

ones (i.e. Vetere et al. 2010; Vona et al. 2011). As soon as a melt reaches a critical crystal volume, it essentially behaves like a solid (i.e. Costa 2005; Takeuchi 2011). When crystals nucleate and grow in a cooling magma chamber, the residual liquid melt changes its chemical composition affecting its viscosity due to the depletion of components incorporated in the solid phases. Consequently, the viscosity of a crystal-bearing melt is the result of the viscosity affecting particles and the viscosity of the residual liquid melt (i.e. Stevenson et al. 1996; Vetere et al. 2010; Vona et al. 2011; Campagnola et al. 2016).

Volcanological implication

The viscosity of a melt is an important transport property and controls magma ascent in a volcanic vent, crystallisation as well as degassing and diffusion processes and finally the explosive style of an eruption. The volcanic explosivity is conventionally assumed to be positive correlated to the SiO_2 content of a melt (i.e. Freda et al. 2011; Cashman and Giordano 2014). Eruptions of SiO_2-rich and intermediate melts are usually (high) explosive. Rhyolitic to andesitic lavas are typically crystal- and bubble-bearing as for instance shown by the pumices of the eruption from the 0.7 Ma Bishop Tuff (Anderson et al. 1989), the 1663 AD eruption of the Usu volcano (Tomiya et al. 2010) or the 3430 yBP eruption of the Aniakchak volcano (Larsen 2006). For instance, due to the high SiO_2 content and the decreasing temperatures during magma ascent, the melt is relatively high viscous inhibiting sinking of phenocrysts as well as degassing of bubbles formed as a consequence of the decreased solubility of volatiles induced by depressuration. The segregated gas bubbles continue to grow and build up pressure within the melt which finally shoot explosively out of the vent accompanied by magma fragmentation during volcanic eruption.

In contrast, SiO_2-poor melts generally show an effusive eruption style. As they are less polymerised resulting in lower viscosities, segregated gases can escape easily. Furthermore, basic to ultra-basic melts typically erupt at higher temperatures than melts with higher SiO_2 contents and the viscosity of an emitted SiO_2-poor lava is mostly still able to flow.

A notable exception are volcanic events of the Colli Albani Volcanic District (CAVD) near Rome (Italy) which erupted effusively as well as explosively and emitted large volumes of pyroclastic material of silica undersaturated and K-rich compositions with FeO_{tot}[7] up to 9.50 wt% (i.e. Freda et al. 2011; Cashman and Giordano 2014). The both largest eruptions of the CAVD are the Pozzolane Rosse event (PR) (456 ± 3 ka (Marra et al. 2009)) and the Pozzolane Nere eruption (PN) (407 ± 4 ka (Karner et al. 2001)) and their striking meaning is clearly seen

[7] FeO_{tot} here gives the total Fe concentration as FeO without considering any speciation

on a plot of the dense-rock equivalent (DRE) vs SiO_2 concentration as their erupted volumes plot outside the cloud formed by other high DRE events around the world (Fig. 1 in Chapter 2). In the total alkali vs SiO_2 (TAS) diagram, the PR and PN melts plot in the foiditic and tephri-phonolitic field, illustrating the assumption that these melts should have low viscosities as a consequence of their low SiO_2 and high alkali content (Fig. 2 in Chapter 2). The pyroclastic deposits of both eruptions show crystal contents up to 60 vol % (Freda et al. 2011) and multiple evidence of assimilation of the carbonate wall rock in which the magma chamber of the CAVD is embedded leading to an enrichment in CaO and in a CO_2-rich fluid of the melts (i.e. Freda et al. 2011; Di Rocco et al. 2012).

Scope of this thesis

It is of scientific interest to understand why such silica undersaturated melts could erupt such a volume with such a violence. The common feature of bubble and crystal forming processes in a magma as well as the explosivity of a volcanic event is the viscosity of a melt. There are a number of questions to be addressed concerning the highly explosive eruptions of PR and PN:

- are the viscosities of the PR and PN melts really as low as assumed based on the estimation by the TAS diagram?
- what effects do CaO and the CO_2-rich fluid exert on the melt viscosity due to the assimilation of the carbonate wall rock?
- how does the leucite crystallisation affect the viscosity of the residual melt?
- what is the influence of the changing Fe speciation due to different oxygen fugacities during magma ascent on the melt viscosity?
- how does water affect the viscosities of these melts?
- and what is the influence of bubbles on the viscosity of the PR and PN melts?

In the search for the first 4 questions, the viscosities of 5 melts are investigated:

1 - with a composition of the pyroclastic products of the PR event (PR),
2 - with a composition before the PR melt was contaminated by the assimilation of the carbonate wall rock (PR-CaO = PR minus 7 wt% CaO),
3 - with the residual melt composition of PR after the crystallisation of 4 mol% leucite (PR-Leu = PR minus 4 mol% $KAlSi_2O_6$) as well as
4 - a composition of the erupted material from the PN eruption (PN) and
5 - the composition of the “white pumice” from the AD 79 eruption from the Vesuvius (WPVe).

With exception of the PR-CaO melt, the temperature dependent viscosities are determined as a function of CO_2 concentration and the Fe speciation.

References

Adam G and Gibb JH (1965) On the temperature dependence of cooperative relaxation properties in glass-forming liquids. J Chem Phys 43:139-146

Anderson AT Jr, Newman S, Williams SN, Druitt TH, Skirius C, Stolper E (1989) H_2O, CO_2, Cl and gas in Plinian and ash-flow Bishop rhyolite. Geol 17:221-225

Blank JG and Brooker RA (1994) Experimental studies of carbon dioxide in silicate melts: solubility, speciation and stable carbon isotope behaviour. In: Carroll MR and Holloway JR (eds) Volatiles in Magmas, vol 30. Rev Mineral. Mineralogical Society of America, Washington, 157-186

Bockris JO´M, MacKenzie JD, Kitchener JA (1955) Viscous flow in silica and binary liquid silicates. Transactions of the Faraday Society 51:1734-1748

Borisov A, Behrens H, Holtz F (2015) Effect of melt composition on Fe^{3+}/Fe^{2+} in silicate melts: a step to model ferric/ferrous ratio in multicomponent systems. Contrib Mineral Petrol 169:24

Borisov A, Behrens H, Holtz F (2017) Effect of strong network modifiers on Fe^{3+}/Fe^{2+} in silicate melts: an experimental study. Contrib Mineral Petrol 172:34

Bottinga Y and Richet P (1995) Silicate melts: The “anomalous” pressure dependence of the viscosity. Geochim et Cosmochim Acta 59:2725-2731

Bourgue E and Richet P (2001) The effects of dissolved CO_2 on the density and viscosity of silicate melts: a preliminary study. Earth Planet Sci Lett 193:57-68

Brearley M and Montana A (1989) The effect of CO_2 on the viscosity od silicate liquids at high pressure. Geochim et Cosmochim Acta 53:2609-2616

Brückner R (1970) Properties and Structure of vitreous Silica I. J Non-Cryst Solids 5:123-175

Campagnola S, Vona A, Romano C, Giordano G (2016) Crystallization kinetics and rheology of leucite-bearing tephriphonolite magmas from the Colli Albani volcano (Italy). Chem Geol 424:12-29

Cashman KV and Giordano G (2014) Calderas and magma reservoirs. J Volcanol Geotherm Res 288:28-45

Costa A (2005) Viscosity of high crystal content melts: Dependence on solid fraction. Geophys Res Lett 32:L22308

Cottrell E and Kelley KA (2011) The oxidation state of Fe in MORB glasses and the oxygen fugacity of the upper mantle. Earth Planet Sci Lett 305:270-282

DeBolt MA, Easteal AJ, Macedo PB, Moynihan CT (1976) Analysis of Structural Relaxation in Glass Using Rate Heating Data. J Am Ceram Soc 59:16-21

Di Genova D, Romano C, Alletti M, Misiti V, Scarlato P (2014) The effect of CO_2 and H_2O on Etna and Fondo Riccio (Phlegrean Fields) liquid viscosity, glass transition temperature and heat capacity. Chem Geol 377:72-86

Di Genova D, Vasseur J, Hess KU, Neuville DR, Dingwell DB (2017) Effect of oxygen fugacity on the glass transition, viscosity and structure of silica- and iron-rich magmatic melts. J Non-Cryst Solids 470:78-85

Dingwell DB (1991) Redox viscometry of some Fe-bearing silicate melts. Am Mineral 76:1560-1562

Dingwell DB and Virgo D (1988) Viscosities of melts in the Na_2O-FeO-Fe_2O_3-SiO_2 system and factors controlling relative viscosities of fully polymerized silicate melts. Geochim et Cosmochim Acta 52:395-403

Dingwell DB and Webb SL (1989) Structural Relaxation in Silicate Melts and Non-Newtonian Melt Rheology in Geological Processes. Phys Chem Minerals 16:508-516

Dingwell DB, Knoche R, Webb SL (1992) The effect of B_2O_3 on the viscosity of haplogranitic liquids. Am Mineral 77:457-461

Dingwell DB, Roman C, Hess KU (1996) The effect of water on the viscosity of a haplogranitic melt under P-T-X conditions relevant to silicic volcanism. Contrib Mineral Petrol 124:19-28

Di Rocco T, Freda C, Gaeta M, Mollo S, Dallai L (2012) Magma Chambers Emplaced in Carbonate Substrate: Petrogenesis of Skarn and Cumulate Rocks and Implications for CO_2 Degassing in Volcanic Areas. J Petrol 53:2307-2332

Fine G and Stolper E (1986) Dissolved carbon dioxide in basaltic glasses: concentrations and speciation. Earth Planet Sci Lett 76:263-278

Freda C, Gaeta M, Giaccio B, Marra F, Palladino DM, Scarlato P, Scottili G (2011) CO2-driven lrage mafic explosive eruptions: the Pozzolane Rosse case study from the Colli Albani Volcanic District (Italy). Bull Volcanol 73:241-256

Guillot B and Sator N (2011) Carbon dioxide in silicate melts: A molecular dynamics simulation study. Geochim et Cosmochim Acta 75:1829-1857

Hess KU, Dingwell DB, Webb SL (1995) The influence of excess alkalis on the viscosity of a haplogranitic melt. Am Mineral 80:297-304

Hess KU, Dingwell DB, Webb SL (1996) The influence of alkaline-earth oxides (BeO, MgO, CaO, SrO, BaO) on the viscosity of a haplogranitic melt: systematics of non-Arrhenian behaviour. Eur J Mineral 80:371-381

Karner DB, Marra F, Renne PR (2001) The history of the Monti Sabatini and Alban Hills volcanoes: groundwork for assessing volcanic-tectonic hazards for Rome. J Volcanol Geotherm Res 107:185-219

Kleest C and Webb SL (2021) Influence of CO_2 on the rheology of melts from the Colli Albani Volcanic District (Italy): foidite to phonolite. Contrib Mineral Petrol 176:92

Kohn SC, Dupree R, Smith ME (1989) Proton environment and hydrogen-bonding in hydrous silicate glasses from proton NMR. Nature 337:539-541

Kress VC and Carmichael ISE (1991) The compressibility of silicate liquids containing Fe_2O_3 and the effect of composition, temperature, oxygen fugacity and pressure on their redox state. Contrib Mineral Petrol 108:82-92

Lange RA and Navrotsky A (1992) Heat capacities of Fe_2O_3-bearing silicate liquids. Contrib Mineral Petrol 110:311-320

Larsen JF (2006) Rhyodacite magma storage conditions prior to the 3430 yBP caldera-forming eruption of Aniakchak volcano, Alaska. Contrib Mineral Petrol 152:523-540

Liu M, Jacob A, Schmetterer C, Masset P, Hennet L, Fischer HE, Kozaily, Jahn S, Gray-Weale A (2016): From atomic structure to excess entropy: a neutron diffraction and density functional theory study of CaO-Al_2O_3-SiO_2 melts. J Phys Condens Matter vol 28:135102

Maier CG, Kelley KK (1932) An equation for the representation of high-temperature heat content data. J Am Chem Soc 54:3243-3246

Marra F, Karner DB, Freda C, Gaeta M, Renne P (2009) Large mafic eruptions at the Alban Hills Volcanic District (Italy): Chronostratigraphy, petrography and eruptive behaviour. J Volcanol Geotherm Res 179:217-232

Misiti V, Vetere F, Freda C, Scarlato P, Behrens H, Mangiacapra A, Dingwell DB (2011) A general viscosity model of Campi Flegrei (Italy) melts. Chem Geol 290:50-59

Morizet Y, Nichols ARL, Kohn SC, Brooker RA, Dingwell DB (2007) The influence of H_2O and CO_2 on the glass transition temperature: insights into the effects of volatiles on magma viscosity. Eur J Mineral 19:657-669

Morizet Y, Paris M, Sifre D, Di Carlo I, Ory S, Gaillard F (2017) Towards the reconciliation of viscosity change and CO_2-induced polymerization in silicate melts. Chem Geol 458:38-47

Moynihan CT (1995) Structural relaxation and glass transition. Rev Mineral 32:1-19

Moynihan CT, Macedo PB, Montrose CJ, Gupta PK, DeBolt MA, Dill JF, Dom BE, Drake PW, Easteal AJ, Elterman PB, Moeller RP, Sasabe H, Wilder JA (1976) Structural Relaxation in vitreous Materials. Ann NY Acad Sci 279:15-35

Mysen BO, Virgo D, Seifert FA (1982) The Structure of Silicate Melts: Implications for Chemical and Physical Properties of Natural Magma. Rev Geophys Space Phys 20:353-383

Mysen BO and Richet P (2005) Silicate Glasses and Melts – Properties and Structure. Series Developments in Geochemistry 10. Edited by Elsevier B.V.

Narayanaswamy OS (1971) A Model of Structural Relaxation in Glass. J Am Ceram Soc 54:491-498

Ni H and Keppler H (2013) Carbon in Silicate Melts. Rev Mineral Geochem 75:251-287

Novikov AN, Neuville DR, Hennet L, Gueguen Y, Thiaudière D, Charpentier T, Florian P (2017): Al and Sr environment in tectosilicate glasses and melts: Viscosity, Raman and NMR investigation. Chem Geol 461:115-127

Ohlhorst S, Behrens H, Holtz F (2001) Compositional dependence of molar absorptivities of near-infrared OH- and H_2O bands in rhyolitic to basaltic glasses. Chem Geol 174:5-20

Persikov ES (1991) The viscosity of magmatic liquids: Experiment, generalised patterns. A model for calculation and prediction. Application. In Physical Chemistry of Magmas. Adv Phys Geochem

Petro WL, Vogel TA, Wilbrand JT (1979) Major-Element Chemistry of plutonic Rock Suites from compressional and extensional Plate Boundaries. Chem Geol 26:217-235

Pocklington HC (1940) Rough measurement of high viscosities. Proc Cambridge Phil Soc 36:507-508

Richet P (1984) Viscosity and configurational entropy of silicate melts. Geochim et Cosmochim Acta 48:471-483

Richet P, Whittington A, Holtz F, Behrens H, Ohlhorst S, Wilke M (2000) Water and density of silicate glasses. Contrib Mineral Petrol 138:337-347

Robert G, Whittington AG, Stechern A, Behrens H (2013) The effect of water on the viscosity of a synthetic calc-alkaline basaltic andesite. Chem Geol 346:135-148

Shaw HR (1972) Viscosities of magmatic silicate liquids: an empirical method of prediction. Am J Sci 272:870-893

Stabile P, Webb S, Knipping JL, Behrens H, Paris E, Giuli (2016) Viscosity of pantelleritic and alkali-silicate melts: Effect of Fe redox state and Na/(Na + K) ratio. Chem Geol 442:73-82

Silver LA, Ihinger PD, Stolper E (1990) The influence of bulk composition on the speciation of water in silicate glasses. Contrib Mineral Petrol 104:142-162

Stevenson RJ, Dingwell DB, Webb SL, Sharp TG (1996) Viscosity of microlite-bearing rhyolitic obsidians: an experimental study. Bull Volcanol 58:298-309

Stolper E (1982) Water in Silicate Glasses: An Infrared Spectroscopic Study. Contrib Mineral Petrol 81:1-17

Takeuchi S (2011) Preeruptive magma viscosity: An important measure of magma eruptibility. J Geophys Res 116:B10201

Thibault Y and Holloway JR (1994) Solubility of CO_2 in a Ca-rich leucitite: effects of pressure, temperature and oxygen fugacity. Contrib Mineral Petrol 116:216-224

Thornber CR, Roeder PL, Foster JR (1980) The effect of composition on the ferric-ferrous ration in basaltic liquids at atmospheric pressure. Geochim et Cosmochim Acta 44:525-532

Tobolsky AV and Taylor RB (1963) Viscoelastic properties of a simple organic glass. J Phys Chem 67:2439-2442

Tomiya A, Takahashi E, Furkawa N, Suzuki T (2010) Depth and Evolution of a Silicic Magma Chamber: Melting Experiments on a Low-K Rhyolite from Usu Volcano, Japan. J Petrol 51:1333-1354

Toplis MJ (1998) Energy barriers to viscous flow and the prediction of glass transition temperatures of molten silicates. Am Mineral 83:480-490

Toplis MJ, Dingwell DB, Lenci T (1997): Peraluminous viscosity maxima in Na2O-Al2O3-SiO2 liquids: The role of triclusters in tectosilicate melts. Geochim et Cosmochim Acta 61:2605-2612

Urbain G, Bottinga Y, Richet P (1982) Viscosity of liquid silica, silicate and alumina-silicates. Geochim et Cosmochim Acta 46:1061-1072

Vetere F, Behrens H, Holtz F, Vilardo G, Ventura G (2010) Visocsity of crystal-bearing melts and its implication for magma ascent. J Mineral Petrol Sci 105:151-163

Vona A, Romano C, Dingwell DB, Giordano D (2011) The rheology of crystal-bearing basaltic magmas from Stromboli and Etna. Geochim et Cosmochim Acta 75:3214-3236

Webb SL (1997): Silicate Melts. Lecture Notes in Earth Sciences vol 67

Webb SL (2005) Structure and rheology of iron-bearing Na_2O-Al_2O_3-SiO_2 melts. Eur J Mineral 17:223-232

Webb SL (2008) Configurational heat capacity of Na_2O-CaO-Al_2O_3-SiO_2 melts. Chem Geol 256:92-101

Webb SL (2011) Configurational heat capacity and viscosity of (Mg, Ca, Sr, Ba)O-Al_2O_3-SiO_2 melts. Eur J Mineral 23:487-497

Webb SL, Banaszak M, Köhler U, Rausch S, Raschke G (2007) The viscosity of Na_2O-CaO-Al_2O_3-SiO_2 melts. Eur J Mineral 19:681-692

Webb SL, Müller E, Büttner H (2004) Anomalous rheology of peraluminous melts. Am Mineral 89:812-818

White B and Montana A (1990) The effect of H_2O and CO_2 on the viscosity of sanidin liquid at high pressures. J Geophys Res 95:683-693

Whittington A, Richet P, Holtz F (2000) Water and the viscosity of depolymerized aluminosilicate melts. Geochim et Cosmochim Acta 64:3725-3736

Whittington A, Richet P, Linard Y, Holtz F (2001) The viscosity of hydrous phonolites and trachytes. Chem Geol 174:209-223

Wilke M (2005) Fe in magma – An overview. Annals GeoPhys 48:609-617

Zachariasen WH (19 32) The Atomic Arrangement in Glass. J Am Chem Soc 54:3841-385

2 Rheology of melts from the Colli Albani Volcanic District (Italy): a case study

Preface

This Chapter 2 contains the results on which further investigations are based (Chapters 3 and 4). The authors are Christin Kleest, Prof. Dr. Sharon Webb and Dr. Sara Fanara and their contribution is shown in Fig. P1.

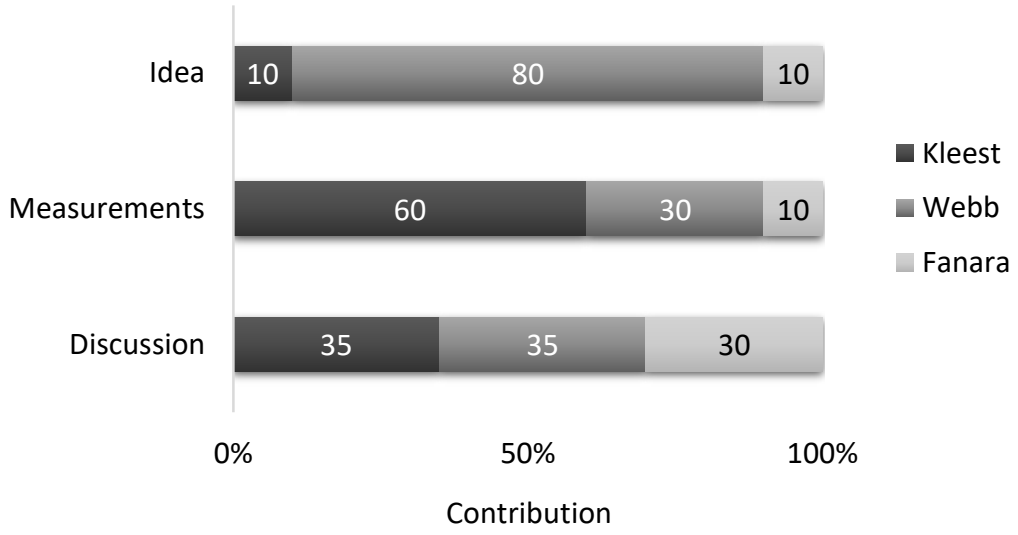

Fig. P1 Author contribution – divided in the parts idea, measurements and discussion – of the first publication of this thesis with the authors Christin Kleest, Prof. Dr. Sharon Webb and Dr. Sara Fanara. The legend gives the last names of the authors.

This Chapter was published on 14 August 2020 online in "Contribution to Mineralogy and Petrology", submitted on 21 December 2019 and accepted on 21 July 2020. On 10 October 2020 a correction to the online version edited containing corrections of typographical errors in the title and the "corrected" acknowledgement that was completely missing in the online publication from 14 August 2020. Therefore, these corrections are integrated in this 2nd Chapter as the corrections do not influence the results or other statements of this study.
The first page of this Chapter is given in the layout of the original article of the abstract follows by the layout corresponding to this thesis.

Contributions to Mineralogy and Petrology (2020) 175:82
https://doi.org/10.1007/s00410-020-01720-1

ORIGINAL PAPER

Rheology of melts from the Colli Albani Volcanic District(Italy): a case study

Christin Kleest[1] · Sharon L. Webb[1] · Sara Fanara[1]

Received: 21 December 2019 / Accepted: 21 July 2020

Abstract
In this study the first viscosity measurements in the glass transition range of melts from highly explosive large-volume eruptions from the Colli Albani Volcanic District (CAVD) are presented. The magmas are ultrapotassic, rich in iron and CaO and characterised by a low silica content (< 45 wt%). Melt compositions range from tephri-phonolitic to foiditic. The Colli Albani eruptions appear anomalous since they produced a large volume of erupted material in spite of their silica undersaturated compositions. The viscosity of the Colli Albani melt changes as the melt composition evolves from the original melt to a country-rock contaminated melt to a crystal-bearing melt with a permanent decrease in liquid viscosity. Conventional estimations of viscosities assume these magmas to have a low viscosity. The presented data show that the melt viscosities are higher than expected. Taking into account further chemical or rheological features of a melt, the investigated CAVD melts are not that striking as assumed in comparison with other large-volume eruptions. Consequently, considering the alkaline-earth to alkaline ratio together with the SiO_2 content could provide an alternative when comparing large volume eruptions.

Keywords Viscosity · Anhydrous melts · Colli Albani · Foidite · Glass transition · Low temperature

Communicated by Mark S. Ghiorso.

✉ Christin Kleest
christin.kleest@uni-goettingen.de

[1] Georg August Universität Göttingen, Abteilung Experimentelle Mineralogie, Goldschmidtstraße 1, 37077 Göttingen, Germany

Published online: 14 August 2020

Introduction

Rheology of magma has an enormous influence on the eruptive style of volcanoes as well as mass transfer in magmas or crystallisation and degassing processes in cooling melts. The rheology of a magma depends on composition X, temperature T, pressure P, the content of crystals, bubbles and vesicles, oxygen fugacity, shear and strain-rate induced crystallisation (i.e. Caricchi et al. 2007; Vona et al. 2011; Campagnola et al. 2016). Understanding eruption processes requires data at the appropriate P-T- and X conditions or modelling of the rheological and thermodynamic behaviour of melts using experimentally determined viscosity, heat capacity and configurational entropy data (e.g. Webb 2008; Russell and Giordano 2017).

In general, there is a positive correlation between the SiO_2 content and the viscosity of a melt, and highly viscous melts with a high silica content show typically an explosive eruptive style (Freda et al. 2011 and references therein). As shown by Freda et al. (2011), a way to illustrate the relationship between the erupted magma volume (a proxy for Volcanic Explosivity Index) and composition is to plot dense-rock equivalent (DRE) vs SiO_2 wt% (Fig. 1).

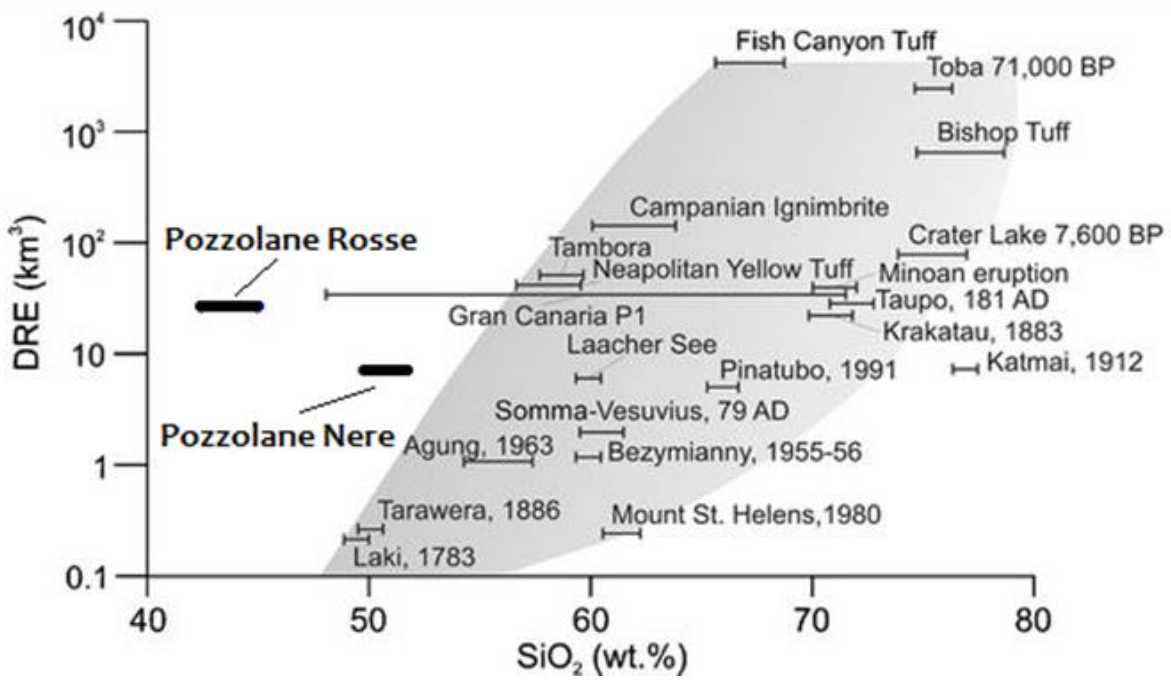

Fig. 1 Dense-rock equivalent (DRE) vs SiO_2 content showing the positive correlation between SiO_2 content and erupted volume with the exceptions of the Pozzolane Rosse and Pozzolane Nere events from the CAVD (after Freda et al. 2011 and references therein)

On this plot, the magmas of Pozzolane Rosse and Pozzolane Nere, characterised by a low silica content, constitute two striking exceptions. These events belong to the Colli Albani Volcanic District (CAVD) located about 20 km south of Rome. The CAVD is part of the ultrapotassic

Roman Volcanic Province, a volcanic belt parallel to the coast of the Tyrrhenian Sea and extending from southern Tuscany to central Latium (Peccerillo 2005). In its eruptive history, the CAVD had shown mainly explosive activity resulting in pyroclastic flow deposits accompanied by minor effusive activity that produced lava flows. In general, the products of the CAVD are characterised by a strong silica undersaturation and a high K content, shown in the TAS diagram in Fig. 2. The history of the CAVD is subdivided in three main periods characterised by dynamically different eruptive events (i.e. Karner et al. 2001; Giordano et al. 2006). The eruptions studied here belong to the earliest and most explosive phase: the Tuscolane-Artemisie phase (dated approx. 561-351 ka BP) (Karner et al. 2001), in which at least five of the largest pyroclastic flows were emplaced. The Pozzolane Rosse (PR) eruption with foiditic composition dated 456 ±3 ka (Marra et al. 2009) and the tephri-phonolitic Pozzolane Nere (PN) eruption dated 407 ±4 ka (Giordano et al. 2006) are the two largest eruptions of the CAVD. In spite of their low silica content, the PR and PN eruptions showed a highly explosive eruptive style. A low silica concentration and a high alkali content, in general (Fig. 2), implies a low viscosity melt which should result in an effusive eruption (i.e. Freda et al. 2011; Campagnola et al. 2016).

The magma chamber of the CAVD is seated in a thick Mesozoic-Cenozoic carbonate wall rock with depths up to 7-8 km (Chiarabba et al. 1997; Giordano et al. 2006; Iacono-Marziano et al. 2007a). Previous studies (i.e. Iacono-Marziano et al. 2007a; Freda et al. 2008; Boari et al. 2009) suggested that significant assimilation of these carbonate rocks into the magma chamber resulted in a liberation of CO_2 which consequently led to the generation of a CO_2-rich melt with the rate of carbonate assimilation depending on melt viscosity (Bluythe et al. 2015). Moreover, an excess of CO_2 is thought to trigger an explosive eruption (Iacono-Marziano et al. 2007a; Boari et al. 2009; Freda et al. 2011; Di Rocco et al. 2012). Fragments of mainly leucite, but also amounts of clinopyroxene and biotite are found in the pyroclastic units of the PR and PN eruptions (Giordano et al. 2006; Freda et al. 2011). The presence of these crystals in the magma chamber would have increased the viscosity of the magma and thus increased the probability of an explosive eruptive event (Freda et al. 2011; Campagnola et al. 2016). Therefore, previous investigations on the Colli Albani volcano concentrated on the effects of carbonate assimilation and the crystal content. Campagnola et al. (2016) investigated the viscosities of pure liquid and crystal-bearing products from the PN event from the CAVD. The samples were remelted from natural material of a tephri-phonolitic composition at superliquidus conditions (for crystal-free melts) and subliquidus conditions (for crystal-bearing melts). The experimental measurements demonstrated that the viscosities at lower temperatures are higher than expected.

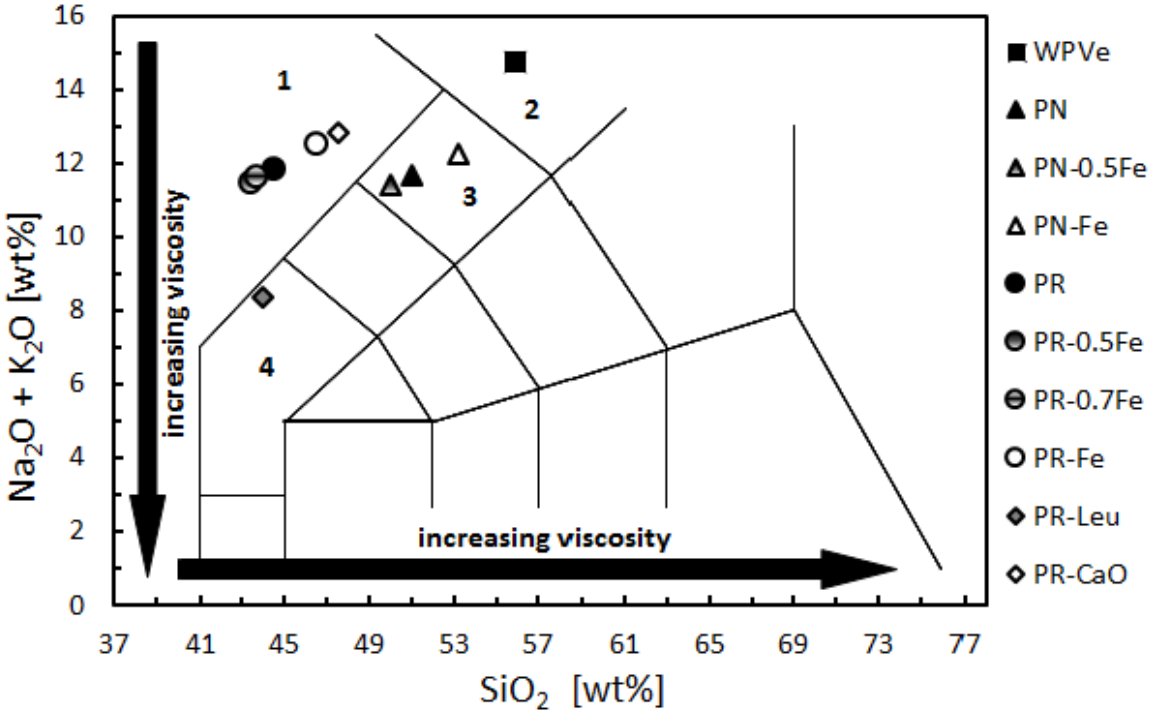

Fig. 2 TAS diagram with the compositions of the investigated melts with WPVe for White Pumice from the Vesuvius AD 79 eruption and composition after Iacono-Marziano et al. (2007b), PN for the Pozzolane Nere eruption from Colli Albani and composition after Campagnola et al. (2016), PN-0.5Fe for the modified PN composition with the half amount of iron, PN-Fe for the modified PN composition without iron, PR for the Pozzolane Rosse eruption from Colli Albani and composition after Freda et al. (2010), PR-0.5Fe for the modified PR composition with the half amount of iron, PR-0.7Fe for the modified PR composition with 30% of iron, PR-Fe for the modified PR composition without iron, PR-Leu for the PR composition minus 4 mol% $KAlSi_2O_6$ and PR-CaO for the PR composition minus 7 wt% CaO and 1- foidite, 2- phonolite, 3- tephri-phonolite, 4- tephrite. Arrows indicate conventional estimations for the viscosity of a magma

In this study, the first viscosity measurements of melt compositions from both the PR and PN event of the CAVD are presented to study their rheological features at sub-liquidus conditions in the glass transition range. Five different compositions are investigated: the K-foidite of the Pozzolane Rosse eruption (PR) with the composition taken from Freda et al. (2011), and another K-foidite that is calculated with the original PR composition minus 7 wt% CaO to represent the viscosity of the melt before its assimilation of the carbonate wall rocks (PR-CaO). To investigate the rheology of the melt after leucite crystallization, 4 mol% $KAlSi_2O_6$ were subtracted from the whole rock composition which results in a tephrite basanite (PR-Leu). The fourth composition is the tephri-phonolite from the Pozzolane Nere eruption (PN) with the whole rock composition of Campagnola et al. (2016). In addition, the more silicic “white pumice” phonolite from the Vesuvius AD 79 eruption (WPVe) (Iacono-Marziano et al. 2007b)

is investigated in order to represent the acid end-member of the K-rich volcanism of central Italy.

Starting materials

Synthetic glasses with the composition of the PR and PN events from the CAVD as well as the modified compositions of PR-Leu and PR-CaO and the WPVe from the Vesuvius AD 79 eruption were prepared from powdered oxides and carbonates of SiO_2, Al_2O_3, Na_2CO_3, TiO_2, Fe_2O_3, MnO, MgO, $CaCO_3$ and K_2CO_3 previously dried at 500 °C for 12 hours with the exception of MgO that was dried at 1000 °C. The mixed powders were decarbonated at a slow heating rate to 1000 °C overnight. The mixture was melted in a $Pt_{90}Rh_{10}$ crucible for 1 hour at 1600 °C and quenched by dipping the crucible in water. To improve the homogenisation, the melts were crushed and remelted twice for 1 hour before the last melting at 1600°C for 4 hours. Both optical microscopy and microprobe analysis demonstrated the starting glasses were free of bubbles and crystals. Extra glasses of PN and PR were synthesized with lower amounts of iron in order to avoid effects of crystals growing during viscosity measurements. A second PN composition was synthesized with half the original iron content (PN-0.5Fe), and two extra PR melts were synthesized with half the amount of iron (PR-0.5Fe) and with 30% of its iron (PR-0.7Fe). Another set of PR and PN glasses were made iron-free (PR-Fe and PN-Fe, respectively). The composition of these melts were calculated based on the iron ratio (Fe^{2+}/Fe_{tot}) of the iron-bearing melts, and the ferric iron was replaced by Al^{3+} and the ferrous iron was replaced by Mg^{2+}. The chemical compositions and iron ratios of all glasses investigated in this study are shown in Table 1.

Electron microprobe analysis												
[wt %]	SiO_2	Al_2O_3	Na_2O	TiO_2	FeO	MnO	MgO	CaO	K_2O	total	Fe^{2+}/Fe_{tot}	M [g mol^{-1}][a]
WPVe	55.91±0.16	21.47±0.10	5.29±0.08	0.30±0.02	2.72±0.05	0.13±0.03	0.41±0.02	3.25±0.05	9.48±0.08	98.96	0.42±0.02	69.44
PN	51.02±0.16	19.47±0.10	2.54±0.06	0.64±0.02	7.28±0.09	0.19±0.03	2.37±0.04	5.56±0.06	9.13±0.08	98.20	0.44±0.02	69.50
PN-0.5Fe	50.01±0.16	22.41±0.10	2.50±0.06	0.63±0.02	5.82±0.08	0.19±0.02	3.25±0.03	5.47±0.06	8.92±0.08	99.20	0.44±0.03	69.42
PN-Fe	53.24±0.15	22.48±0.10	2.62±0.06	0.68±0.02	-	-	4.61±0.05	5.72±0.06	9.62±0.08	98.97	-	67.06
PR	44.42±0.15	16.46±0.09	3.17±0.06	0.93±0.02	9.46±0.10	0.20±0.03	3.94±0.05	10.82±0.09	8.73±0.08	98.13	0.39±0.01	68.08
PR-0.5Fe	43.30±0.15	19.84±0.10	3.04±0.06	0.92±0.04	7.46±0.09	0.20±0.02	5.44±0.04	10.55±0.09	8.47±0.08	99.22	0.36±0.03	68.22
PR-0.7Fe	43.62±0.15	21.46±0.10	3.10±0.06	0.92±0.04	5.10±0.07	0.21±0.02	5.45±0.04	10.71±0.09	8.58±0.08	99.15	0.37±0.02	67.83
PR-Fe	46.47±0.15	20.41±0.10	3.22±0.06	1.02±0.03	-	-	6.87±0.07	11.25±0.09	9.37±0.08	98.61	-	65.35
PR-Leu	43.95±0.15	15.80±0.09	3.71±0.07	1.11±0.03	11.13±0.10	0.25±0.03	4.63±0.05	12.82±0.09	4.66±0.06	98.06	0.42±0.02	67.34
PR-CaO	47.57±0.15	17.68±0.09	3.42±0.07	1.04±0.03	10.25±0.10	0.23±0.03	4.23±0.05	4.26±0.05	9.44±0.08	98.12	0.42±0.01	69.62
Calculated compositions												
[mol %]	SiO_2	Al_2O_3	Na_2O	TiO_2	FeO	Fe_2O_3	MnO	MgO	CaO	K_2O	γ[b]	
WPVe	65.18±0.32	14.75±0.12	5.98±0.15	0.26±0.03	1.11±0.03	0.77±0.03	0.13±0.05	0.71±0.06	4.06±0.11	7.05±0.10	0.55	
PN	59.81±0.29	13.46±0.11	2.88±0.11	0.57±0.03	3.14±0.06	2.00±0.03	0.19±0.05	4.14±0.11	6.99±0.12	6.83±0.09	0.61	
PN-0.5Fe	58.03±0.31	15.33±0.12	2.81±0.09	0.55±0.04	2.49±0.05	1.58±0.04	0.18±0.03	5.62±0.09	6.80±0.13	6.61±0.10	0.59	
PN-Fe	60.04±0.32	14.94±0.12	2.86±0.12	0.58±0.03	-	-	-	7.75±0.16	6.91±0.14	6.92±0.11	0.62	
PR	51.29±0.25	11.20±0.09	3.55±0.11	0.81±0.03	3.57±0.06	2.79±0.04	0.19±0.04	6.77±0.13	13.39±0.16	6.43±0.09	0.71	
PR-0.5Fe	49.29±0.26	13.31±0.10	3.35±0.10	0.79±0.05	2.56±0.04	2.27±0.04	0.19±0.03	9.23±0.10	12.86±0.17	6.15±0.09	0.69	
PR-0.7Fe	49.49±0.27	14.35±0.10	3.41±0.10	0.78±0.05	1.79±0.04	1.52±0.03	0.20±0.03	9.22±0.11	13.02±0.17	6.21±0.09	0.68	
PR-Fe	51.26±0.28	13.27±0.11	3.44±0.11	0.85±0.04	-	-	-	11.30±0.19	13.30±0.18	6.59±0.09	0.72	
PR-Leu	49.86±0.25	10.56±0.09	4.09±0.11	0.95±0.04	4.43±0.06	3.06±0.04	0.25±0.04	7.84±0.12	15.59±0.16	3.37±0.08	0.72	
PR-CaO	55.80±0.26	12.22±0.10	3.89±0.12	0.92±0.04	4.22±0.06	2.92±0.05	0.23±0.04	7.39±0.13	5.35±0.11	7.07±0.09	0.65	

[a] M is calculated by normalising the total weight of each oxide to one mole of the sample

[b] $\gamma = \frac{Na_2O+K_2O+CaO+MgO+FeO}{Na_2O+K_2O+CaO+MgO+FeO+Al_2O_3+Fe_2O_3}$

Table 1 Chemical compositions of the investigated melts determined by electron microprobe analysis (JEOL JXA 8900 RL) with 15 kV acceleration voltage, 15 nA current and 25 µm beam diameter. Listed data are the average of 20 single measurements (in wt %). Standard deviation is 1σ. The data in mol % are calculated using the atomic analysis combined with the Fe-ratio determined by colorimetric micro-determination, here the standard variation is 2σ

Micropenetration technique

Viscosities η were determined in the range $10^{8.5}$ – $10^{13.5}$ Pa s using the micropenetration method. The measurements were carried out with a Netzsch TMA 402 Dilatometer. Glass discs, 3 mm thick, were polished to give 2 parallel faces before measurements. Depending on the viscosities, the duration of the measurements varied between 30 min and 3 hours within a temperature range of 630 - 810 °C. The measurements were done in air in a sequence that alternates between lower and higher temperatures to ensure that the determined viscosity was not affected by crystallisation. The temperature in the dilatometer was calibrated to ±0.5 °C with the melting points of Bi (268.02 °C), Zn (417.02 °C), Al (659.02 °C), NaCl (800.05 °C) and Ag (951.09 °C). The standard glass DGG1, a Na_2O-CaO-SiO_2 float glass from the Deutsche Glastechnische Gesellschaft was used to determine the precision of the dilatometer which is ±0.06 $\log_{10}$ Pa s. Hence, the total error of ±0.06 $\log_{10}$ Pa s (1σ) is assigned for each measured viscosity. A polished sphere of single crystal Al_2O_3 with 2 mm diameter was forced into the discs using 0.1 - 1.5 N. Viscosity is calculated from the rate of penetration of the sphere into the melt by:

$$\eta = \frac{0.1875\, Ft}{r^{0.5} l^{1.5}} \quad (1)$$

with F – the applied force, t – time, r – radius of the indent sphere, l – distance of indent (Pocklington 1940; Tobolsky and Taylor 1963; Dingwell et al. 1992). Indent data obtained for timescales less than 100 τ (τ- relaxation time) after the application of the force were not included in the determination of viscosity.

Differential scanning calorimetry

The heat capacities were measured in a Netzsch DSC 404C differential scanning calorimeter in an argon atmosphere. Discs of the samples with polished parallel surfaces and weights between 52 and 82 mg were first heated to a temperature of about T_g^9 (the temperature at which the viscosity is 10^9 Pa s) with a rate of 20 °C min^{-1} and cooled with the same rate. The heat capacity of these glasses with a fictive temperature set by the 20 °C min^{-1} cooling rate were then measured at a 20 °C min^{-1} heating rate. The samples in a Pt crucible were measured against an empty Pt crucible. The calibration of the calorimeter was done with a single sapphire crystal (m = 113.140 ± 0.005 mg) and the heat capacity data of Robie et al. (1978). The error of the measurements is ≤ 1%. The configurational heat capacity (C_p^{conf}) was calculated as the difference between the liquid heat capacity (C_{pl}) and the glass heat capacity (C_{pg}) extrapolated

to the same temperature as the liquid heat capacity. The heat capacity of the glass (c_{pg}) is determined by the extrapolation of the Maier-Kelley-Fit to the unrelaxed glass heat capacity:

$$c_{pg} = a + bT + cT^{-2} \quad (2)$$

with a, b and c as parameters and T – temperature in Kelvin (Maier and Kelley 1932).

Determining the heat capacities of all of the melts (c_{pl}) is not possible due to crystallisation during the measurements. Therefore, c_{pl} and C_p^{conf} are modelled after Giordano and Russell (2017) and Russell and Giordano (2017) as discussed below.

Colorimetric micro-determination of the iron species

The colorimetric micro-determination of the ferrous and ferric iron ratio in silicic glasses was first developed by Wilson (1960) and modified by Schuessler et al. (2008). This method involves measurement of the ferrous iron species by UV/VIS spectroscopy. Each sample is crushed and 4 – 10 mg of the powdered glass is dissolved in hydrofluoric acid (HF). The bivalent iron builds a reddish Fe(II)-bipyridyl-complex with 2:2´bipyridyl added to the solution that shows an intensive absorption band at approx. 523 nm. Measurements of the total iron content are obtained by reducing the ferric iron into the ferrous species with hydroxylamine hydrochloride (H_4NOCl). The total iron content of the sample is determined by comparing the absorption of the sample with a series of standards with known ferrous iron concentrations. UV/VIS measurements were done with an AvaSpec-UV/VIS/NIR spectrometer from Avantes and the software AvaSoft Version 8.3. The ratio of the ferrous to total iron in the sample is directly acquired from the ratio of the absorbances at 523 nm. The iron ratios Fe^{2+}/Fe_{tot} are given in Table 1.

Results and discussion

All the investigated melts are metaluminous defined by $Na_2O + K_2O < Al_2O_3 < CaO + MgO + Na_2O + K_2O$ in mole fraction (Shand 1927). An estimation of the degree of depolymerisation and hence of the melt structure is $\gamma = (Na_2O + K_2O + CaO + MgO + FeO)/(Na_2O + K_2O + CaO + MgO + FeO + Al_2O_3 + Fe_2O_3)$ in mole fraction (Toplis et al. 1997; Webb et al. 2007) which ranges from 0.55 for WPVe to 0.72 for PR-Fe and PR-Leu. The γ values are given in Table 1. The iron ratio (Fe^{2+}/Fe_{tot}) was found to be in the range from 0.36 – 0.44 (see Table 1). All samples were synthesised at the same temperature (1600 °C) and oxygen fugacity (in air) and

were quenched at the same rate at 0.1 MPa. Kress & Carmichael (1991) developed a model for the calculation of the iron ratio of silicate melts in dependence of composition, temperature, oxygen fugacity and pressure. A comparison with the Fe^{2+}/Fe_{tot} calculated by this model and the measured Fe^{2+}/Fe_{tot} shown in Fig. 3 illustrates that the modelled iron ratios are within the error of the measured values, showing this model works well for the studied melt compositions.

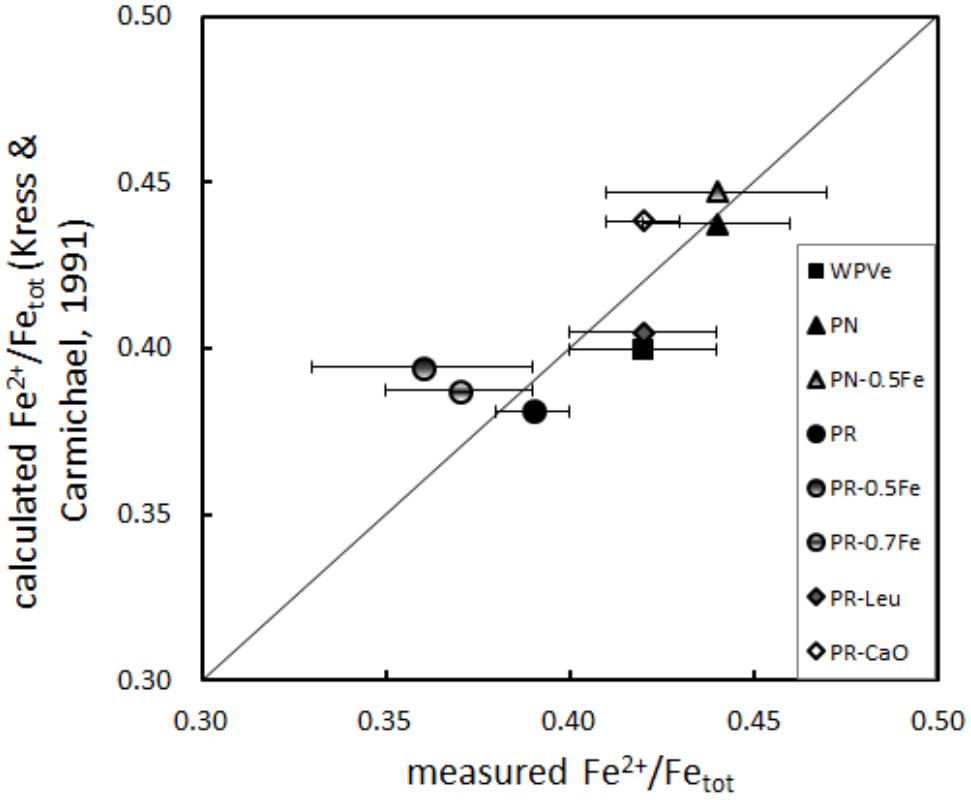

Fig. 3 Comparison of measured iron ratios with calculated iron ratios after Kress & Carmichael (1991) and the 1:1 line.

Viscosity

The samples investigated in this study were found to be free of bubbles and crystals by optical microscopy and scanning electron microscopy (SEM) with magnifications up to 10^6 times. However, Raman spectroscopy indicated the presence of nanolites. Fig. 4 shows the Raman spectra for sample PR-CaO exhibiting the highest nanolite content represented by the peak at approx. 680 cm^{-1} belonging to magnetite with the clear glass "hump" in the area of approx. 950 cm^{-1}.

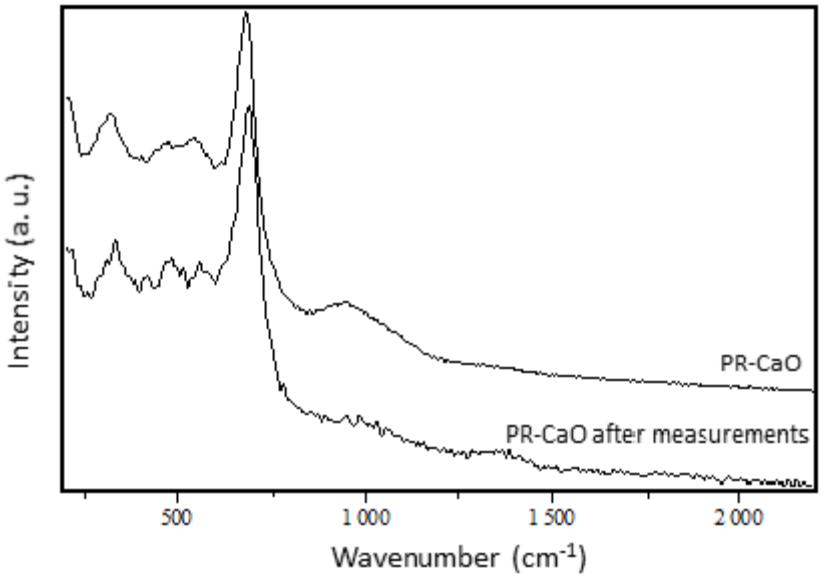

Fig. 4 Raman spectra of the sample PR-CaO. The upper spectrum is from the glass before viscosity measurements and the lower one is that from the glass after viscosity measurements

This is in agreement with the observations from Di Genova et al. (2017) who recognised the effect of nanolites in Fe-bearing glasses on the Raman spectra. The ratio of the peaks is reduced after the viscosity measurements with respect to the spectra obtained before the viscosity measurements. This indicates an increase in the nanolite content. As due to the fact that the nanolites in the post-viscosity glasses are not visible in the SEM, they are assumed to be so small and unconnected that their presence would have an insignificant effect on the viscosity. Stevenson et al. (1996) showed that a crystal fraction of 0.01 or less in homogenous distribution in the melt and without any connectivity has negligible influence on the viscosity. However, accounting the effect of crystallisation of magnetite depleting the residual melt in Fe_3O_4, the viscosity of the chemically changed residual liquid is modelled with a crystal content of 2 vol% and discussed below.

Measured viscosities are listed in Table 2.

WPVe		PN		PN-0.5Fe		PN-Fe		PR	
T [°C]	$\log_{10}$ η [Pa s]	T [°C]	$\log_{10}$ η [Pa s]	T [°C]	$\log_{10}$ η [Pa s]	T [°C]	$\log_{10}$ η [Pa s]	T [°C]	$\log_{10}$ η [Pa s]
678.3	12.68	697.2	12.87	702.6	13.1	682.5	13.34	637.2	13.78
697.3	12.13	707.3	12.62	717.7	12.72	702.6	12.44	667.2	12.68
717.3	11.45	717.3	12.36	732.8	12.02	722.7	12.09	687.2	12.26
737.3	10.91	727.3	12.07	742.8	11.89	732.8	11.72	707.3	11.60
757.3	10.54	737.3	11.84	752.9	11.39	743.0	11.38	717.3	11.27
777.3	10.12	747.3	11.59	763.0	11.14	783.3	10.12	727.3	10.77
817.3	9.13	757.3	11.05	773.1	10.89	803.3	9.59	737.3	10.66
		767.3	10.66	783.2	10.41	823.9	9.01	767.3	9.58
				803.3	10.09	843.5	8.58		
				813.4	9.89				

PR-0.5Fe		PR-0.7Fe		PR-Fe		PR-Leu		PR-CaO	
T [°C]	$\log_{10}$ η [Pa s]	T [°C]	$\log_{10}$ η [Pa s]	T [°C]	$\log_{10}$ η [Pa s]	T [°C]	$\log_{10}$ η [Pa s]	T [°C]	$\log_{10}$ η [Pa s]
652.2	13.61	642.2	13.40	642.2	13.61	627.2	12.88	677.3	12.91
672.4	12.87	662.3	12.80	702.6	11.82	647.2	12.54	707.3	12.21
697.5	12.00	682.4	11.97	722.7	10.85	657.2	11.81	717.3	11.75
712.6	11.25	702.6	11.19	742.9	10.29	677.2	11.51	727.3	11.58
722.7	10.97	712.6	10.86	763.0	9.59	687.2	11.61		
741.8	10.31	722.7	10.33	783.1	9.25	707.3	10.87		
752.9	9.81	742.9	9.59	803.3	8.28	727.3	10.19		
768.1	9.48	763.3	8.95			747.3	9.35		
783.2	9.13	783.4	8.41			767.4	9.14		
803.6	8.73								

Table 2 Measured viscosities at given temperatures. The error in viscosity is ±0.06 $\log_{10}$ Pa s, the error in temperature is ±0.5 °C

The best fit for viscosity measurements over the present temperature range is the Arrhenius Equation

$$log_{10}\eta = A + \frac{B \cdot 10^4}{T} \quad (3)$$

with *A* and *B* as fit parameters and *T* – temperature in Kelvin. An equation more complex than a straight line fit to $\log_{10}$ η as a function of inverse temperature is not statistically possible due to the small range in both viscosity and temperature over which the data are obtained. The fitted parameters of the Arrhenius Equation are given in Table 3.

	A [$\log_{10}$ Pa s]	B [K]	T_g^{12} [K]	m
WPVe	-14.80±0.06	2.61±0.01	973.6	26.8
P.N.	-18.96±0.45	3.10±0.07	1001.1	31.0
PN-0.5Fe	-19.58±0.19	3.19±0.03	1009.4	31.6
PN-Fe	-19.69±0.05	3.15±0.01	995.0	31.7
PR	-19.13±0.15	3.00±0.02	964.2	31.1
PR-0.5Fe	-22.71±0.10	3.36±0.02	967.7	34.7
PR-0.7Fe	-25.24±0.07	3.55±0.01	953.1	37.2
PR-Fe	-21.43±0.19	3.22±0.03	963.2	33.4
PR-Leu	-15.24±0.52	2.54±0.09	932.9	27.2
PR-CaO	-14.26±0.26	2.58±0.05	984.2	26.3

Table 3 Fit parameters from the Arrhenius Equation (Eq. 3) using the viscosity data and T_g^{12} and fragility m (Eq. 4)

The measured viscosities for the melts with the original iron content of the whole rock composition are plotted in Fig. 5 as a function of inverse temperature. The viscosity data of a MORB melt (Webb et al. 2014) are plotted for comparison, showing that the MORB viscosity is lower than that of the foiditic PR and the tephri-phonolitic PN. At the fixed temperature of 700 °C, the most viscous melt from this study is the PN composition (12.89 $\log_{10}$ Pa s) being nearly 1.2 orders of magnitude higher than that of PR (11.72 $\log_{10}$ Pa s). PR-Leu is 0.85 $\log_{10}$ Pa s lower than PR as expected since network formers are removed to form this melt composition. As a result of subtracting the network modifying CaO from PR (PR-CaO) the viscosity increases by 0.58 $\log_{10}$ Pa s. At temperatures above 730 °C, the crystallisation, detected by optical microscopy and X-ray diffraction, affects the viscosity of PR-CaO, resulting in an increase in viscosity by nearly two orders of magnitude. Therefore, the data of obviously crystal bearing melts are not presented here. The melt with the highest SiO_2 content, WPVe,

shows viscosities lying in the middle of the viscosity range of the investigated melt compositions. Thus, the viscosities of the investigated melts are not as low as assumed although they have a silica-poor and K-rich composition.

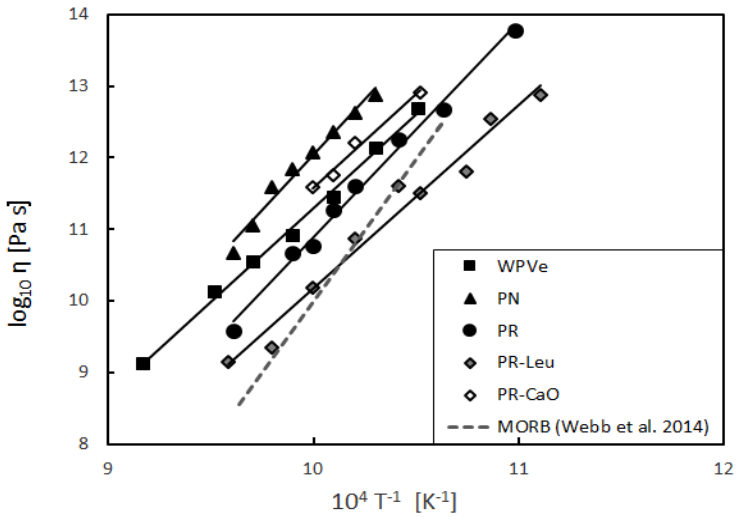

Fig. 5 Viscosities as a function of inverse temperature of the investigated melts with the original iron content in comparison with a MORB (dotted line) (Webb et al. 2014)

The viscosities of the PN series are presented in Fig. 6 and Table 2. The viscosity of PN-Fe is ~0.5 $\log_{10}$ Pa s lower than that of PN-0.5Fe and around 0.2 $\log_{10}$ Pa s lower than the viscosity of PN with the original iron content. The viscosity data of the anhydrous remelted natural PN melt from Campagnola et al. (2016) are also shown in Fig. 6. The measured viscosities in this study are ~1 order higher than those from Campagnola et al. (2016). The Einstein-Roscoe viscosity model (Einstein 1906; Roscoe 1952) as well as that of Caricchi et al. (2007) require 35 vol% crystal content to increase viscosity by one order of magnitude. Due to this discrepancy, the standard glass DGG1 was remeasured to confirm the accuracy of both the dilatometer measurements and the data evaluation.

The Arrhenius plots of the original and modified PR melts are shown in Fig. 7 and data are listed in Table 2. The PR-0.7Fe composition shows slightly lower viscosities over the whole viscosity range compared to the other PR melts with a deviation of ~0.7 $\log_{10}$Pa s.

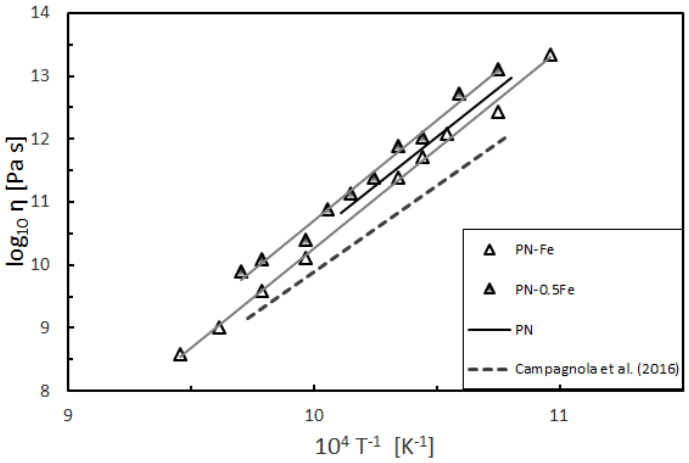

Fig. 6 Viscosity data of the PN series ($0.59 < \gamma < 0.62$) as a function of inverse temperature. Dotted line are the viscosity data of PN measured by Campagnola et al. (2016)

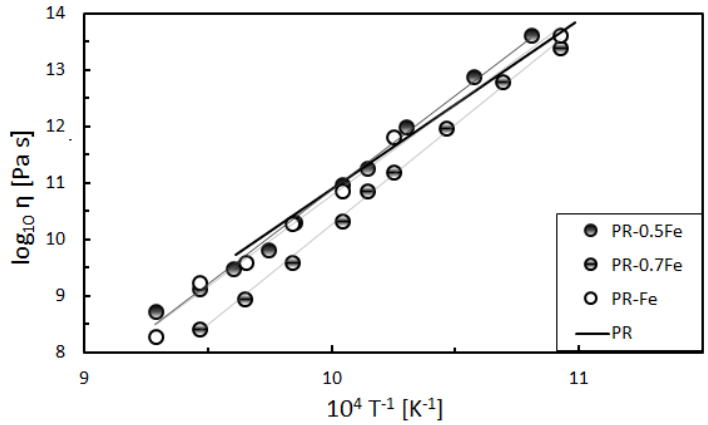

Fig. 7 Viscosity data of the PR series ($0.68 < \gamma < 0.72$) as a function of inverse temperature

As illustrated in Fig. 8, which shows the glass transition temperature T_g^{12} (the temperature at which the viscosity is 10^{12} Pa s) as a function of γ, there is a decreasing trend of viscosity with increasing γ, with the exception of the WPVe melt which will follow a different compositional trend as it is poor in alkaline-earths compared to the other melts. This T_g^{12} trend has been extensively discussed in the literature (i.e. Richet 1984; Toplis 1998; Webb et al. 2004, 2005, 2007) and is due to the increase in the amount of non-bridging oxygens as the bridging oxygens of the Si-O and tetrahedral Al-O bonds are broken by the network modifiers. This trend is generally observed within the investigated melt series of the CAVD in spite of relatively small variation in the viscosity within the PR composition series.

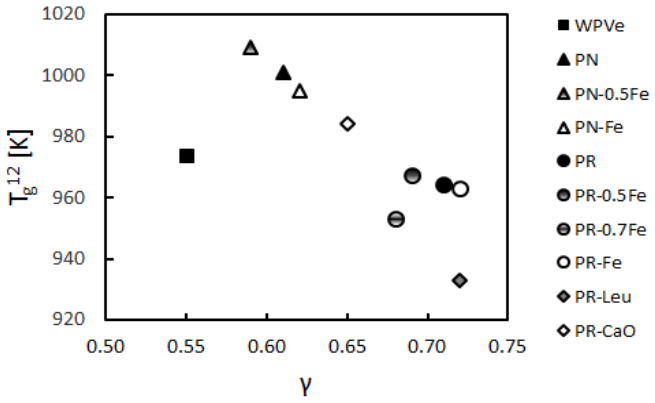

Fig. 8 T_g^{12} as a function of γ

Fragility

Using the viscosity data the fragility m is calculated from the equation

$$m = \frac{B \times 10^4}{T_g^{12}} \tag{4}$$

with B – parameter of the Arrhenius fit (Eq. 3) in Kelvin and T_g^{12} – temperature at which the viscosity is 10^{12} Pa s in Kelvins (Toplis et al. 1997; Webb 2011). The values of m and T_g^{12} are reported in Table 3. Fragility is a value indicating the deviation from an Arrhenian behaviour. The series of PR compositions exhibit the highest fragilities (31.1 to 37.2), followed by the series of PN compositions (31.0 to 31.7), PR-Leu (27.2), WPVe (26.8) and PR-CaO (26.3).

Calorimetry

The fit parameters a, b and c of the Maier-Kelley Equation (Eq. 2) are shown in Table 4. For WPVe, PN-Fe, PR-0.7Fe and PR-Fe, a determination of c_{pl} is possible. It was not possible to obtain a c_{pl} value for the other melts due to crystallisation at the given temperature. As the value of C_p^{conf} is required in the Adam-Gibbs description of viscosity as a function of temperature (Adam and Gibbs 1965; Richet 1984, 1987; Toplis et al. 1997; Webb 2008), the relationship of Giordano and Russell (2017) is used to estimate C_p^{conf}.

Table 4 shows the calculated data. To treat all calorimetry data and resultant values equally, C_{pl} and C_p^{conf} are calculated for all investigated melts after Giordano and Russell (2017). However, these values have to be regarded as a first approximation of the heat capacities since the correlation from Giordano and Russell (2017) does not include foiditic, tephri-phonolitic or phonolitic compositions and it assumes the same iron speciation for all melts.

	Maier-Kelley parameters							
	a	b	c	c_{pg}	C_{pl} [a]	C_p^{conf} [b]	S^{conf} [c]	B_e [c]
	[J g^{-1} K^{-1}]	[J g^{-1} K^{-2}]	*10^3 [J g^{-1} K]	[J g^{-1} K^{-1}]	[J mol^{-1} K^{-1}]	[J mol^{-1} K^{-1}]	[J mol^{-1} K^{-1}]	[kJ mol^{-1}]
WPVe	1.151±0.001	35.47± 1.29	-48.72±0.19	1.15	94.95	16.28	21.74±1.34	779.50±46.81
PN	1.229±0.003	-75.05±2.91	-57.99±0.44	1.10	95.73	19.63	20.90±3.03	774.16±111.40
PN-0.5Fe	1.222±0.002	-63.62±1.75	-53.15±0.27	1.11	97.46	20.75	19.99±1.27	742.61±46.37
PN-Fe	1.139±0.002	79.61±1.44	-47.50±0.21	1.18	97.53	19.07	17.46±0.90	638.70±31.96
PR	1.158±0.003	-15.76±2.93	-49.16±0.42	1.10	98.66	24.66	25.77±2.39	918.35±83.90
PR-0.5Fe	0.993±0.010	134.48±8.65	-63.02±2.12	1.08	97.41	25.78	20.10±0.82	714.09±28.01
PR-0.7Fe	1.324±0.002	-65.95±2.11	-70.87±0.29	1.19	105.46	25.22	17.26±0.98	603.99±33.14
PR-Fe	1.158±0.003	39.51±2.81	-54.16±0.45	1.15	98.60	24.10	20.70±2.20	730.95±74.68
PR-Leu	1.021±0.001	161.08±1.62	-35.25±0.22	1.15	102.14	25.78	33.06±6.07	1141.00±204.03
PR-CaO	1.257±0.002	-92.47±2.27	-57.62±0.35	1.11	103.95	22.42	35.98±9.17	1304.51±331.79

[a] C_{pl} calculated using C_p^{conf} after Giordano and Russell (2017)

[b] C_p^{conf} calculated via $C_p^{conf} = 52.6 - 55.88X_{SiO2}$ with X_{SiO2} – mole fraction of the SiO_2 content of the melt (Giordano and Russell 2017)

[c] S^{conf} and B_e fitted via Eq. 5

Table 4 Heat capacity, configurational heat capacity, configurational entropy and the parameters for the Maier-Kelley Equation (Eq. 2)

The calculated C_p^{conf} is plotted vs γ in Fig. 9. It shows a general positive correlation between γ and C_p^{conf}. WPVe with the lowest value of γ (0.55) has the lowest C_p^{conf} (16.28 J mol^{-1} K^{-1}). The highest values of C_p^{conf} are calculated for PR-0.5Fe and for PR-Leu (25.78 J mol^{-1} K^{-1}) with values of γ of 0.69 and 0.72, respectively. As pointed out by Giordano and Russell (2017) an increase in the SiO_2 content of a melt leads to a decreasing C_p^{conf}. The same conclusion is reached by Russell and Giordano (2017) who concluded that an increasing SiO_2 accompanied with a rising degree of polymerisation would result in a less re-ordering of the melt structure at the glass transition and therefore a lower C_p^{conf}.

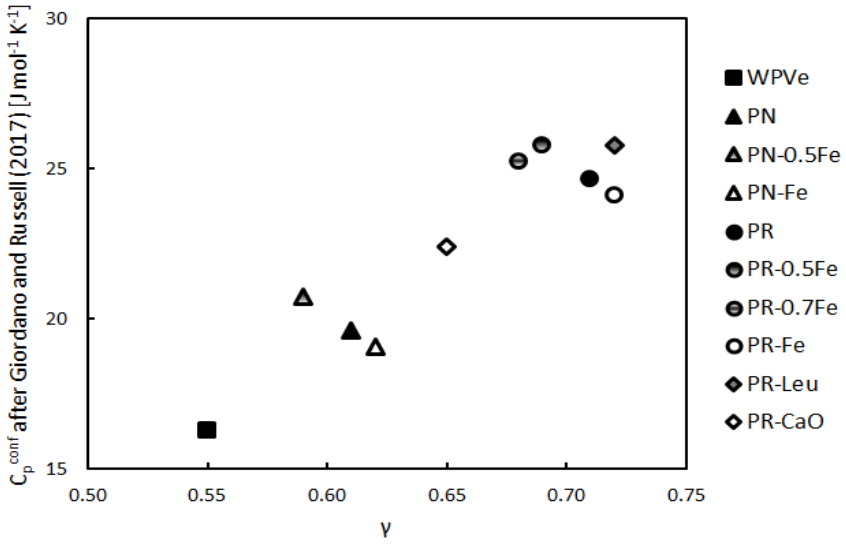

Fig. 9 C_p^{conf} as a function of γ. C_p^{conf} is estimated after $C_p^{conf} = 52.6 - 55.88X_{SiO2}$ (with X_{SiO2} – mole fraction of the SiO_2 content) showing an increase with increasing γ

Combining the viscosity data and the calculated C_p^{conf} enables the evaluation of the configurational entropy (S^{conf}) using the Equation

$$log_{10}\,\eta = A_e + \frac{B_e}{\ln 10\left[s^{conf}(T_g^{12}) + \int_{T_g^{12}}^{T} \frac{C_p^{conf}}{T} dT\right]T} \qquad (5)$$

(Richet 1984; Webb 2008; Falenty and Webb 2010) with A_e and B_e as constants, T – temperature in Kelvin and T_g^{12} – glass transition temperature in Kelvin, conventionally assumed as the temperature at which the viscosity is 10^{12} Pa s. This Equation presumes that there is no change in S^{conf} for temperatures lower than T_g^{12}. The value for the parameter A_e is a highly debated topic. This parameter represents the viscosity at infinite temperature (Toplis 1998) and is assumed to be constant for all silicate melts and thus independent of composition (Toplis et al.

1997; Giordano et al. 2008). In 1998, Toplis found A_e = -2.6 ± 1 $\log_{10}$ Pa s. Russell et al. (2003) postulated this high temperature parameter to be -3.2 ± 0.66 $\log_{10}$ Pa s for the Adam Gibbs theory. In a model from Giordano et al. (2008) the parameter is found to be -4.55 ± 0.21 $\log_{10}$ Pa s as the optimal value. In more recent studies, Russell and Giordano (2017) set A_e = -3.51 ± 0.25 $\log_{10}$ Pa s for their model and Robert et al. (2019) compared modelling with A_e = -3.51 $\log_{10}$ Pa s with a varying A_e. They conclude that a model with a variable A_e (-2.4 to -4.0 $\log_{10}$ Pa s) fits better to measured data. In this study, A_e is based on the Maxwell relation $\tau = \eta_0/G$ (with τ - relaxation time, η_0 - time-indepentent Newtonian viscosity and G - elastic shear modulus) with $\tau_0 = 10^{-14}$ s (τ_0 is the vibration frequency at $T^{-1} = 0$) (Martinez & Angell 2001; Angell et al. 2003) and G_∞ = 10 ± 0.5 GPa (G_∞ is the shear modulus at infinite frequency) (Dingwell & Webb 1989) and is calculated to be -4.00 $\log_{10}$ Pa s. This value lies in the range of the parameter discussed above. Parameters B_e and S^{conf} are fitted from the viscosity data using the calculated C_p^{conf} values after Giordano and Russell (2017) and the fixed A_e. Fitting the viscosity data to the Adam-Gibbs Equation allows the extrapolation of viscosity through temperature space from the low temperatures of the measurements to the high temperatures of geological processes.

A comparison of the fitted S^{conf} by Eq. 5 and the calculated S^{conf} after Russell and Giordano (2017) is seen in Fig. 10.

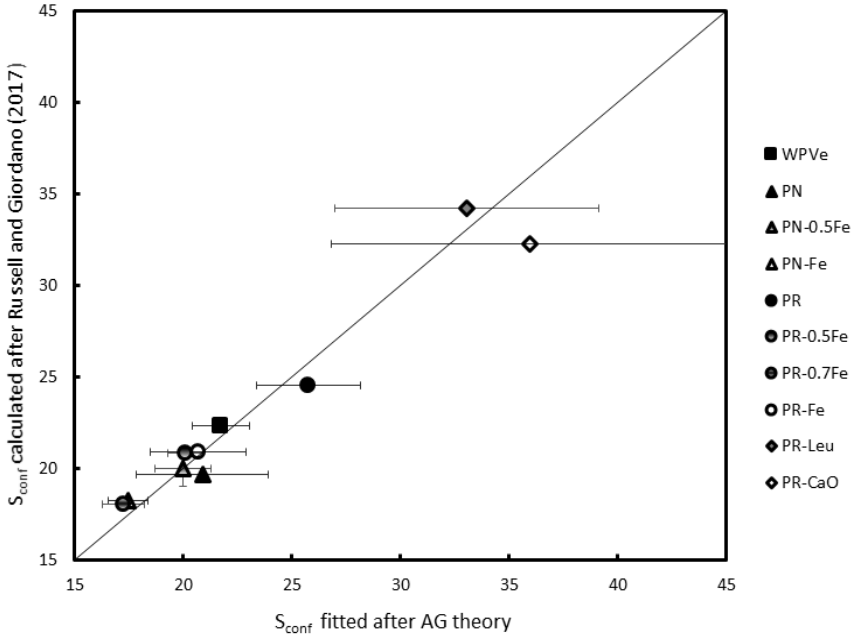

Fig. 10 Comparison of fitted S^{conf} using the Adam Gibbs model (Eq. 5) und the calculated ones after a correlation from Russell and Giordano (2017)

The greatest deviations occur for PR-Leu and PR-CaO. However, all fitted values for S^{conf} (Eq. 5) are within the errors given by Russell and Giordano (2017). Hence, the correlation after Russell and Giordano (2017) works quite well for the studied melts. For further modelling processes, fitted S^{conf} after Eq. 5 are used.

The value for S^{conf} is lowest for the PR-0.7Fe composition (17.26 J mol^{-1} K^{-1}) and highest for PR-CaO (35.98 J mol^{-1} K^{-1}) as it is shown in Fig.11 plotting S^{conf} vs γ.

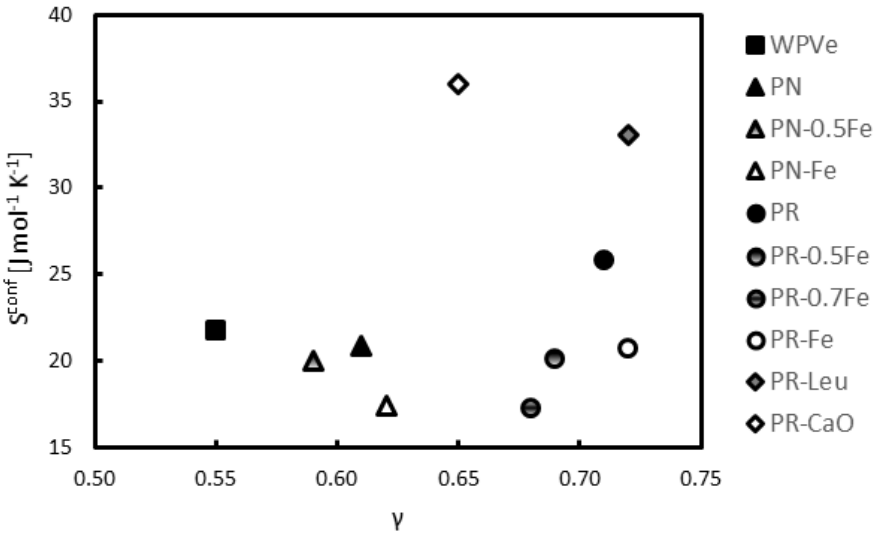

Fig. 11 S^{conf} fitted with Eq. 5 vs γ

The ratio B_e/S^{conf} is an indicator for the value of the changes of the average potential energy barrier to viscous flow (Richet 1984; Toplis 1998; Webb 2005) or the size of the smallest moving structural unit in the melt (Toplis 1998). This ratio is plotted against γ of the melts and shown in Fig. 12.

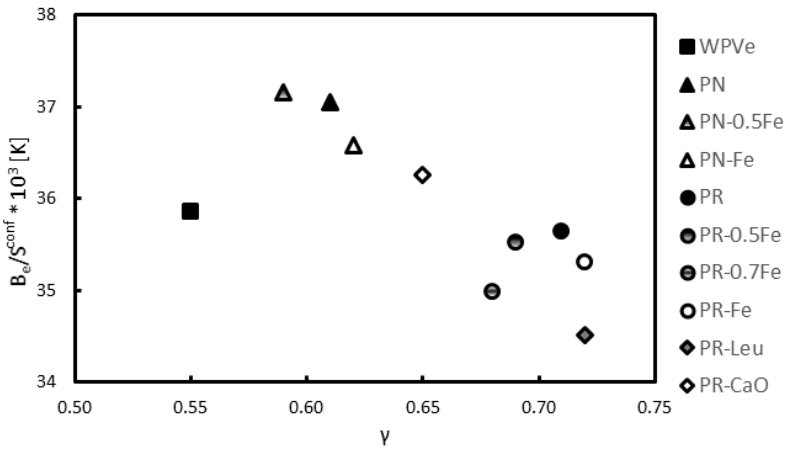

Fig. 12 $B_e/S^{conf}*10^3$ vs γ

It is highest for the PN compositions (37.15 – 36.58 $\times 10^3$ K), followed by PR-CaO (36.25 $\times 10^3$ K), WPVe (35.86 $\times 10^3$ K) and the PR series (35.64 – 34.99 $\times 10^3$ K) and the lowest B_e/S^{conf} ratio occurs for PR-Leu (34.52 $\times 10^3$ K). This trend indicates that the size of the smallest structural unit in the melt decreases with decreasing polymerisation as the bridging oxygens are replaced by an increasing number of non-bridging oxygens.

Comparison with existing viscosity models

Several models exist for the prediction of the viscosity of silicate melts. Bottinga and Weill (1972) developed a model applying to many low viscosity extrusive anhydrous melts that was improved by Shaw (1972) to extend it to hydrous compositions. Giordano and Dingwell (2003) developed the first model considering the non-Arrhenian behaviour of silicate melts over a wide temperature range restricted to anhydrous melts. A model for anhydrous and hydrous silicate melts was given by Hui and Zhang (2007) expanding the temperature range for modelled viscosities. A further model was developed by Giordano et al. (2008) that encompasses most compositions of naturally occurring volcanic rocks and includes H_2O and F as volatile components. However, this model does not differentiate between the iron species which affect the melt structure – and viscosity – in different ways. A model considering the iron speciation in common, iron-bearing melts was developed by Duan (2014) with a root-mean-square-error of 0.23 log units. Sehlke and Whittington (2016) developed a specific model for the anhydrous tholeiitic basalts taking into account the different iron species.

A comparison between measured and predicted viscosities in the range from $10^{8.3}$ to $10^{13.5}$ Pa s, at temperatures from ~640 to ~840 °C, is done with the model from Hui and Zhang (2007) and shown in Fig. 13. This model underestimates the viscosities of the investigated melts with the highest iron content by approx. two and a half orders of magnitude (PR, PR-CaO, and PN and PR-Leu with FeO_{tot} of 9.46 wt%, 10.25 wt%, 7.28 wt% and 11.13 wt%, respectively, ordered with decreasing deviation). The lower the iron content the smaller the deviation. Whilst the viscosities of PN-0.5Fe and PR-0.5Fe are underestimated more than two orders in magnitude with decreasing deviations with increasing temperature, PR-0.7Fe is underestimated of approx. one order of magnitude at lower temperatures. When temperature rises the predicted viscosities for the PR-0.7Fe composition reach the measured viscosities. The predicted viscosity of the WPVe composition having the lowest iron content of all iron-bearing compositions (2.72 wt%) in this study is one $\log_{10}$ Pa s lower than that measured at ~680 °C. At temperatures of ~720 °C and above, the measured viscosities of this melt are predicted quite well. The viscosities of the iron-free compositions PN-Fe and PR-Fe are within the error of this

model (2σ = 0.61 $\log_{10}$ Pa s) over the whole temperature range. This observation could be founded on the fact that the model from Hui and Zhang (2007) does not consider the iron speciation since it treats all iron as FeO. This is a very important criterion as ferrous and ferric iron have different effects on melt viscosity. Whereas ferrous iron is considered to act as a network modifier reducing the viscosity, ferric iron is assumed to behave like a network former and thus increases viscosity (i.e. Kress and Carmichael 1991; Wilke 2005; Knipping et al. 2015). Hence, the viscosity increasing influence of the ferric iron is completely disregarded by this model. Consequently, the higher the iron content of the studied melt (treated as FeO), the higher the total amount of ferric iron, the higher the network forming effect and the greater the underestimation of the prediction in viscosity as it is seen in Fig. 13. A second reason could be the dataset supporting this model includes a few phonolitic and tephritic compositions but no foiditic compositions.

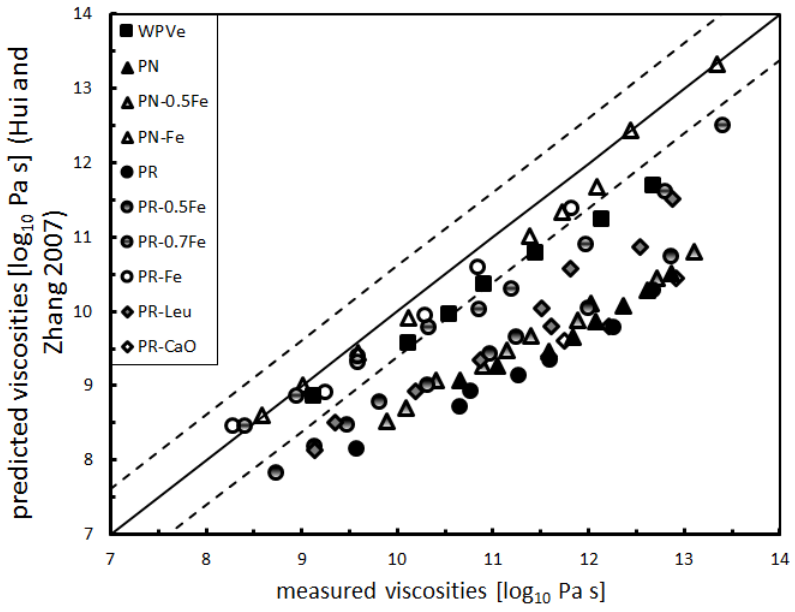

Fig. 13 Comparison of the measured viscosities in this study with those predicted by the model from Hui and Zhang (2007). Exact agreement is marked by the continuous line and upper and lower errors are marked by the dotted lines

The rheological data of this study are additionally compared with the model from Giordano et al. (2008) (subsequently denominated as GRD08) in Fig. 14. In the viscosity range from $10^{8.3}$ to $10^{13.3}$ log Pa s, corresponding to temperatures of ~680 °C to ~840 °C, the Fe-free melt compositions PN-Fe and PR-Fe and the WPVe melt composition (FeO_{tot} <3 wt%) are predicted well by GRD08. The largest deviation is 0.32 log Pa s, which is within its estimated error of 5%. In general, GRD08 underestimates the viscosities of most of the melts in this study, with

the viscosity of the melt with the highest FeO_{tot} (>11 wt% for PR-Leu) underestimated by ~ 1.25 log_{10} Pa s. The viscosities for the PR-0.7Fe composition (FeO_{tot} = 5.10 wt%) are overestimated by up to one order in magnitude. In contrast, the viscosities for the PN-0.5Fe composition with a similar FeO_{tot} content (5.82 wt%) are strongly underestimated by this model with deviations of ~1.20 log_{10} Pa s. The predicted viscosities of all other melt compositions are strongly underestimated. In particular, the prediction of viscosities of PR-CaO (FeO_{tot} >10 wt%) is nearly 2 orders of magnitude lower than the measured ones. It is notable that the deviations of the predicted from the measured viscosities get smaller with decreasing iron content. One explanation could be that the GRD08 model does not take into account the iron speciation. The GRD08 model lists all iron as FeO_{tot} assuming the same Fe^{2+}/Fe^{3+} ratio for all silicate melts, probably resulting in the underestimation of the viscosity of melts with more Fe^{3+} than that assumed in the general range of melt compositions used for fitting the model parameters. The model underestimates the viscosity of PR-0.5Fe with Fe^{2+}/Fe_{tot} of 0.36 but overestimates the viscosity of PR-0.7Fe with nearly the same Fe^{2+}/Fe_{tot} of 0.37. So it can not be simply the Fe^{2+}/Fe^{3+} ratio which results in an underestimation of the measured viscosities. A further possibility for the misfits of the GRD08 model could be that it is not calibrated for phonolitic or foiditic compositions investigated in this study.

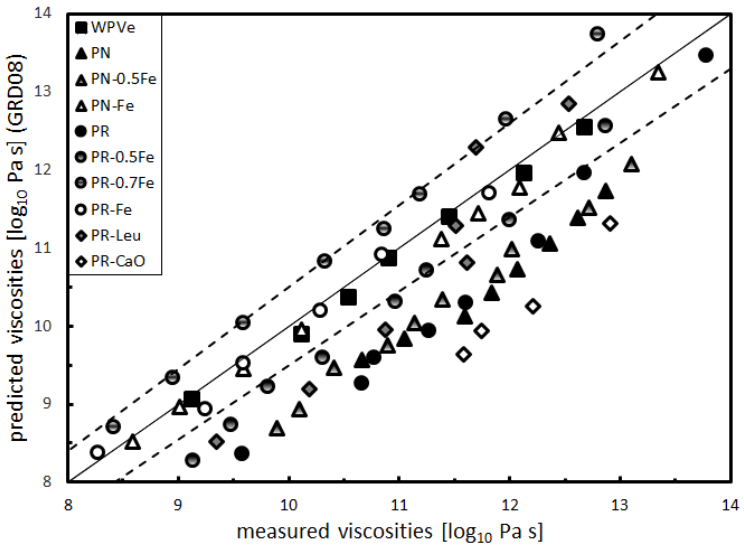

Fig. 14 Comparison of measured viscosities in this study with the predicted ones from Giordano et al. (2008). The continuous line represents exact agreement and dotted lines mark the upper and lower errors of the prediction given by GRD08

Fig. 15 shows a third comparison of the viscosities of the studied melt compositions with the model from Duan (2014) in the viscosity range from 10^9 Pa s to 10^{14} Pa s. The viscosity of most

of the investigated melts (PR-Leu, PN-Fe, PR-0.7Fe, PR-0.5Fe and PR-Fe) are overestimated by this model up to 1.61 $\log_{10}$ Pa s for PR-Leu at ~660 °C. The viscosity of the WPVe composition is overestimated more than one order of magnitude at 680 °C by this model. This overestimation decreases with increasing temperature to 0.23 $\log_{10}$ Pa s at 820 °C. The predicted viscosities of the PR composition are overestimated with deviations of 0.63 $\log_{10}$ Pa s at 670 °C and 0.23 $\log_{10}$ Pa s at 740 °C. The viscosity of the PR-CaO melt is quite well predicted within the given error of 0.23 $\log_{10}$ Pa s. The viscosity of the PN and PN-0.5Fe compositions are underestimated over the whole viscosity range up to 0.73 $\log_{10}$ Pa s and nearly one order in magnitude, respectively. The viscosity of the iron-rich and foiditic composition of the PR-CaO melt is the best prediction in this comparison although foiditic melt compositions are not included in the database for the model from Duan. Within the PN series it is seen that the predictions get worse with decreasing iron content. It is the same for PR, PR-0.5Fe and PR-0.7Fe. The model calibration is based on compositions showing a decreased iron content with increasing SiO_2 content not including all of the iron-silica-range of the melts in this study. Additionally, the model should not be used for iron-free compositions (Duan 2014). This point could be an explanation for the predicted viscosities within the PN series and PR, PR-0.5Fe and PR-0.7Fe getting worse with decreasing iron content but unchanged silica content.

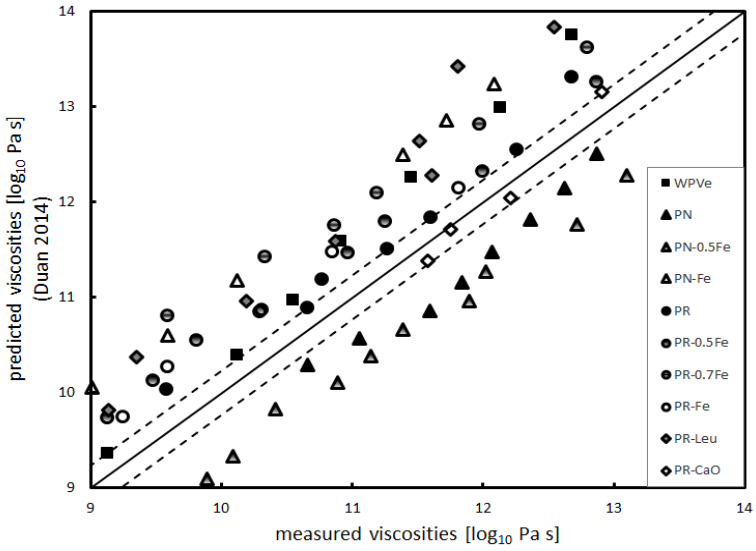

Fig. 15 Comparison of measured viscosities with predicted viscosities from the model from Duan (2014). The continuous line marks exact agreement and dotted lines mark the upper and lower error of the viscosity prediction

Commonly, higher viscosities than expected would occur in melts which contain crystals. X-ray diffraction of these glasses together with measurements of viscosity at alternating high and low temperature show that the melts are crystal-free. However, the Raman spectra after

measurements show an increase in the nanolite content and a reduced "hump" typical for glass indicating a growth of nanolites (Fig. 4). Supposing a crystallisation of 2 vol% nano-magnetites, modelling the relative viscosity after Klein et al. (2018) considering the degree of crystallinity and the shape of crystals shows a viscosity increase of 0.03 $\log_{10}$ Pa s. This influence is negligible since this change in viscosity is within the error of measurements. Nonetheless, the residual liquid melt changes its composition during crystallisation and consequently its structure and rheological behaviour. The viscosity of the PN and PR composition in comparison with those after crystallisation of 2 vol% magnetite (PN-2vol% magnetite and PR-2vol% magnetite, respectively) is modelled using the GRD08 model. Due to the increased content of the network forming SiO_2, the depletion of Fe_3O_4 in the PN and PR melt increases the viscosity of the pure liquid melt by approx. 0.5 $\log_{10}$ Pa s and nearly 0.4 $\log_{10}$ Pa s, respectively, as demonstrated in Fig. 16.

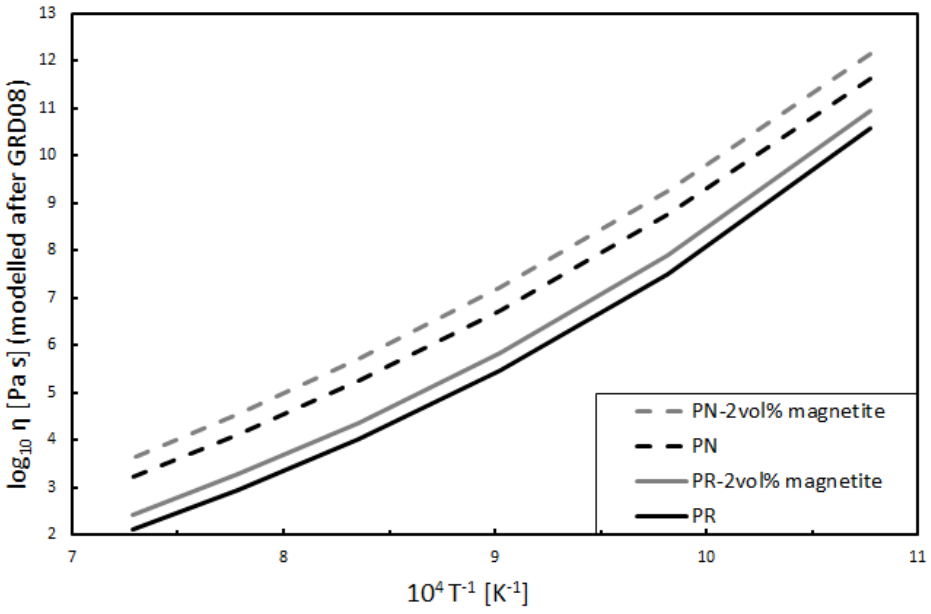

Fig. 16 Modelled liquid viscosities of the PN and PR composition and the PN and PR composition after the removal of 2 vol% magnetite after GRD08

Consequently, the measured viscosities of the PN and PR melt differ from the actual viscosities since amounts of 1 to 2 vol% nano-magnetite are present in the melt. The viscosity increase due to crystallisation reduces the discrepancies between measured and predicted viscosities by the models of PN and PR melt. However, the viscosities are still underestimated by the model from Hui and Zhang (2007) and the GRD08 model. The predicted viscosity of the pure liquid PN composition after Duan (2014) converges to the predicted one whereas the predicted viscosity of the pure liquid PR compositions departs significantly from the predicted one. Furthermore,

the modelled decrease in viscosity of the liquid PN melt of approx. 0.5 $\log_{10}$ Pa s due to crystallisation of nanolites reduces the differences between the presented data and that of Campagnola et al. (2016).

Geology of the PN and PR eruptions

As mentioned above, the melt viscosity of the PR melt is lower than that of the PN melt (Fig. 5). Both melts have higher viscosities than expected based simply on the SiO_2 and K_2O contents (Fig. 2). The present data illustrate that the assimilation of the carbonate wall rock leads to a decrease in viscosity of the PR melt since the viscosities of PR-CaO are higher than those of the PR whole rock composition. This is not considering the effect of CO_2 – that additionally enters the melt – on the melt viscosity during carbonate wall rock assimilation. Furthermore, the crystallisation of 4 mol% leucite from the PR whole rock composition leads to a decrease in viscosity of the residual melt PR-Leu. Depending on the crystal content, their shape, the connectivity between crystals in the melt, the resultant viscosity of a mixture of melt and crystals is higher than that of a crystal-free liquid and thus affecting the eruptive style (i.e. Stevenson et al. 1996; Caricchi et al. 2007; Vona et al. 2011). Caricchi et al. (2007) investigated the rheology of crystal-bearing magmas with a crystal fraction up to 0.80. Vona et al. (2011) studied the rheology of basaltic magmas with a crystal fraction up to approx. 0.30. Both studies present a model for calculating the apparent viscosity as a function of the applied shear rate. Following Kolzenburg et al. (2018), geological relevant shear rates range from approx. 70 s^{-1} to 10^{-9} s^{-1}. Calculations of the relative viscosities depending on shear rate after Caricchi et al. (2007) and Vona et al. (2011) are presented in Fig. 17 with shear rates of 70 s^{-1}, 0.1 s^{-1} and 10^{-9} s^{-1} as a function of different leucite contents. 4 mol% leucite from the whole rock composition of PR correspond to ~14 vol% crystals in the melt. The volume of the melt was estimated after Lange & Carmichael (1987). As shown in Fig. 17, depending on the applied shear rate, the viscosity of the crystal bearing melt increases by 0.04 to 0.06 $\log_{10}$ Pa s after Vona et al. (2011), which is negligible since it is within the error of the measurements but increases up to 0.22 $\log_{10}$ Pa s after Caricchi et al. (2007). Freda et al. (2011) found some pyroclastic units from the PR event to be highly porphyric with leucite phenocrysts up to 40 – 60 vol%. Therefore, the relative viscosity of two further leucite contents are calculated for an approximation of the changes in viscosities: one with 28 vol% and another one with 56 vol% leucite crystals. The calculation after Vona et al. (2011) for a leucite fraction of 0.28 increases the viscosity by 0.13 $\log_{10}$ Pa s in comparison to the model from Caricchi et al. (2007) that results in an increase of nearly 0.60 $\log_{10}$ Pa s. Both models demonstrate higher relative viscosities with decreasing shear rates but

show significant differences in predicting the relative viscosity with respect to each other. A leucite content of 56 vol% in the melt leads to a significant increase in viscosity up to nearly two orders in magnitude at a shear rate of 10^{-9} s^{-1}. However, these models do not consider the effect of magma evolution during crystallisation resulting in a depletion of K_2O-Al_2O_3-SiO_2 from the melt composition. As shown in Fig. 5, the viscosity of the residual melt PR-Leu after 4 mol% leucite crystallisation decreases by nearly one order in magnitude. Assuming this behaviour continues during progressive crystallisation, the residual melt would become less viscous and the relative viscosity would not be as high as predicted by the models from Caricchi et al. (2007) and Vona et al. (2011).

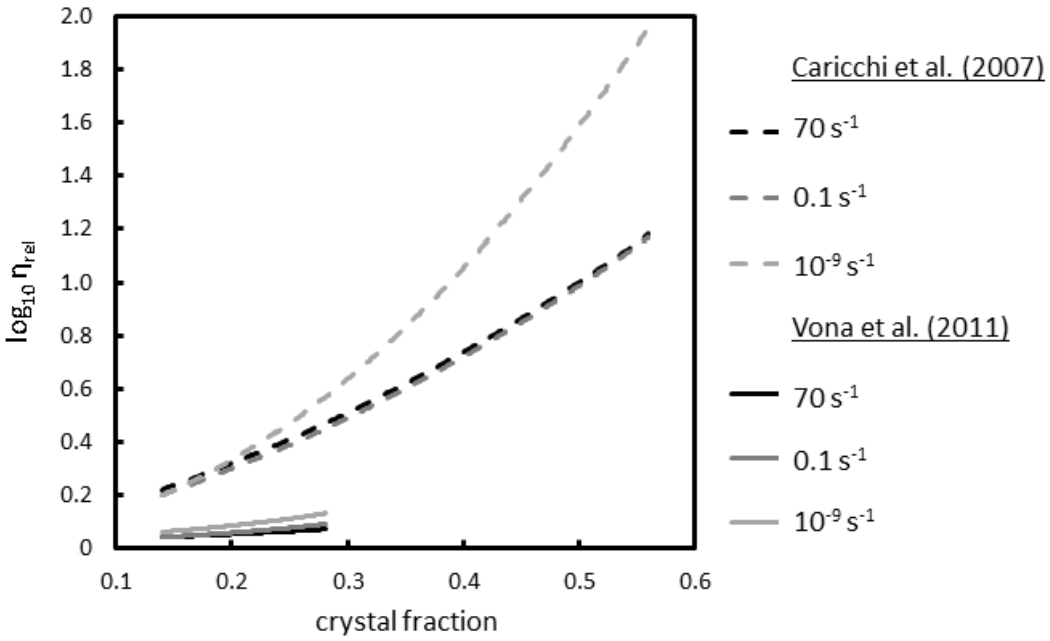

Fig. 17 Relative viscosity η_{rel} vs leucite fraction. Two leucite fractions (0.14 and 0.28) are calculated after Caricchi et al. (2007) and Vona et al. (2011) and a third leucite fraction of 0.56 is calculated after Caricchi et al. (2007). Relative viscosities are calculated with three different shear rates (70 s^{-1}, 0.1 s^{-1} and 10^{-9} s^{-1}) relevant for volcanic implications

Freda et al. (2011) discussed the PR event by plotting DRE vs. SiO_2 (Fig. 1) and observed that this low silica melt plots outside the cloud of data for large eruptions as a function of SiO_2 content. However, as shown in Fig. 18 this comparison is between Na_2O-K_2O-rich and CaO-MgO-FeO-rich melts.

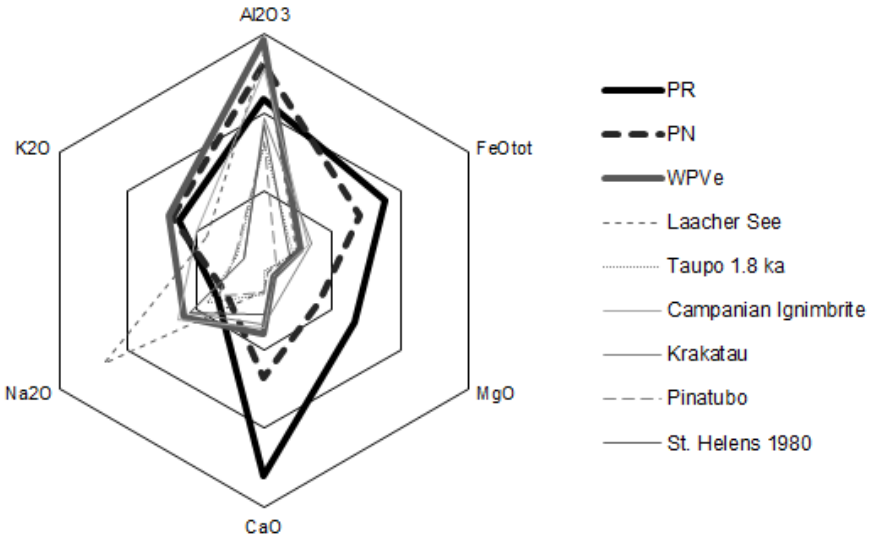

Fig. 18 Net diagram for the investigated PR, PN and WPVe compositions and other large-volume eruptions worldwide. Compositions are in mol% ranging from 0 mol% up to 15 mol% at the outermost line. The compositions analysed in this study are rich in potassium and the PR and PN compositions have much higher contents in FeO_{tot}, MgO and especially CaO in comparison with the other melts. The Laacher See composition is enriched in Na_2O. For detailed information of the compositions see Table 1 (for PR, PN and WPVe) or Takeuchi (2011) and references therein (for the other eruptions)

As illustrated by the study of Webb et al. (2007), the viscosity of CaO-Al_2O_3-SiO_2 melts is 4 orders of magnitude greater than that of Na_2O-Al_2O_3-SiO_2 melts at 800 °C for $\gamma > 0.5$, with this difference decreasing with increasing temperature. Hess et al. (1995, 1996) also illustrate that the addition of 5 mol% CaO to a haplo-granitic composition melt results in a viscosity an order of magnitude higher than the composition with 5 mol% added Na_2O. Increasing these additions to 10 mol% produces a 2 order of magnitude difference between the Na_2O and CaO enriched melt viscosities. In contrast, the plot shown in Fig. 1 assumes the viscosities of the alkaline-earth rich PN and PR melts are similar to the low viscosity alkali-rich melts of the other eruptions in the graph. Fig. 19 plots (CaO + MgO)/(Na_2O + K_2O) vs SiO_2 content of several large-volume eruptions (see also Fig. 1). The PR composition appears to be an exception in this graph since it is the only melt with an alkaline-earth/alkali ratio higher than 1. However, it follows an obvious trend of a decreasing (CaO + MgO)/(Na_2O + K_2O) value with increasing SiO_2 content for all these events. Assuming that this correlation is valid for more complex compositions, it illustrates that the viscosities of PR and PN compositions are higher than expected since their enrichment in alkaline-earth is conventionally not considered in discussions of the viscosities of these melts. Thus, only regarding the SiO_2 content of a melt is insufficient for an estimation of its viscosity and rheological behaviour.

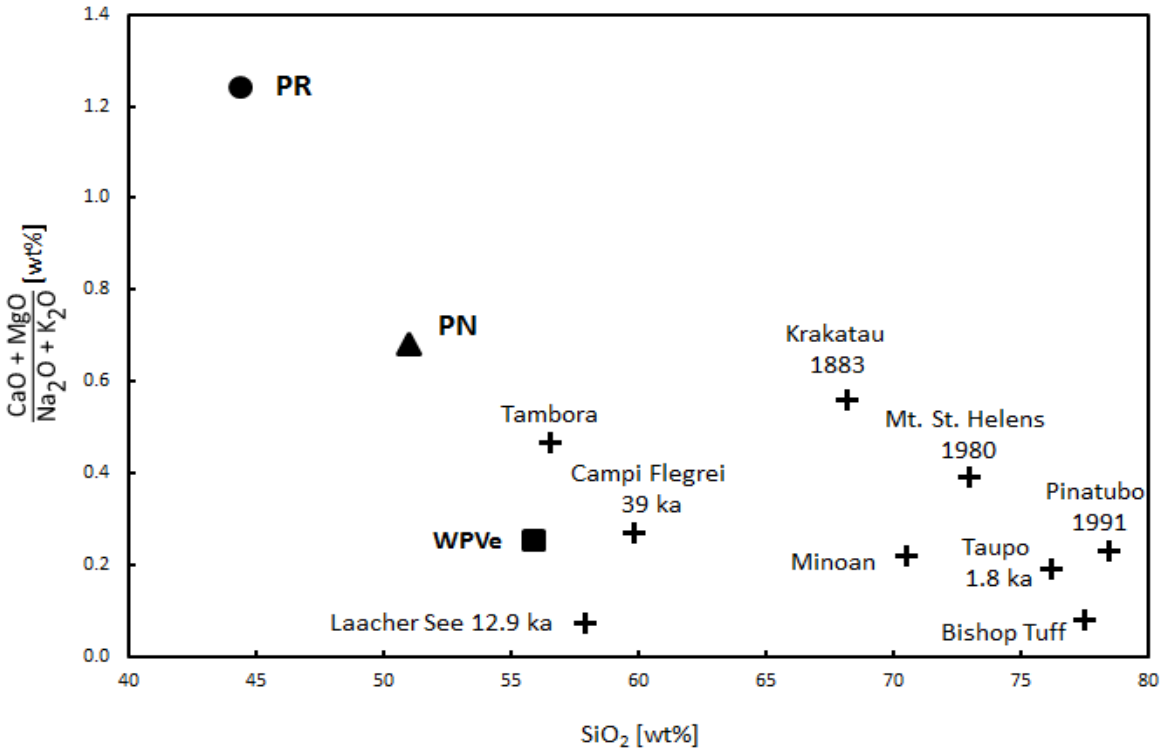

Fig. 19 Comparison of high-volume eruptions in the plot (CaO + MgO)/(Na_2O + K_2O) vs SiO_2

Trolese et al. (2017) investigated the emplacement temperatures of magmatic ignimbrites of the CAVD including the PN and PR eruptions. They found the emplacement temperature to be between 600°C or 630°C and 710°C for PN and PR, respectively, and suggest that process of magma fragmentation begins at temperatures approx. 100 °C higher than the emplacement one. Takeuchi (2011) estimated pre-erupted temperatures for the other eruptions in Table 5 and Figs. 18 and 20. With the presumption that melt fragmentation is a syn-eruptive process the eruptive temperatures for all compared melts range between 700 and 1070 °C. In this temperature range the viscosity curves of the PR and PN compositions cross the viscosity curves of the other Na_2O-Al_2O_3-SiO_2 melts (Fig. 20) due to their different fragilities of ~31 and 24-28, respectively.

In January 2002, foiditic lava was ejected by the Mt. Nyiragongo (Santo et al. 2002; Giordano et al. 2007). The lava near the top of the volcano was highly fluid and moved quickly forward whereas the lava at the bottom of Mt. Nyiragongo was more viscous moving with less speed. Giordano et al. (2007) measured the dry liquid viscosity of remelted lava from this eruption to be approx. two $\log_{10}$ Pa s lower than that from the foiditic synthetic glasses from this study. They conclude different eruptive temperatures at the different locations: the lava escaped in higher altitudes erupted at higher temperatures than the lava at the base of the volcano resulting in a lower viscous flow near the volcanic top. The eruptive temperatures for the Mt. Nyiragongo

event are much higher than those for the PR event what results in higher eruptive viscosity for PR.

explosive event	composition	references	fragility
PR	foidite	Freda et al., 2011	31.13[a]
PN	tephri-phonolite	Campagnola et al,. 2016	30.96[a]
WPVe	phonolite	Balcone-Boissard et al., 2011 Iacono-Marziano et al., 2007	26.47[a]
Laacher See	phonolite	Harms & Schmincke, 1999	26.02[b]
Taupo 1.8 ka	rhyolitic	Dunbar et al., 1989	24.58[b]
Campanian Ignimbrite	trachytic	Marianelli et al., 2006	28.21[b]
Krakatau	mainly rhyodacitic	Mandeville et al., 1996	27.84[b]
Pinatubo 1991	dacitic	Westrich & Gerlach, 1992	24.32[b]
Usu 1663	rhyolitic	Tomiya et al, 2010	25.31[b]
Aniakchak 3430 BP	andesitic	Larsen, 2006	34.95[b]
St. Helens 1980	rhyolitic	Takeuchi, 2011	25.89[b]

[a] fragility calculated after Eq. 4

[b] fragility calculated after GRD08 (Giordano et al. 2008)

Table 5 Chemical classification and fragilities from large-volume eruptions from all over the world

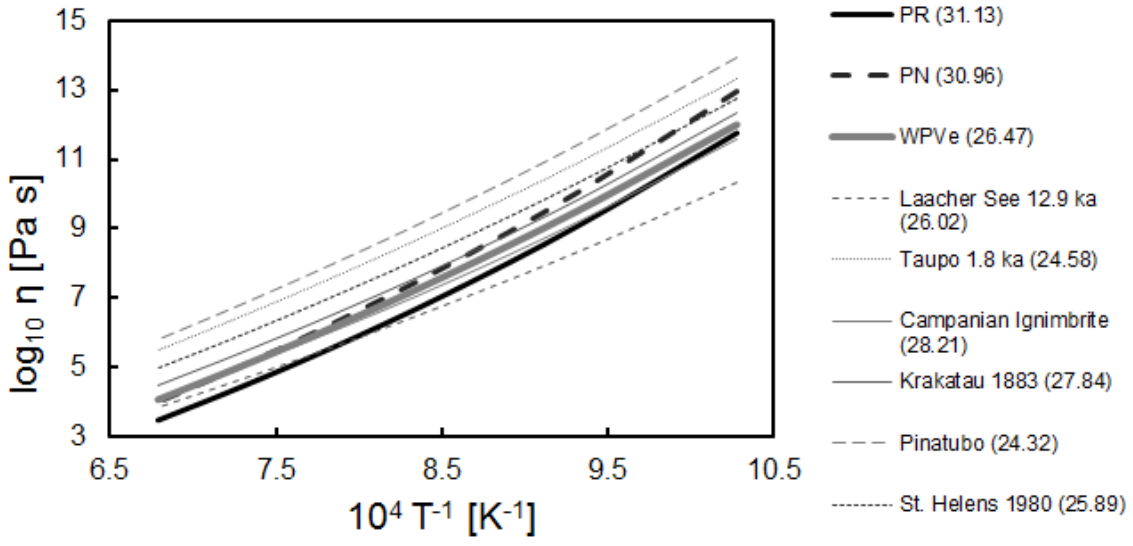

Fig. 20 Viscosities of the PR, PN and WPVe compositions investigated in this study with measured and extrapolated viscosities using Eq. 5 and further large-volume eruptions worldwide. Compositions for these events are taken from Takeuchi and references therein (2011), viscosities are calculated with the GRD08 model. Fragilities are written in parentheses

Consequently, as an approximation of the rheology of an erupting magma controlls the explosivity of an eruptive event, the viscosity at the eruptive temperature ($\eta(T_{erupt})$) should be regarded rather than the SiO_2 content only. In Fig. 21, the viscosity at the temperature at eruption is plotted vs the silica content for some of the major explosive eruptions with a high DRE. The viscosities at eruptive temperature from the melts from literature are calculated with the GRD08 model ignoring any content of H_2O. The PR, PN and WPVe compositions measured in this study have eruptive viscosities of 8.58, 9.56 and 9.18 log_{10} Pa s, respectively.

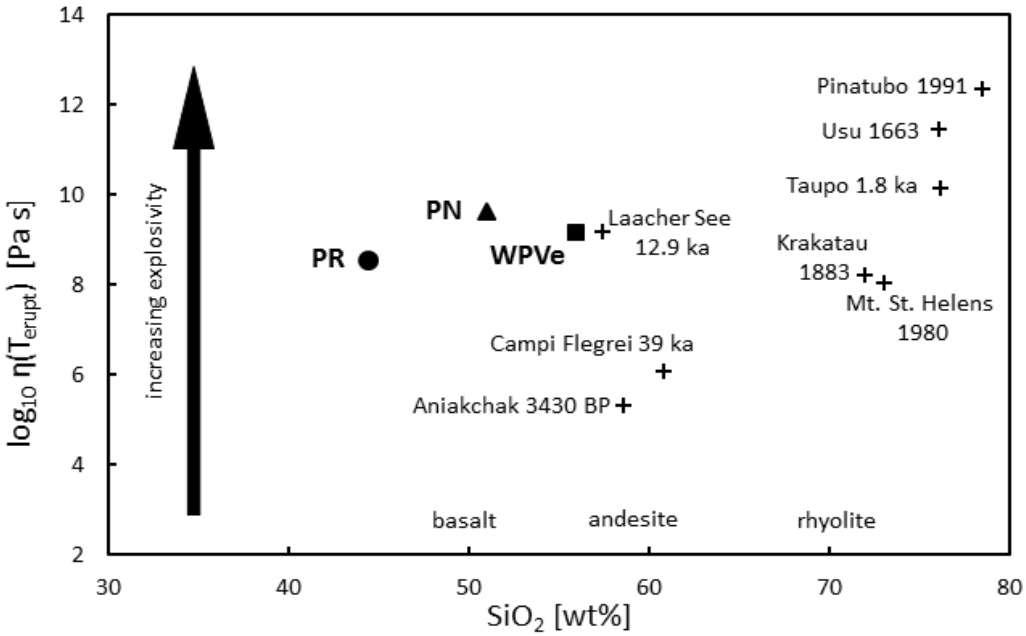

Fig. 21 Viscosity at eruptive temperature as a function of SiO_2 content for some large-volume eruptions showing that the eruptive viscosities for PR, PN and WPVe are in the middle of all these explosive events

It is seen that their eruptive viscosities are in the middle of all events in spite of their low SiO_2 content. The explosivity of an eruption increases with increasing eruptive viscosity. By means of this plot it can be estimated that at eruptive viscosities of 5-6 log_{10} Pa s the eruptive style changes from effusive to explosive considering a dry and crystal- and bubble-free magma. The relationship between the DRE of all these explosive events and the eruptive temperature is shown in Fig. 22, indicating that these eruptions fall together in the same area in this figure and that the PR and PN events are also in the middle of all data points. Considering the melt viscosity at the eruption of an event, the PR and PN eruptions are not as unusual as they appear when plotted in the DRE vs SiO_2 diagram (Fig. 1).

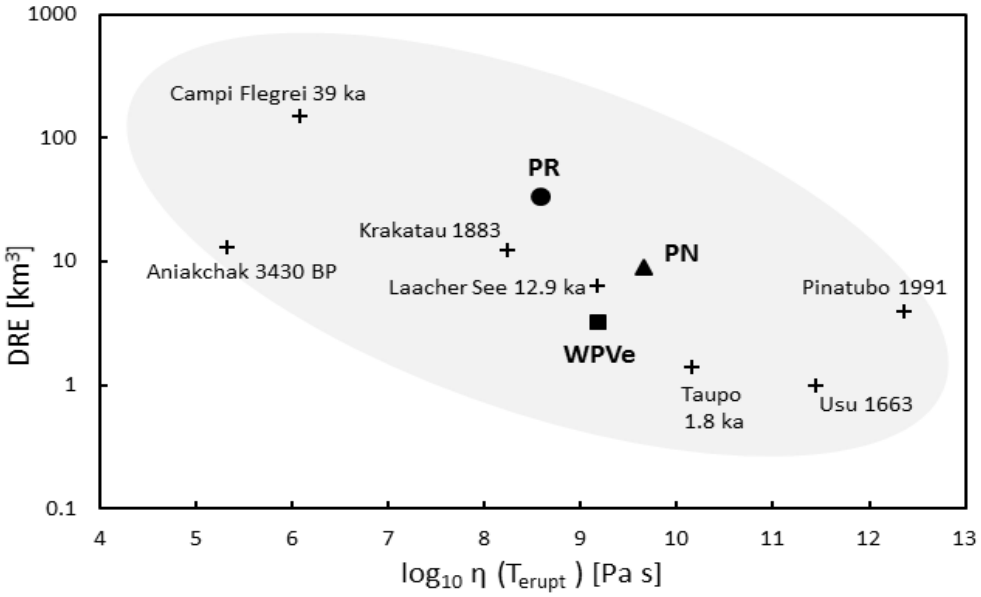

Fig. 22 DRE from explosive eruptions as a function of the viscosity at eruptive temperature. PR, PN and WPVe form a cloud with the other eruptions showing no anomalous position

However, natural magmas and lavas are a mixture of a liquid melt, solid particles and gas bubbles (Lev et al. 2019). This, together with the species of volatiles, strain and shear-rates generated by the geological setting of a volcano, results in a complex melt rheology (i.e. Dingwell et al. 1996; Giordano et al. 2008; Robert et al. 2013; Sehlke and Whittington 2016) not investigated in this study. Especially for the geological conditions of the CAVD, the formation of a CO_2-rich fluid and an enrichment of the CaO component in the melt even in syn-eruptive processes are important features affecting the style of its eruptions.

Nevertheless, the plot in Fig. 19 constitutes a good first approximation of the explosivity of an eruption including the alkaline-earth content as well as the SiO_2 content.

Conclusion

Considering the SiO_2 content only or together with the alkali content is a common way to estimate the viscosity of a melt. This study illustrates that this is not sufficient. The viscosities presented here are higher than expected using conventional approximations as these compositions are not only silica undersaturated and rich in K but also rich in alkaline-earths. The knowledge of the rheological features of a melt and especially the viscosity is fundamental for understanding and evaluating the style in which a volcano erupts. Hence, it is proposed here to estimate the explosivity of an eruption not only based on the silica content of a melt but additionally on the ratio $(CaO + MgO)/(Na_2O + K_2O)$.

Acknowledgements

This research was funded by the Deutsche Forschungsgemeinschaft grant No. WE 1801/15-1. For technical assistance, we wish to thank Bettina Schlieper-Ludewig for her help at the viscosity and calorimetry measurements and the colorimetric determination of the iron speciation and Marina Horstmann for her help at the chemical analysis at the µ-RFA and the EMP as well as Andre Petitjean for the sample preparation. Furthermore, we wish to thank Dr. Andreas Kronz for the support at the electron microprobe, Dr. Kirsten Techmer for the support at the scanning electron microscope and Dr. Burkhard Schmidt for the discussion of the Raman spectra. We thank the two anonymous reviewers for their constructive suggestions for improvements.

References

Adam G and Gibbs JH (1965) On the Temperature Dependence of Coorperative Relaxation Properties in Glass-Forming Liquids. J Chem Phys 43:139-146

Anderson Jr. AT, Newman S, Williams SN, Druitt TH, Skirius C, Stolper E (1989) H_2O, CO_2, Cl and gas in Plinian and ash-flow Bishop rhyolite. Geology 17:221-225

Angell C A, Yue Y, Wang L-M, Colpey J R D, Borick S, Mosa S (2003) Potential energy, relaxation, vibrational dynamics and boson peak, of hyperquenched glasses. J Phys: Condensed Matter 15:1051-1068

Balcone-Boissard H, Boudon G, Villemant B (2011) Textural and geochemical constraints on eruptive style of the 79 AD eruption at Vesuvius. Bull Volcanol 73:279-294

Blythe LS, Deegan FM, Freda C, Jolis EM, Masotta M, Misiti V, Taddeucci J, Troll VR (2015) CO_2 bubble generation and migration during magma-carbonate interaction. Contrib Mineral Petrol 169:article 42

Boari E, Avanzinelli R, Melluso L, Giordano G, Mattei M, De Benedetti AA, Morra V, Conticelli S (2009) Isotope geochemistry (Sr-Nd-Pb) and petrogenesis of leucite-bearing volcanic rocks from “Colli Albani” volcano, Roman Magmatic Province, Central Italy: inferences on volcano evolution and magma genesis. Bull Volcanol 71:977-1005

Bottinga Y and Weill DF (1972) The viscosity of magmatic silicate liquids: a model for calculation. Am J Sci 272:438-475

Campagnola S, Vona A, Giordano G (2016) Crystallization kinetics and rheology of leucite-bearing tephriphonolite magmas from the Colli Albani volcano (Italy). Chem Geol 424:12-29

Caricchi L, Burlini L, Ulmer P, Gerya T, Vassalli M, Papale P (2007) Non-Newtonian rheology of crystal-bearing magmas and implications for magma ascent dynamics. Earth Planet Sci Lett 264:402-419

Chiarabba C, Amato A, Delaney PT (1997) Crustal structure, evolution, and volcanic unrest of the Alban Hills, Central Italy. Bull Volcanol 59:161-170

Di Genova D, Sicola S, Romano C, Vona A, Fanara S, Spina L (2017) Effect of iron and naolites on Raman spectra of volcanc glasses: A reassessment of existing strategies to estimate the water content. Chem Geol 475:76-86

Dingwell DB, Knoche R, Webb SL (1992) The effect of B_2O_3 on the viscosity of haplogranitic liquids. Am Mineral 77:457-461

Dingwell DB, Romano C, Hess K-U (1996) The effect of water on the viscosity of a haplogranitic melt under P-T-X conditions relevant to silicic volcanism. Contrib Mineral Petrol 124:19-28

Dingwell DB and Webb SL (1989) Structural Relaxation in Silicate Melts and Non-Newtonian Melt Rheology in Geological Processes. Phys Chem Minerals 16:508-516

Di Rocco T, Freda C, Gatea M, Mollo S, Dallai L (2012) Magma Chambers Emplaced in Carbonate Substrate: Petrogenesis of Skarn and Cumulate Rocks and Implications for CO_2 Degassing in Volcanic Areas. J Petrology 53:2307-2332

Duan X (2014) A model for calculating the viscosity of natural iron-bearing silicate melts over a wide range of temperatures, pressures, oxygen fugacites and compositions. Am Mineral 99:2378-2388

Dunbar NW, Hervig RL, Kyle PR (1989) Determination of pre-eruptive H_2O, F ans Cl contents of silicic magmas using melt inclusions: examples from Taupo volcanic center, New Zealand. Bull Volcanol 51:177-184

Einstein A (1906) Eine neue Bestimmung der Moleküldimensionen. Annals Phys 19:289-306

Freda C, Gaeta M, Giaccio B, Marra F, Palladino DM, Scarlat P, Sottili G (2011) CO_2-driven large mafic explosive eruptions: the Pozzolane Rosse case study from the Colli Albani Volcanic District (Italy). Bull Volcanol 73:241-256

Freda C, Gaeta M, Misiti V, Mollo S, Dilfi D, Scarlato P (2008) Magma-carbonate interaction: An experimental study on ultrapotassic rocks from Alban Hills (Central Italy). Lithos 101:397-415

Gaeta M, Freda C, Marra F, Arienzo I, Gozzi F, Jicha B, Di Rocco T (2016) Paleozoic metasomatism at the origin of Mediterranean ultrapotassic magmas: Constraints from timedepentent geochemistry of Colli Albani volcanic products (Central Italy). Lithos 244:151-164

Giordano G, De Benedetti AA, Diana A, Diano G, Gaudioso F, Marasco F, Miceli M, Mollo S, Cas RAF, Funiciello R (2006) The Colli Albani mafic caldera (Roma, Italy): Stratigraphy, structure and petrology. J Volcanol Geotherm Res 155:49-80

Giordano D and Dingwell DB (2003) Non-Arrhenian multicomponent melt viscosity: a model. Earth Planet Sci Lett 208:337-349

Giordano D, Polacci M, Longo A, Papale P, Dingwell DB, Boschi E, Kasereka M (2007) Thermo-rheological magma control on the impact of highly fluid lava flows at Mt. Nyiragongo. Geophys Res Lett 34: L06301

Giordano D and Russell JK (2017) The heat capacity if hydrous multicomponent natural melts and glasses. Chem Geol 461:96-103

Giordano D, Russell JK, Dingwell DB (2008) Viscosity of magmatic liquids: A model. Earth Planet Sci Lett 271:123-134

Harms E, Schmincke H-U (1999) Volatile composition of the phonolitic Laacher See magma (12,900 yr BP): implications for syn-eruptive degassing of S, F, Cl and H_2O. Contrib Mineral Petrol 138:84-98

Hess K-U, Dingwell DB, Webb SL (1995) The influence of excess alkalis on the viscosity of a haplogranitic melt. Am Mineral 80:297-304

Hess K-U, Dingwell DB, Webb SL (1996) The influence of alkaline-earth oxides (BeO, MgO, CaO, SrO, BaO) on the viscosity of a haplogranitic melt: systematics of non-Arrhenian behaviour. Eur J Mineral 8:371-381

Hui H and Zhang Y (2007) Toward a general viscosity equation for natural anhydrous and hydrous silicate melts. Geochim et Cosmochim Acta 71:403-416

Iacono-Marziano G, Gaillard F, Pichavant M (2007a) Limestone assimilation and the origin of CO_2 emissions at the Alban Hills (Central Italy): constraints from experimental petrology. J Volcanol Geotherm Res 166:91-105

Iacono Marziano G, Schmidt BC, Dolfi D (2007b) Equilibrium and disequilibrium degassing of a phonolitic melt (Vesuvius AD 79 “white pumice”) simulated by decompression experiments. J Volcanol Geotherm Res 161:151-164

Karner DB, Marra F, Renne PR (2001) The history of the Monte Sabatini and Alban Hills volcanoes: groundwork for assessing volcanic-tectonic hazards for Rome. J Volcanol Geotherm Res 107:185-219

Klein J, Mueller SP, Helo C, Schweitzer S, Gurioli L, Castr JM (2018) An expanded model and application of the combined effect of crystal-size distribution and crystal shape on the reltive viscosity of magmas. J Volcanol Geotherm Res 357:128-133

Knipping JL, Behrens H, Wilke M, Göttlicher J, Stabile P (2015) Effect of oxygen fugacity on the coordination and oxidation state of iron in alkali bearing silicate melts. Chem Geol 411:143-154

Kolzenburg S, Di Genova D, Giordano D, Hess KU, Dingwell DB (2018) The effect of oxygen fugacity on the theological evolution of crystallizing basaltic melts. Earth Planet Sci Lett 487:21-32

Kress VC and Carmichael ISE (1991) The compressibility of silicate liquids containing Fe_2O_3 and the effect of composition, temperature, oxygen fugacity and pressure on their redox state. Contrib Mineral Petrol 108:82-92

Lange RA and Carmichael ISE (1987) Densities of Na_2O-K_2O-CaO-MgO-FeO-Fe_2O_3-Al_2O_3-TiO_2-SiO_2 liquids: New measurements and derived partial molar properties. Geochim et Cosmochim Acta 51:2931-2946

Larsen JF (2006) Rhyodacite magma storage cobditins prior to the 3430 yBP caldera-forming eruption of Aniakchak volcano, Alaska. Contrib Mineral Petrol 152:523-540

Lev E, Rumpf E, Dietterich H (2019) Analog experiments of lava flow emplacement. Annals GeoPhy 62:no 2

Maier CG, Kelley KK (1932) An equation for the representation of high-temperature heat content data. J Am Chem Soc 54:3243-3246

Mandeville CW, Carey S, Sigurdsson H (1996) Magma mixing, fractional crystallization and volatile degassing during the 1883 eruption of Krakatau volcano, Indonesia. J Volcanol Geotherm Res 74:243-274

Marianelli P, Sbrana A, Proto M (2006) Magma chamber of the Campi Flegrei supervolcano at the time of eruption of the Campanian Ignimbrite. Geolog Soc Am 34:937-940

Marra F, Karner DB, Freda C, Gaeta M, Renne P (2009) Large mafic eruptions on Alban Hills Volcanic District (Central Italy): Chronostratigraphy, petrography and eruptive behaviour. J Volcanol Geotherm Res 179:217-232

Martinez L-M & Angell CA, (2001) A thermodynamic connection to the fragility of glass-forming liquids. Nature 410:663-667

Marsh BD (1981) On the crystallinity, probably occurrence, and rheology of lava and magma. Contrib Mineral Petrol 78:85-98

Peccerillo A (2005) Plio-Quaternary volcanism in Italy Petrology, geochemistry, geodynamics. Springer Berlin Heidelberg, 365

Pocklington HC (1940) Rough measurement of high viscosities. Proc Cambridge Phil Soc 36:507-508

Richet P (1984) Viscosity and configurational entropy of silicate melts. Geochim et Cosmochim Acta 48:471-483

Richet P (1987) Heat capacity of silicate glasses. Chem Geol 62:111-124

Robert G, Smith RA, Whittington AG (2019) Viscosity of melts in the $NaAlSiO_4$-SiO_2 system: Configurational entropy modelling. J Non-Cryst Solids 524:119635

Robert G, Whittington AG, Stechern A, Behrens H (2013) The effect of water on the viscosity of synthetic calc-alkaline basaltic andesite. Chem Geol 346:135-148

Robie RA, Hemingway BS, Fischer JR (1978) Thermodynamic properties of minerals and related substances at 29815 K and 1 bar (10^5 Pa) pressure and at higher temperatures. US Geolog Surv Bull 1452:428-446

Roscoe R (1952) The viscosity of suspensions of rigid spheres. Br J Appl Phys 3:267-269

Russell JK and Giordano D (2017) Modelling configurational entropy of silicate melts. Chem Geol 461:140-151

Russell JK, Giordano D, Dingwell DB (2003) High-temperature limits on viscosity of non-Arrhenian silicate melts. Am Mineral 88:1390-1394

Santo AP, Capaccioni B, Tedesco D, Vaselli O (2002) Petrographic and geochemical features of the 2002 Nyiragongo lava flows. Acta Vulcanol 14:63-66

Sehlke A and Whittington AG (2016) The viscosity of planetary tholeiitic melts: A configurational entropy model. Geochim et Cosmochim Acta 191:277-299

Schuessler JA, Botcharnikov RE, Behrens H, Misiti V, Freda C (2008) Oxidation state of iron in hydrous phono-tephritic melts. Am Mineral 93:1493-1504

Shand SJ (1927) The Eruptive Rocks. Wiley, Mew York NY

Shaw HR (1972) Viscosities of magmatic silicate liquids, an empirical method of prediction. Am J Sci 272:870-893

Stevenson RJ, Dingwell DB, Webb SL, Sharp TG (1996) Viscosity of microlite-bearing rhyolitic obsidians: an experimental study. Bull Volcanol 58:298-309

Takeuchi S (2011) Preeruptive magma viscosity: An important measure of magma eruptibility. J Geophys Res 116:B10201

Tobolsky AV and Taylor RB (1963) Viscoelastic properties of a simple organic glass. J Phys Chem 67:2439-2442

Tomiya A, Takahashi E, Furukawa N, Suzuki T (2010) Depth and Evolution of a Silicic Magma Chamber: Melting Experiments on a Low-K Rhyolite from Usu Volcano, Japan. J Petrol 51:1333-1354

Toplis MJ (1998) Energy barriers to viscous flow and the prediction of the glass transition temperatures of molten silicates. Am Mineral 83:480-490

Toplis MJ, Dingwell DB, Hess K-U, Lenci T (1997) Viscosity, fragility and configurational entropy of melts along the join SiO_2-$NaAlSiO_4$. Am Mineral 82:979-990

Trolese M, Giordano G, Cifelli F, Winkler A, Mattei M (2017) Forced transport of thermal energy in magmatic and phreatomagmatic large volume ignimbrites: Paleomagnetic evidence from the Colli Albani volcano, Italy. Earth Planet Sci Lett 478:179-191

Vona A, Romano C, Dingwell DB, Giordano D (2011) The rheology of crystal-bearing basaltic magmas from Stromboli and Etna. Geochim et Cosmochim Acta 75:3214-3236

Webb SL (2005) Structure and rheology of iron-bearing Na_2O-Al_2O_3-SiO_2 melts. Eur J Mineral 17:223-232

Webb SL (2008) Configurational heat capacity of Na_2O-CaO-Al_2O_3-SiO_2 melts. Chem Geol 256:92-101

Webb SL (2011) Configurational heat capacity and viscosity of (Mg, Ca, Sr, Ba)-Al_2O_3-SiO_2 melts. Eur J Mineral 23:487-497

Webb SL (2014) Rheology and the Fe^{3+}-chlorine reaction in basaltic melts. Chem Geol 366:24-31

Webb SL, Banaszak M, Köhler U, Rausch S, Raschke G (2007) The viscosity of Na_2O-CaO-Al_2O_3-SiO_2 melts. Eur J Mineral 19:681-692

Webb SL, Müller E, Büttner H (2004) Anomalous rheology of peraluminous melts. Am Mineral 89:812-818

Westrich HR and Gerlach TM (1992) Magmatic gas source for the stratospheric SO_2 cloud from the June 15, eruption of Mount Pinatubo. Geology 20:867-870

Whittington A, Richet P, Holtz F (2000) Water and viscosity of depolymerized aluminosilicate melts. Geochim et Cosmochim Acta 64:3725-3736

Wilke M (2005) Fe in magma – An overview. Annals GeoPhys 48:609-617

Wilson AD (1960) The Micro-determination of Ferrous Iron in Silicate Minerals by a Volumetric and a Colorimetric Method. Analyst 85:823-827

3 Influence of CO_2 on the rheology of melts from the Colli Albani Volcanic District (Italy): foidite to phonolite

Preface

The following Chapter 3 has been made by Christin Kleest and Prof. Dr. Sharon Webb and their contribution to this study is seen in Fig. P1.

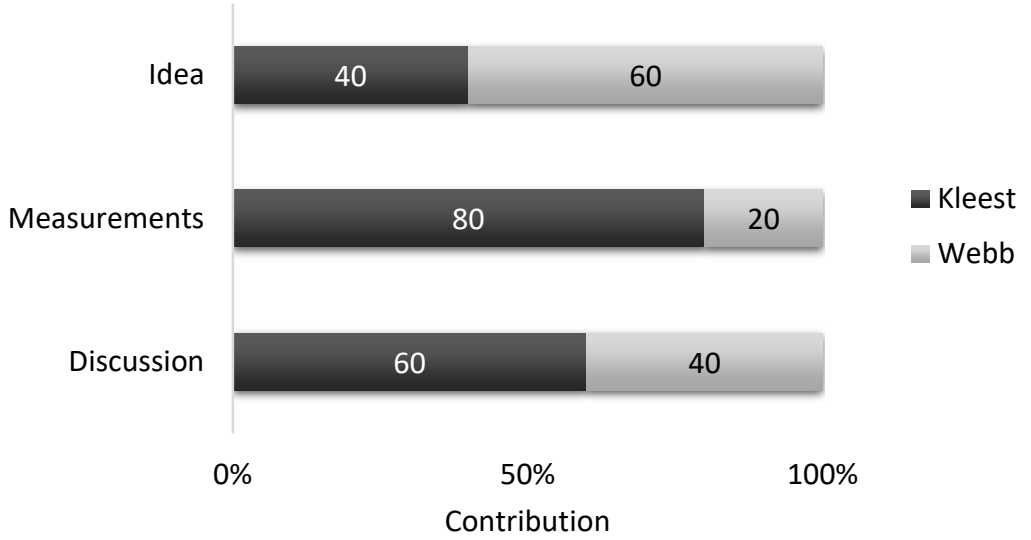

Fig. P1 Author contribution of the idea, measurements and discussion to this Chapter 3 from Christin Kleest and Prof. Dr. Sharon Webb.

This Chapter was submitted on 3 May 2021 to "Contributions to Mineralogy and Petrology", accepted on 10 September 2021 and finally published online on 15 October 2021. In the online version of this article supplementary material is provided consisting of 4 appendices A, B, C and D. In the presented version, these appendices are attached at the end of this 3rd Chapter. The abstract of this Chapter starts in the style of the published article whereas further contents are continued in the style of this thesis.

Contributions to Mineralogy and Petrology (2021) 176:92
https://doi.org/10.1007/s00410-021-01838-w

ORIGINAL PAPER

Influence of CO_2 on the rheology of melts from the Colli Albani Volcanic District (Italy): foidite to phonolite

Christin Kleest[1] · Sharon L. Webb[1]

Received: 3 May 2021 / Accepted: 10 September 2021

Abstract
In this study, the influence of CO_2 on the rheology of silica poor and K-rich melts from highly explosive eruptions from the Colli Albani Volcanic District (Italy) (CAVD) is measured for the first time. The investigated melts range from foidite to tephri-phonolite to tephrite from the CAVD to a phonolite from the Vesuvius (Italy) with CO_2 concentrations up to 0.50 wt%. Viscosity and calorimetric measurements are performed in the glass transition range T_g between 600 and 780 °C. Although nominally anhydrous, the investigated melts contain H_2O concentrations up to 0.23 wt%. The data exhibit a decrease in viscosity of approx. $10^{0.40}$ Pa s for the phonolitic composition with ~ 0.07 wt% CO_2 and a T_g reduced by approx. 14 °C. For the tephritic composition, T_g is approx. 5 °C lower and has a viscosity reduced by $10^{0.25}$ Pa s for the sample containing ~ 0.5 wt% CO_2. Calorimetric measurements of the tephri-phonolite show lowered onset of T_g by approx. 6 °C for the melt with ~ 0.11 wt% CO_2 and T_g of the foidite appears not to be influenced by a CO_2 concentration of ~ 0.37 wt% CO_2. However, these tephri-phonolitic and foiditic melts foamed during calorimetric measurements preventing a reliable measurement. It would appear that most of this overall drop in viscosity is caused by the small amounts of H_2O in the melts with CO_2 slightly reducing the viscosity or having no effect on viscosity. Additionally, it is shown that the reduction in viscosity decreases with an increasing degree of the depolymerisation for the investigated melts. Consequently, the explosive style of the CAVD eruptions is mainly caused by crystals and bubbles which form and rise during magma storage and ascent which increases the magma viscosity whereas the CO_2 in the melt slightly reduces the viscosity.

Keywords Viscosity · Calorimetry · Colli Albani · Carbon dioxide · Glass transition · Foidite

Communicated by Dante Canil.

✉ Christin Kleest
christin.kleest@uni-goettingen.de

[1] Department of Mineralogy, Georg-August-Universität Göttingen, Goldschmidtstraße 1, 37077 Göttingen, Germany

Published online: 15 October 2021

Introduction

Rheology of melts plays a key role in magmatic processes. It influences mass transfer, crystallisation processes, nucleation, forming and exsolution of bubbles, the speed of ascent in the volcanic vent and finally the eruptive style. Rheology is affected by melt composition and its volatile content, temperature, pressure, crystal and bubble content as well as oxygen fugacity (i.e. Webb et al. 2007; Chevrel et al. 2013; Di Genova et al. 2014; Campagnola et al. 2016; Klein et al. 2018; Kolzenburg et al. 2018). Among the volatile components in magmatic systems, CO_2 is the most important one after H_2O (Nowak et al. 2003). In many geological settings with mainly explosive volcanic eruptions, magmas get "flushed" with CO_2 by the entrainment of a CO_2-rich gas from deeper levels of the magmatic systems or by the assimilation of a CO_2-rich host material, i.e. the Colli Albani Volcanic District, Italy (Freda et al. 2011), Mt. Somma-Vesuvius, Italy (Bruno et al. 1998), Popocatépetl volcano, Mexico (Goff et al. 2001) or Merapi volcano, Indonesia (Troll et al. 2012). An enrichment of CO_2 in magma results in changes in the rheological behaviour with a decrease in density, changes in chemistry and mineral assemblage and the formation of bubbles and/or crystals. Hence, CO_2 is often assumed to trigger volcanic eruptions (Blythe et al. 2015; Caricchi et al. 2018). Blythe et al. (2015) pointed out that the viscosity of a melt strongly determines the carbonate assimilation rate when a magma interacts with the carbonate wall rock. In contrast, the influence of CO_2 on melt viscosity is poorly investigated as shown below.

Adding CO_2 to polymerised liquids such as $NaAlSi_3O_8$ (Brearley and Montana 1989) or $KAlSi_3O_8$ (White and Montana 1990) decreases the viscosity at high pressure. In contrast, Brearley and Montana (1989) detected no influence of CO_2 on the viscosity of the more depolymerised liquid $NaCaAlSi_2O_7$. Viscosity studies on a K-rich silicate melt by Bourgue and Richet (2001) exhibit a reducing effect of CO_2 on the viscosity within the first 3 wt% CO_2 added. They also measured a linearly decreasing density of the melt with increasing CO_2 concentration at room temperature. Morizet et al. (2007) inferred viscosity from calorimetric measurements of the glass transition temperature T_g of CO_2-bearing jadeitic and phonolitic melts. They concluded there is little or no influence of dissolved CO_2 on viscosity at temperatures near the glass transition because they saw no systematic variations in T_g. Seifert et al. (2013) did experiments on the relaxation times for basaltic, phonolitic and rhyolitic glasses and showed a reduction in relaxation time with increasing CO_2 content for the basaltic melt but no changes for the other compositions. As a consequence, they deduce CO_2 decreases the viscosity of basaltic melts but does not affect the other SiO_2 rich melts. Di Genova et al. (2014)

investigated rheological features of natural hydrous and H_2O-CO_2-bearing trachybasaltic and latitic compositions. They showed a decrease in viscosities for volatile bearing melts and found a stronger decrease in H_2O-CO_2-bearing melts than for hydrous ones. The glass transition temperature was reduced by ~25 K with the addition of any amount of CO_3^{2-} up to 1900 ppm CO_2. In contrast, the heat capacities are not affected by those volatiles. A study by Robert et al. (2015) on a remelted natural basalt confirms the effect of CO_2 slightly reducing viscosity in the presence of up to 1 wt% H_2O.

The present study investigates the influence of CO_2 on rheological properties of three synthetic equivalents of the Colli Albani Volcanic District (CAVD) and a fourth sample equivalent to the "white pumice" phonolite from the Vesuvius AD 79 eruption (WPVe series) (Iacono-Marziano et al. 2007). To minimise crystallisation and structural changes during experimental runs, all CAVD glasses are made with half the amount of Fe in the natural sample. Fe^{2+} is replaced by Mg^{2+} and Fe^{3+} by Al^{3+}. Glasses of the CAVD are of the foiditic composition from the Pozzolane Rosse event after Freda et al. (2011) (PR-0.5Fe series) and a tephri-phonolitic one from the Pozzolane Nere event after Campagnola et al. (2016) (PN-0.5Fe series). A further tephritic glass is synthesised by subtracting 4 mol% $KAlSi_2O_6$ from the Pozzolane Rosse composition (PR-Leu-0.5Fe series) to investigate the rheology of the residual PR-0.5Fe melt after crystallisation of leucite which is a characteristic phenocryst in the pyroclastic products of the CAVD (i.e. Giordano et al. 2006; Freda et al. 2011).

Methods

Sample preparation

Volatile-free base glasses were made of powdered and previously dried metal oxides and carbonates. They were melted at 1600 °C at ambient pressure and atmosphere for 1 hour and subsequently grinded and mixed for 20 min. This procedure was repeated before the glass was finally melted for the third time for 4 hours. The glasses were quenched by dipping the crucible with the melt in water at ambient temperature. The base glasses are than powdered and dried at 500°C for 20 hours to avoid adsorption of H_2O. The sample powder is filled into $Au_{75}Pd_{25}$ capsules and welded at approx. 500°C. For the CO_2-bearing melts, the powdered base glass is mixed with silver oxalate $Ag_2C_2O_4$ as the source of CO_2 loaded into the capsules and welded at room temperature. The experiments are performed in an internally heated pressure vessel (IHPV) with an intrinsic oxygen fugacity fO_2 = NNO + 3 at 1250 °C and approx. 250 MPa for 46 or 70 hours (for detailed description of the IHPV see Schanofski et al. 2019). The melts are

quenched with a cooling rate of ~150 °C s^{-1} previously determined in similar studies (Benne and Behrens 2003).

Density

Based on Archimedes´ principle, the sample is weighed in air and in distilled H_2O with a wetting agent to reduce the surface tension of H_2O using a Mettler Toledo Excellence XP/XS analyse balance. The calculation of the density ρ follows the equation

$$\rho = \frac{A}{A-B} \times \rho_{H_2O} \quad (1)$$

with A – sample weight in air, B – sample weight in distilled H_2O and ρ_{H2O} – density of the H_2O at ambient temperature after Bigg (1967). The density of every glass is measured 10 times.

Fourier transform infrared spectroscopy (FTIR)

Contents of CO_2 and H_2O are determined by FTIR spectroscopy in the mid-infrared (MIR) range of 1200 – 4000 cm^{-1} and in the near-infrared (NIR) range of 2000 – 6000 cm^{-1}, respectively. Measurements are done with a Bruker Hyperion 3000 IR microscope and a coupled Bruker Vertex 70 FTIR spectrometer. A tungsten lamp, a MCT detector cooled by liquid nitrogen and a KBr beam splitter together with a Globar light source and a CaF_2 beam splitter are used to collect the MIR and NIR spectra, respectively. 100 scans in transmission with 4 cm^{-1} spectral resolution are collected for each spectrum with a spot size of 50 x 50 µm. Samples are double polished and have a thickness of 100 – 190 µm for the MIR spectra and 200 – 250 µm for the NIR spectra.

Colorimetric micro-determination of the iron species

The colorimetric method of Wilson (1960) and Schuessler et al. (2008) was used to determine the Fe speciation. Each sample is powdered and 5 – 15 mg are dissolved in hydrofluoric acid (HF). Upon addition of 2:2´bipyridyl to the solution, a reddish Fe(II)-bipyridyl-complex is built by the Fe^{2+}. This complex has an intensive absorption band at ~523 nm in an UV/VIS spectrum. Hydroxylamine hydrochloride (H_4NOCl) is then used to reduce Fe^{3+} to Fe^{2+} to measure the total Fe content Fe_{tot}. Comparison of the intensities at ~523 nm of the unreduced and reduced solutions provides the ratio of Fe^{2+} to the total Fe content Fe^{2+}/Fe_{tot}. The UV/VIS measurements are performed at an AvaSpec-UV/VIS/NIR spectrometer from Avantes and the AvaSoft software Version 8.3.

Micropenetration technique

Viscosity η is measured using the micropenetration technique with a Netzsch TMA 402 dilatometer in the range $10^{8.5}$ – $10^{13.5}$ Pa s. The calibration of the temperature is done with the melting points of Bi (268.02 °C), Zn (417.02 °C), Al (659.02 °C), NaCl (800.05 °C) and Ag (951.09 °C). The DGG1, a Na_2O-CaO-SiO_2 float glass from the Deutsche Glastechnische Gesellschaft, is measured as a standard glass to determine the precision of the dilatometer. A total error of ±0.06 $\log_{10}$ Pa s (1σ) is assessed for the measurements. Samples with parallel surfaces are double polished and have a thickness of 1.5 mm. A sphere of a single crystal of Al_2O_3 with a diameter of 1 mm is forced into the discs with 0.1 – 1.5 N. Depending on the expected viscosity, the measurements are performed for 30 min up to 6 hours in a temperature range of 600 – 780 °C. The penetration rate of the sphere into the glass disc is used for the calculation of the viscosity by:

$$\eta = \frac{0.1875\, Ft}{r^{0.5} l^{1.5}} \qquad (2)$$

with F – the applied force, t – time, r – radius of the indent sphere, l – distance of indent (Pocklington 1940; Tobolsky and Taylor 1963; Dingwell et al. 1992). As this equation assumes that both the thickness of the sample and the radius of the sphere is much greater than the penetration distance, both F and t are chosen such that l < 80 µm in all of the measurements.

Differential scanning calorimetry (DSC)

Heat capacities are measured with the Netzsch DSC 404C differential scanning calorimeter. The samples are heated to the approximate temperature at which the viscosity is 10^9 Pa s (T_g^9) which is in the temperature range of 730 – 800 °C, depending on the chemical composition. Measurements are performed with a constant heating- and cooling-rate of 20 °C min^{-1}. To erase the thermal history of the glasses, only the second calorimetric run of each sample is used for the determination of the glass transition temperature T_g. Measurements are done in a Pt crucible against an empty Pt crucible and calibrated with a single sapphire crystal with the data of Robie et al. (1978) from 20 to 1000 °C. Measured discs of the WPVe and PR-Leu-0.5Fe series as well as the CO_2-free samples of the PN-0.5Fe and PR-0.5Fe series were double polished with parallel faces. During their first calorimetric runs, the discs of CO_2-bearing samples of the PN-0.5Fe and PR-0.5Fe series foamed and raised the lid of the crucible. Hence, these samples were subsequently crushed to coarse fragments before their measurements.

The configurational heat capacity C_p^{conf} is determined from the scanning data and is the difference between the relaxed heat capacity of the melt and that of the glass at the same temperature just above the glass transition ($C_p^{conf} = C_{pl} - C_{pg}$).

The liquid heat capacity (C_{pl}) is directly given by the heat capacity curve. To extrapolate the heat capacity of the glass (C_{pg}) to a higher temperature, the unrelaxed glass data are fitted by the Maier-Kelley equation:

$$C_{pg} = a + bT + cT^{-2} \quad (3)$$

with *a*, *b*, *c* as parameters and *T* – temperature in Kelvin (Maier and Kelley 1932). The unrelaxed C_{pg} is extrapolated to approx. 150 °C to the temperature at which the relaxed C_{pl} has been determined.

Results

The results of the electron microprobe analysis of the chemical compositions of the investigated melts are listed in Table 1 as well as the chemical compositions calculated with the atomic analysis of the electron microprobe and the Fe ratio Fe^{2+}/Fe_{tot} received from the colorimetric micro-determination. All melts are metaluminous by the definition: $(Na_2O + K_2O) < Al_2O_3 < (CaO + MgO + Na_2O + K_2O)$ in mole fraction (Shand 1927). Fe^{2+}/Fe_{tot} ranges from 0.33 (PR-0.5Fe_0.2) to 0.51 (samples within the PN-0.5Fe series) (Table 1). The degree of polymerisation of the melt structure is given by $\gamma = (Na_2O + K_2O + CaO + MgO + FeO)/(Na_2O + K_2O + CaO + MgO + FeO + Al_2O_3 + Fe_2O_3)$ in mole fraction (Toplis et al. 1997; Webb et al. 2007) and seen in Table 1. The most depolymerised melts are those of the PR-Leu-0.5Fe series ($\gamma = 0.72$), followed by the PR-0.5Fe series ($\gamma = 0.68 – 0.70$) and the PN-0.5Fe series ($\gamma = 0.59 – 0.60$). The melts of the WPVe series have the highest degree of polymerisation ($\gamma = 0.55$). All melts are nominally anhydrous ($H_2O < 0.50$ wt%). The WPVe and PR-Leu-0.5Fe series are crystal free. The PN- 0.5Fe and PR-0.5Fe series contain up to 4 vol% crystals with a mean aspect ratio (= major axes/minor axes) of 1.29 and grain sizes from 2 to 4 µm (Table 2) that formed during the IHPV runs. All CO_2-free glasses are bubble free. The CO_2-bearing samples of the WPVe and the PN-0.5Fe series contain up to 3 vol% spherical bubbles (Table 2). Raman spectroscopy identified the gases in the bubbles as molecular CO_2 with characteristic peaks at 1286 and 1390 cm^{-1} (Schrötter and Klöckner 1979) (for the Raman spectra see Fig. A1 in Appendix A).

Electron microprobe analysis										
[wt%]	SiO_2	Al_2O_3	Na_2O	TiO_2	FeO_{tot}	MnO	MgO	CaO	K_2O	total
WPVe series	55.91±0.16	21.47±0.10	5.29±0.07	0.30±0.03	2.72±0.05	0.13±0.02	0.41±0.01	3.25±0.05	9.48±0.08	98.96
PN-0.5Fe series	50.01±0.16	22.41±0.10	2.50±0.06	0.63±0.02	5.82±0.08	0.19±0.02	3.25±0.03	5.47±0.06	8.92±0.08	99.20
PR-0.5Fe series	43.30±0.15	19.84±0.10	3.04±0.06	0.92±0.04	7.46±0.09	0.20±0.02	5.44±0.04	10.55±0.09	8.47±0.08	99.22
PR-Leu-0.5Fe series	45.20±0.16	18.65±0.10	3.68±0.06	1.14±0.03	5.88±0.08	0.25±0.02	6.16±0.06	13.05±0.09	4.77±0.06	98.78

Calculated compositions													
[mol %]	SiO_2	Al_2O_3	Na_2O	TiO_2	FeO	Fe_2O_3	MnO	MgO	CaO	K_2O	Fe^{2+}/Fe_{tot}	γ^a	M^b
WPVe_0.1	65.17±0.32	14.75±0.12	5.98±0.16	0.26±0.03	1.14±0.03	0.76±0.02	0.12±0.05	0.71±0.06	4.06±0.11	7.04±0.10	0.43±0.02	0.55	69.43
WPVe_0.2	65.13±0.32	14.74±0.12	5.98±0.15	0.26±0.03	1.25±0.05	0.70±0.02	0.12±0.05	0.71±0.06	4.06±0.11	7.04±0.10	0.47±0.03	0.55	69.38
WPVe_1.1	65.17±0.32	14.75±0.12	5.98±0.16	0.26±0.03	1.14±0.03	0.76±0.02	0.12±0.05	0.71±0.06	4.06±0.11	7.04±0.10	0.43±0.02	0.55	69.43
WPVe_1.2	65.15±0.32	14.75±0.12	5.98±0.16	0.26±0.03	1.19±0.03	0.73±0.02	0.12±0.05	0.71±0.06	4.06±0.11	7.04±0.10	0.45±0.02	0.55	69.40
PN-0.5Fe_0.1	58.06±0.31	15.34±0.12	2.81±0.09	0.55±0.04	2.37±0.05	1.64±0.04	0.18±0.03	5.62±0.09	6.81±0.13	6.61±0.10	0.42±0.02	0.59	69.47
PN-0.5Fe_0.2	57.91±0.31	15.30±0.12	2.81±0.09	0.55±0.04	2.88±0.05	1.38±0.04	0.18±0.03	5.61±0.09	6.79±0.13	6.59±0.10	0.51±0.02	0.60	69.40
PN-0.5Fe_1.1	57.91±0.31	15.30±0.12	2.81±0.09	0.55±0.04	2.88±0.05	1.38±0.04	0.18±0.03	5.61±0.09	6.79±0.13	6.59±0.10	0.51±0.02	0.60	69.25
PN-0.5Fe_1.2	57.98±0.31	15.32±0.12	2.81±0.09	0.55±0.04	2.65±0.05	1.50±0.04	0.18±0.03	5.61±0.09	6.80±0.13	6.60±0.10	0.47±0.02	0.59	69.36
PN-0.5Fe_1.3	57.91±0.31	15.30±0.12	2.81±0.09	0.55±0.04	2.88±0.05	1.38±0.04	0.18±0.03	5.61±0.09	6.79±0.13	6.59±0.10	0.51±0.02	0.60	69.25
PR-0.5Fe_0.1	49.22±0.27	13.29±0.10	3.35±0.10	0.78±0.04	2.84±0.04	2.13±0.04	0.19±0.03	9.22±0.11	12.84±0.17	6.14±0.09	0.40±0.02	0.69	68.31
PR-0.5Fe_0.2	49.34±0.27	13.33±0.10	3.36±0.10	0.79±0.04	2.35±0.04	2.38±0.04	0.19±0.03	9.24±0.11	12.87±0.17	6.16±0.09	0.33±0.01	0.68	68.10
PR-0.5Fe_1.1	49.11±0.27	13.26±0.10	3.34±0.10	0.78±0.04	3.26±0.04	1.91±0.04	0.19±0.03	9.20±0.11	12.82±0.17	6.13±0.09	0.46±0.01	0.70	67.92
PR-0.5Fe_1.2	49.22±0.27	13.29±0.10	3.35±0.10	0.78±0.04	2.84±0.04	2.13±0.04	0.19±0.03	9.22±0.11	12.84±0.17	6.14±0.09	0.40±0.01	0.69	68.10
PR-Leu-0.5Fe_0.1	49.85±0.27	12.12±0.10	3.93±0.10	0.94±0.04	2.60±0.06	1.41±0.03	0.23±0.03	10.13±0.15	15.42±0.16	3.36±0.06	0.48±0.01	0.72	65.68
PR-Leu-0.5Fe_0.2	49.87±0.27	12.12±0.10	3.94±0.10	0.94±0.04	2.55±0.06	1.44±0.03	0.23±0.03	10.13±0.15	15.42±0.16	3.36±0.06	0.47±0.02	0.72	65.70
PR-Leu-0.5Fe_1.1	49.88±0.27	12.13±0.10	3.94±0.10	0.94±0.04	2.50±0.06	1.47±0.03	0.23±0.03	10.14±0.15	15.43±0.16	3.36±0.06	0.46±0.01	0.72	65.73
PR-Leu-0.5Fe_1.2	49.91±0.27	12.13±0.10	3.94±0.10	0.94±0.04	2.39±0.04	1.52±0.03	0.23±0.03	10.14±0.15	15.43±0.16	3.36±0.07	0.44±0.02	0.72	65.77
PR-Leu-0.5Fe_1.3	49.85±0.27	12.12±0.10	3.93±0.10	0.94±0.04	2.60±0.06	1.41±0.03	0.23±0.03	10.13±0.15	15.42±0.16	3.36±0.06	0.48±0.02	0.72	65.68

[a] $\gamma = \frac{Na_2O+K_2O+CaO+MgO+FeO}{Na_2O+K_2O+CaO+MgO+FeO+Al_2O_3+Fe_2O_3}$ [b] M = Molecular weight of the glass (g mol^{-1})

Table 1 Chemical compositions of the investigated melts. Columns in wt% show the composition of the base glasses analysed by electron microprobe (JEOL JXA 8900 RL); acceleration voltage: 15 kV, current: 15 nA, beam diameter: 25 µm. Data are the average of 10 single measurements with standard deviation of 1σ. Columns in mol% give the compositions of the melts after the IHPV runs. Data are calculated with the atomic analysis of the electron microprobe and the Fe-ratio measured with the colorimetric micro-determination. Standard deviation is 2σ.

	P [MPa]	t [h]	c(H_2O) [wt%]	c(CO_3^{2-}) [µg g^{-1}]	c(CO_2)^{total} [µg g^{-1}]	ρ [g cm^{-3}]	comments
			FTIR	FTIR	CS		
WPVe_0.1	257	46	0.12 ± 0.01[1]	-	n.d	2.48 ± 0.01	
WPVe_0.2	251	70	0.12 ± 0.01[1]	-	n.d	2.48 ± 0.02	
WPVe_1.1	256	70	0.17 ± 0.02[1]	748 ± 56[3]	n.d.	2.47 ± 0.02	bubbles < 1 vol%
WPVe_1.2	256	70	0.18 ± 0.02[1]	748 ± 65[3]	n.d	2.47 ± 0.01	bubbles < 1 vol%
PN-0.5Fe_0.1	252	46	0.23 ± 0.02[2]	-	n.d	2.60 ± 0.01	crystals ~4vol%
PN-0.5Fe_0.2	254	70	0.20 ± 0.02[2]	-	n.d	2.60 ± 0.01	crystals ~3vol%
PN-0.5Fe_1.1	254	70	0.22 ± 0.02[2]	1020 ± 61[4]	n.d	2.59 ± 0.01	crystals ~3vol%, bubbles ~3 vol%
PN-0.5Fe_1.2	254	70	0.21 ± 0.02[2]	1090 ± 67[4]	n.d	2.58 ± 0.01	crystals ~3vol%, bubbles ~3 vol%
PN-0.5Fe_1.3	254	70	0.22 ± 0.02[2]	1178 ± 62[4]	n.d	2.57 ± 0.01	crystals ~3vol%, bubbles ~3 vol%
PR-0.5Fe_0.1	247	70	0.18 ± 0.02[1]	-	n.d	2.72 ± 0.01	crystals ~3vol%
PR-0.5Fe_0.2	252	46	0.23 ± 0.02[1]	-	n.d	2.73 ± 0.01	crystals ~4vol%
PR-0.5Fe_1.1	255	46	0.14 ± 0.01[1]	3122 ± 74[5]	n.d	2.71 ± 0.01	crystals ~2vol%
PR-0.5Fe_1.2	255	46	0.17 ± 0.02[1]	3672 ± 657[5]	n.d	2.70 ± 0.02	crystals ~2vol%
PR-Leu-0.5Fe_0.1	253	46	0.16 ± 0.01[2]	-	n.d	2.74 ± 0.01	
PR-Leu-0.5Fe_0.2	251	70	0.17 ± 0.01[2]	-	n.d	2.74 ± 0.01	
PR-Leu-0.5Fe_1.1	256	46	0.19 ± 0.02[2]	2988 ± 152[6]	2907[7]	2.73 ± 0.02	
PR-Leu-0.5Fe_1.2	254	46	0.20 ± 0.02[2]	4083 ± 138[6]	3966[7]	2.72 ± 0.01	
PR-Leu-0.5Fe_1.3	256	46	0.18 ± 0.02[2]	5052 ± 169[6]	5019[7]	2.71 ± 0.01	

[1] ε_{3550} = 67.0 ± 6.7 l mol^{-1} cm^{-1} (Stolper 1982)
[2] ε_{3550} = 63.9 ± 5.4 l mol^{-1} cm^{-1} (Behrens et al. 2009)
[3] ε_{1425} = 245 ± 17 l mol^{-1} cm^{-1} (Schanofski et al. 2019)
[4] ε_{1425} = 296 l mol^{-1} cm^{-1} (calculated after Dixon and Pan 1995)
[5] ε_{1425} = 334 l mol^{-1} cm^{-1} (calculated after Dixon and Pan 1995)
[6] ε_{1425} = 324 ± 0.06 (1σ) l mol^{-1} cm^{-1} (this study)
[7] no error given for the PR-Leu-0.5Fe series since the CO_2^{total} was determined once by CS analysis

Table 2 Conditions during IHPV runs, water concentration c(H_2O) determined by FTIR, concentration of the carbon ion c(CO_3^{2-}) determined by FTIR, total carbon concentration c(CO_2)^{total} measured by carbon sulphur (CS) analysis and density ρ. All errors are 1σ for evaluations in this study, errors of absorptions coefficients of ε_{3550} and ε_{1425} from the literature are 2σ (see references). The crystals in the melts of the PN-0.5Fe and PR-0.5Fe series have grain sizes ranging from 2 to 4 µm and a mean aspect ratio (= major axes/minor axes) of 1.29.

The crystals as well as the bubbles are unconnected in the crystal and bubble bearing glasses. All glasses are checked for homogeneity by the FTIR. The CO_2-bearing melts of the PR-0.5Fe series showed little variations of the CO_2 concentration within the samples. Thus, the CO_2 concentration of these melts are determined after their viscosity and heat capacity measurements and given in Table 2.

Density

The densities are shown in Table 2. The WPVe series has the lowest densities with 2.47-2.48 g cm^{-3}, followed by the PN-0.5Fe series with 2.57 – 2.60 g cm^{-3}. The PR-0.5Fe and the PR-Leu-0.5Fe series have similar densities, ranging from 2.70 -2.73 and 2.71 – 2.74 g cm^{-3}, respectively. Within each series of the investigated melts the density appears to decrease with increasing CO_2 concentration (Fig. 1A). This decrease in density is, however, within the error of the density of the volatile-free glasses.

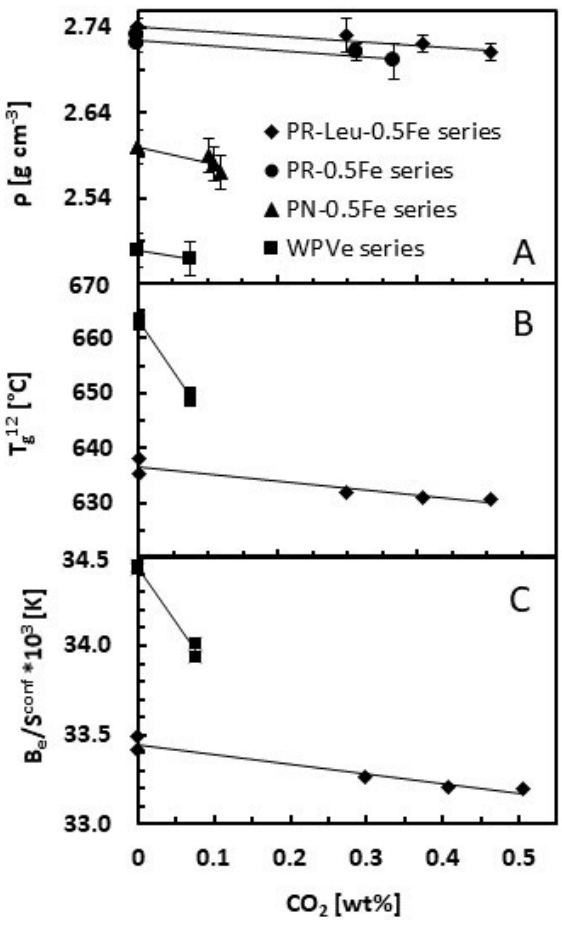

Fig. 1 A – Densities of the investigated melts as a function of CO_2 concentration; B – T_g^{12} vs CO_2 concentration for the WPVe and PR-Leu-0.5Fe series; C – B_e/S^{conf} vs CO_2 content for the WPVe and PR-Leu-0.5Fe series. Symbols for the melt series are the same for the three panels.

FTIR spectroscopy

The relation between the concentration of a species and the IR-absorbance is given by the Lambert-Beer-law:

$$c_i = \frac{M_i \times A_j}{d \times \rho \times \varepsilon_j} \times 100 \quad (4)$$

with c_i – concentration of the species i in wt%, M_i – molar mass of the species i, A_j – peak height of the absorbance of the band j, d – thickness of the sample in cm, ρ – density of the sample in g l^{-1}, ε – absorption coefficient in l mol^{-1} cm^{-1}(i.e. Stolper 1982; Thibault and Holloway 1994; Behrens et al. 2009).

The height of the FTIR-absorption bands related to the carbon species is determined by subtracting the spectrum of the CO_2-free glass from that of the CO_2-bearing sample scaled to the same thickness. As shown in Fig. 2A, the residual spectrum of the PR-Leu-0.5Fe series shows a doublet at approx. 1510 and 1425 cm^{-1}, caused by the asymmetric stretching vibration of CO_3^{2-} (Blank and Brooker 1994; Botcharnikov et al. 2006). To quantify the concentration of the CO_3^{2-} species, the absorbance at approx. 1425 cm^{-1} is used since the doublet is assumed to be symmetric (Dixon and Pan 1995) and the absorbance at 1510 cm^{-1} could be overlapped by a vibration mode of H_2O molecules (Botcharnikov et al. 2006) and hence falsify the evaluation of the carbon concentration. For this PR-Leu-0.5Fe series, the composition dependent absorption coefficient ε_{1425} is calculated using the absorbance normalised by thickness of the glass chip and density and the total carbon content determined by the carbon sulphur (CS) analysis (Table 2). The value for ε_{1425} is 324 ± 12 (2σ) l mol^{-1} cm^{-1} (see Fig. B1 in Appendix B) being in good agreement with that calculated for Ca-rich silicate glasses from Dixon and Pan (1995) with ε_{1425} = 335 l mol^{-1} cm^{-1}.

The FTIR spectra of the WPVe and the PN-0.5Fe series show the doublet of CO_3^{2-} and an extra peak at approx. 2350 cm^{-1} as shown in Fig. 2B. This extra peak is caused by the asymmetric stretching vibration of CO_2 molecules (Blank and Brooker 1994). Since the Raman spectrum (Fig. A1 in Appendix A) attests the presence of molecular CO_2 in the bubbles, it is assumed that this extra peak arises from the substance in the bubbles. The CO_2 species in the presented melts is assumed to be dissolved as CO_3^{2-} only since Fine and Stolper (1986), Thibault and Holloway (1994), Behrens et al. (2009), Shishkina et al. (2014) as well as Schanofski et al. (2019) detected no molecular CO_2 in their bubble free basaltic, Ca-rich leucititic, phono-tephritic, mafic melts as well as phonolitic and foiditic melts, respectively. Therefore, the CS analysis overestimates the total amount of CO_2 in these samples and is not reliable for the

determination of ε_{1425} for these melts (an example of the falsified determination of ε_{1425} is given in Fig. B2 in Appendix B). Due to the underestimations of the absorption coefficients of the bubble bearing melts and the inhomogeneity in CO_2 distribution of the CO_2-bearing melts of the PR-0.5Fe series, ε_{1425} values of 245 l mol^{-1} cm^{-1} (Schanofski et al. 2019), 296 l mol^{-1} cm^{-1} and 334 l mol^{-1} cm^{-1} (calculated after Dixon and Pan 1995) are used for the determination of the CO_3^{2-} content for the WPVe, PN-0.5Fe and the PR-0.5Fe series, respectively. Determined concentrations of CO_3^{2-} are listed in Table 2.

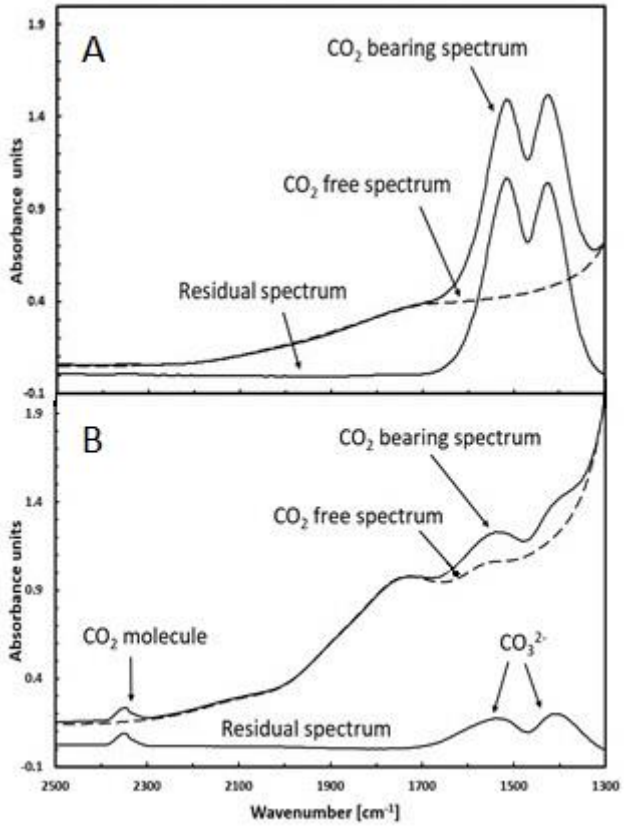

Fig. 2 A – MIR spectra of the CO_2-bearing melt PR-Leu-0.5Fe_1.3 (continuous line) and the corresponding CO_2-free spectra normalised to the thickness of the CO_2-bearing one (dashed line). The residual spectrum is the result of the subtraction of the CO_2-bearing minus the CO_2-free spectra whose absorbance at ~1425 cm^{-1} is used for the determination of the concentration of CO_3^{2-}; B – MIR spectra of the CO_2-bearing melt WPVe_1.1 (continuous line) and the corresponding CO_2-free spectra normalised to the thickness of the CO_2-bearing one (dashed line). The residual spectrum is the result of the subtraction of the CO_2-bearing minus the CO_2-free spectra. Besides the CO_3^{2-} doublet at 1425 and 1510 cm^{-1} a peak at 2350 cm^{-1} exists indicating the presence of molecular CO_2 in this melt.

In the NIR spectra, weak absorbances at approx. 3550 cm^{-1} are caused by the fundamental OH stretching mode (Stolper 1982; Ohlhorst et al. 2001; Behrens et al. 2009). A two-tangent baseline is used to determine the peak height at 3550 cm^{-1}. There is no evidence of molecular H_2O in the glasses, since there is no absorbance peak at approx. 5200 cm^{-1} which is in agreement with previous studies (i.e. Stolper 1982; Behrens et al. 2009) who observed the OH^- groups to be the predominant H_2O species in H_2O bearing glasses with total H_2O content < 0.5 wt%. For the calculation of the total amount of H_2O, values for the absorption coefficients ε_{3550} are taken from other surveys since they strongly depend on melt composition. Stolper (1982) calibrated an absorption coefficient ε_{3550} for variable compositions ranging from basaltic to albitic to rhyolitic and found it to be the same within error and is 67.0 ± 6.7 l mol^{-1} cm^{-1}. Behrens et al (2009) found ε_{3550} for a phono-tephritic glass to be 63.9 ± 5.4 l mol^{-1} cm^{-1}. For the measurements of the H_2O contents of the melts in this study, ε_{3550} = 67.0 ± 6.7 l mol^{-1} cm^{-1} and ε_{3550} = 63.9 ± 5.4 l mol^{-1} cm^{-1} are used for the WPVe and PR-0.5Fe series as well as for the PN-0.5Fe and PR-Leu-0.5Fe series, respectively. The melts contain H_2O concentrations up to 0.23 wt% (Table 2) due to the reduction of Fe^{3+} in the samples by hydrogen following the reaction $Fe_2O_3 + H_2 \rightarrow 2FeO + H_2O$ (Brearley and Montana 1989; Botcharnikov et al. 2006; Behrens et al. 2009) during sample preparation in the IHPV. An additional possibility for H_2O entry into the samples could be adsorbed H_2O on the $Ag_2C_2O_4$ dissolved during the experimental run in the IHPV.

Viscosity

The measured viscosities at a given temperature of all melts are given in the supplementary material (Appendix C)**.** Due to the narrow temperature range applied in this study the statistical analysis needs to fit a straight line through the measured viscosity data which is given by the Arrhenian Equation

$$log_{10}\,\eta = A + \frac{B \times 10^4}{T} \quad (5)$$

with η – viscosity in Pa s, A and B as – fit parameters and T – temperature in Kelvin. All fit parameters are listed in Table 3.

	A [log_{10} Pa s]	B [K]	T_g^{12} [°C]	m
WPVe_0.1	-16.50 ± 0.04	2.67 ± 0.01	663.5	28.5
WPVe_0.2	-15.01 ± 0.09	2.53 ± 0.01	662.5	27.0
WPVe_1.1	-15.27 ± 0.05	2.52 ± 0.01	650.2	27.3
WPVe_1.2	-13.46 ± 0.05	2.35 ± 0.01	648.5	25.5
PN-0.5Fe_0.1	-16.65 ± 0.04	2.71 ± 0.01	674.5	28.6
PN-0.5Fe_0.2	-16.16 ± 0.05	2.66 ± 0.01	670.1	28.2
PN-0.5Fe_1.1	n.d.	n.d.	n.d.	n.d
PN-0.5Fe_1.2	n.d.	n.d.	n.d.	n.d
PN-0.5Fe_1.3	n.d.	n.d.	n.d.	n.d
PR-0.5Fe_0.1	-16.67 ± 0.13	2.61 ± 0.02	638.4	28.7
PR-0.5Fe_0.2	-16.19 ± 0.18	2.56 ± 0.03	634.8	28.2
PR-0.5Fe_1.1	n.d.	n.d.	n.d.	n.d.
PR-0.5Fe_1.2	n.d.	n.d.	n.d.	n.d.
PR-Leu-0.5Fe_0.1	-29.23 ± 0.06	3.76 ± 0.01	637.9	41.2
PR-Leu-0.5Fe_0.2	-26.71 ± 0.05	3.52 ± 0.01	635.4	38.7
PR-Leu-0.5Fe_1.1	-28.20 ± 0.03	3.64 ± 0.01	631.8	40.2
PR-Leu-0.5Fe_1.2	-28.61 ± 0.04	3.67 ± 0.01	631.0	40.6
PR-Leu-0.5Fe_1.3	-28.87 ± 0.04	3.69 ± 0.01	630.6	40.9

Table 3 Fit parameter for the Arrhenian Equation (Eq. 5), T_g^{12} and fragility m (Eq. 7) calculated with the viscosity data

The CO_2-bearing samples WPVe_1.1 and WPVe_1.2 contain < 1 vol % spherical bubbles and show bubble growth and rise at temperatures > 700°C, and therefore these data are not shown. Einstein (1906) developed a formula for the effect of suspended isolated spheres on melt viscosity:

$$\eta_{rel} = \frac{\eta_{eff}}{\eta_{melt}} = 1 + f * \varphi \quad (6)$$

with η_{rel} – relative viscosity, η_{eff} – effective viscosity of the dilute suspension in Pa s, η_{melt} – viscosity of the pure suspending liquid in Pa s, f – constant that is 1 for spherical bubbles (Taylor 1932) and φ – bubble fraction.

For the CO_2-bearing samples, the influence of the present bubbles on viscosity is < 0.01 log_{10} Pa s and hence negligible. As seen in Fig. 3A, the viscosities of the CO_2-free melts of the WPVe series agree with each other within the measurement error of 0.06 log_{10} Pa s. At a temperature of 650°C, the viscosities of the samples WPVe_0.1 and WPVe_0.2 are 12.42 and 12.37 log_{10}

Pa s, respectively. The viscosities of the CO_2-bearing samples, having the same CO_2 content, are about 0.4 $\log_{10}$ Pa s lower at this temperature, namely 12.01 $\log_{10}$ Pa s for WPVe_1.1 and 11.96 $\log_{10}$ Pa s for WPVe_1.2. The glass transition temperature T_g[12] for the CO_2-bearing melts is approx. 14 °C lower with respect to that of the CO_2-free samples of this series (see Fig. 1B and Table 3).

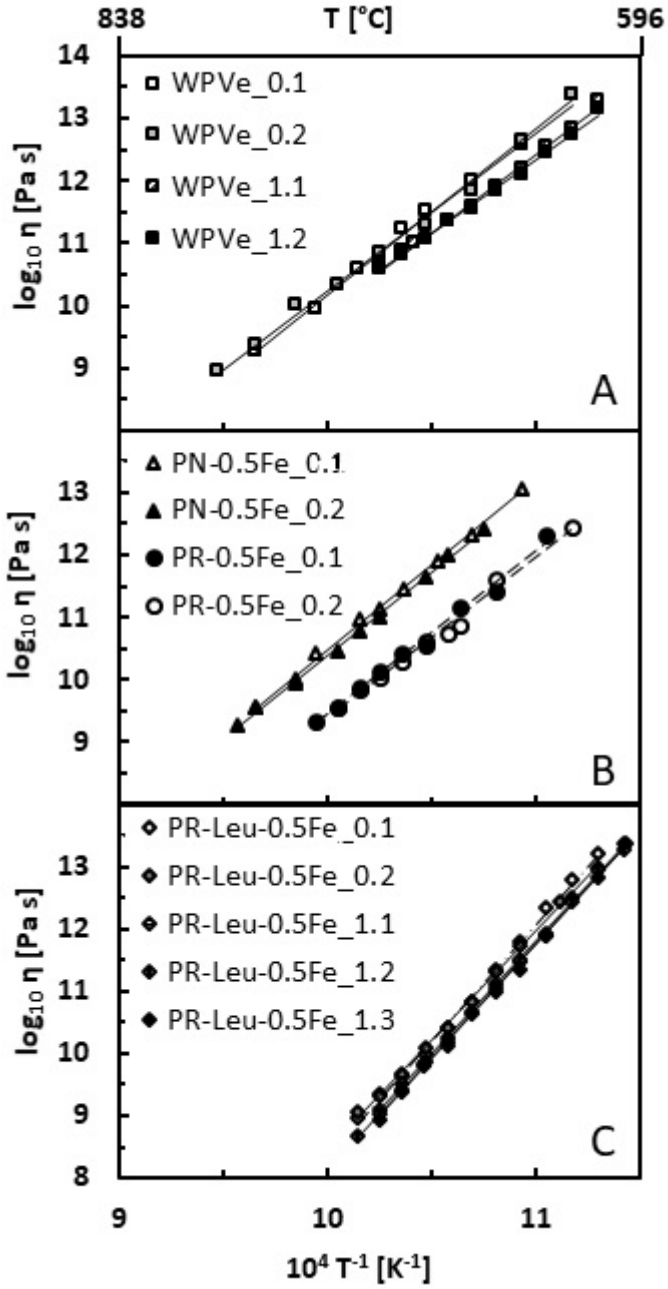

Fig. 3 Viscosity data of all melts investigated in this study as a function of inverse temperature for: A – the CO_2-free and CO_2-bearing melts of the WPVe series, B – the CO_2-free PN-0.5Fe and PR-0.5Fe melts and C – the CO_2-free and CO_2-bearing melts of the PR-Leu-0.5Fe series. The measured temperature range in °C is given at the top of the figure.

The CO_2-bearing melts of the PN-0.5Fe and the PR-0.5Fe series disintegrated during heating before reaching the temperature of measurement. It is assumed, that gases in existing or forming bubbles in the PN-0.5Fe series and PR-0.5Fe series, respectively, expand and lead to the fragmentation of these melts. Therefore, only the viscosities of the CO_2-free melts are investigated.

As illustrated in Fig. 3B, the viscosity of PN-0.5Fe_0.1 is approx. 0.1 $\log_{10}$ Pa s higher than those of PN-0.5Fe_0.2 over the whole temperature range i.e. at 700 °C the viscosity is 11.25 $\log_{10}$ Pa s and 11.13 $\log_{10}$ Pa s, respectively. The viscosities of the CO_2-free samples of the PR-0.5Fe series are additionally shown in Fig. 3B. At a temperature of 700 °C, the viscosity of PR-0.5Fe_0.1 is 10.18 $\log_{10}$ Pa s and that from PR-0.5Fe_0.2 is 10.11 $\log_{10}$ Pa s differing by 0.07 $\log_{10}$ Pa s.

Fig. 3C shows the viscosities of the PR-Leu-0.5Fe series. The viscosity data of the CO_2-free samples agree with each other, i.e. at 650°C the viscosities for PR-Leu-0.5Fe_0.1 and PR-Leu-0.5Fe_0.2 are 11.41 and 11.39 $\log_{10}$ Pa s, respectively, what is within the error of measurements. The viscosities of the samples with a CO_2 concentration of ~0.30 wt% (PR-Leu-0.5Fe_1.1), ~0.40 wt% (PR-Leu-0.5Fe_1.2) and ~0.50 wt% (PR-Leu-0.5Fe_1.3) are 0.18, 0.22 and 0.25 $\log_{10}$ Pa s lower, respectively, compared to the CO_2-free PR-Leu-0.5Fe_0.2. The glass transition temperature T_g^{12} of the CO_2-bearing melts decreases by approx. 5 °C with respect to PR-Leu-0.5Fe_0.2 (see Fig. 1B and Table 3).

Fragility

Using the viscosity data, the fragility m is calculated by

$$m = \frac{B \times 10^4}{T_g^{12}} \tag{7}$$

with B – fit parameter from the Arrhenian fit (Eq. 5) and T_g^{12} – temperature at which the viscosity is 10^{12} Pa s in Kelvin (Toplis et al. 1997; Webb 2011).

As demonstrated in Table 3, the PR-Leu-0.5Fe series has the highest fragilities (38.7 – 41.2) whereas the fragilities of all other melts for which viscosity measurements are possible, are nearly the same (25.5 – 28.7).

The Vogel-Fulcher-Tammann Equation (VFT Equation)

$$log_{10}\eta = A_{VFT} + \frac{B_{VFT}}{T - C_{VFT}} \quad (8)$$

with A_{VFT} – constant, B_{VFT} and C_{VFT} – parameters and T – temperature in Kelvin (i.e. Toplis et al. 1997), can be used to force a curve in the fit to the viscosity data. This requires setting the constant A_{VFT} to -4 (see Kleest et al. (2020) for a discussion). Corresponding to the VFT Equation (Eq. 8), the fragility m_{VFT} is then:

$$m_{VFT} = \frac{B_{VFT}}{T_g^{12}(1 - C_{VFT}/T_g^{12})^2} \quad (9)$$

The constant A_{VFT}, the parameters B_{VFT} and C_{VFT} as well as the fragilities using Eq. 9 are given in the supplemental material (Appendix D).

Differential scanning calorimetry (DSC)

The extrapolated parameters of the Maier-Kelley-Fit (Eq. 3) of the studied melts are listed in Table 4 together with the heat capacities of the glasses (c_{pg}) and liquids (c_{pl}) and the configurational heat capacity C_p^{conf}. C_p^{conf} is lowest for the WPVe series (10.35 – 12.42 J mol^{-1} K^{-1}), followed by the PN-0.5Fe series (13.76 – 16.38 J mol^{-1} K^{-1}). The PR-0.5Fe series has similar C_p^{conf} (20.70 – 26.3 J mol^{-1} K^{-1}) to the PR-Leu-0.5Fe series (25.31 – 26.93 J mol^{-1} K^{-1}). Fig. 4 shows a positive correlation between C_p^{conf} and the degree of depolymerisation expressed by γ which is in agreement with previous studies from Giordano and Russell (2017) and Russell and Giordano (2017) who demonstrated that C_p^{conf} diminishes with increasing SiO_2 content. An increase of SiO_2 increases the degree of polymerisation and hence a lower re-ordering of the structure in the melt is required at the glass transition range resulting in lower C_p^{conf}.

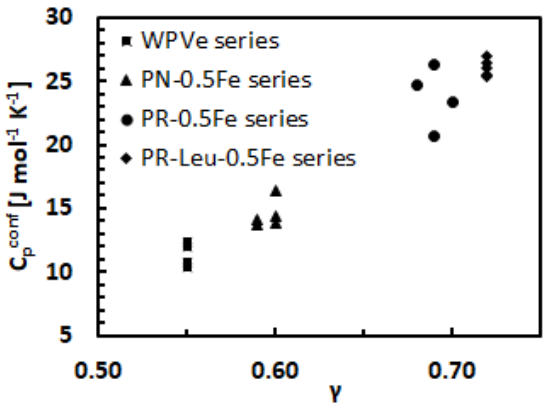

Fig. 4 Configurational heat capacity C_p^{conf} as a function of γ: the higher the degree of polymerisation the lower C_p^{conf}

The fragmentation of the CO_2-bearing glasses of the PN-0.5Fe and PR-0.5Fe series prevented viscosity measurements, however, the calorimetric data can be used to estimate the viscosities. Scherer (1984) postulated a relation between viscosity in the glass transition range and the cooling-rate during calorimetric measurements:

$$log_{10}\eta\left(T_g^{Onset}\right) = K_{Onset} - log|q| \quad (10)$$

with η – viscosity in Pa s, T_g^{Onset} – temperature at the beginning of the glass transition range, defined by the extrapolated glassy heat capacity via the Maier-Kelley fit (Eq. 3) and the rapid increase in heat capacity, K_{Onset} – shift factor of 11.3 and q – cooling rate in °C s^{-1}.

K_{Onset} is calculated for each sample for which viscosity data are available. The average of K_{Onset} ($øK_{Onset}$) for each melt series is used for further investigations of the CO_2-bearing melts and is listed in Table 4 as well as T_g^{Onset}.

K_{Onset} varies from 11.56 ± 0.05 for the PR-0.5Fe series to 11.86 ± 0.10 for the WPVe series. K_{Onset} is assumed to be independent of the chemical composition (Stevenson et al. 1995). However, Stevenson et al. (1995) argued that K_{Onset} slightly decreases with increasing agpaitic index ($(Na_2O + K_2O)/Al_2O_3$ in mol. fraction). As seen in Fig. 5 showing $øK_{Onset}$ of each series vs SiO_2 concentration, $øK_{Onset}$ slightly increases with increasing SiO_2 content. Conventionally implicating a more polymerised melt with increasing SiO_2 content, this observation agrees with that from Stevenson et al. (1995) treating the agpaitic index as an indication of the degree of polymerisation of a melt.

The CO_2-bearing melts of the WPVe and PN-0.5Fe series contain bubbles of < 1 vol% and 3 vol%, respectively. Based on Eq. 6, the influence of bubbles on viscosity is < 0.01 log_{10} Pa s for the WPVe melts and 0.01 log_{10} Pa s for the PN-0.5Fe melts which is within the measurement error of 0.06 log_{10} Pa s.

The calorimetrically determined viscosities are shown in Fig. 6, presented as the difference in log_{10} η at T_g^{Onset} between the CO_2-free and the CO_2-bearing samples of each series vs CO_2 concentration. For the WPVe, the PN-0.5Fe as well as for the PR-Leu-0.5Fe series, the CO_2-bearing melts have lower viscosities at T_g^{Onset} than the CO_2-free melts.

The viscosity of the WPVe_1.1 sample decreases by 0.39 log_{10} Pa s and the WPVe_1.2 sample has a viscosity drop of 0.60 log_{10} Pa s with respect to the CO_2-free WPVe_0.1 melt. In contrast to the results of the viscosity measurements, the viscosities of the CO_2-bearing melts of the WPVe series differ by 0.21 log_{10} Pa s at T_g^{Onset}.

	Maier-Kelley parameters									
	a [J g^{-1} K^{-1}]	b [J g^{-1} K^{-2}]	c*10^3 [J K g^{-1}]	c_{pg} [J g^{-1} K^{-1}]	C_{pl} [J mol^{-1} K^{-1}]	C_p^{conf} [J mol^{-1} K^{-1}]	S^{conf} [J mol^{-1} K^{-1}]	B_e [kJ mol^{-1}]	T_g^{Onset} [°C]	$\emptyset K_{Onset}$
WPVe_0.1	1.310 ± 0.006	93.61 ± 6.28	-53.57 ± 0.92	1.16	91.16	10.35	12.49 ± 0.64	430.18 ± 21.65	657.3	11.86 ± 0.10
WPVe_0.2	1.298 ± 0.004	-82.21 ± 4.33	-60.89 ± 0.60	1.16	92.62	12.42	16.38 ± 0.96	563.78 ± 32.28	651.0	
WPVe_1.1	1.266 ± 0.005	-95.76 ± 4.84	-52.59 ± 0.69	1.12	88.38	10.76	14.99 ± 0.62	509.60 ± 20.79	640.3	
WPVe_1.2	1.187 ± 0.003	-39.84 ± 2.62	-50.80 ± 0.35	1.10	88.14	12.01	19.86 ± 0.98	673.98 ± 33.16	633.8	
PN-0.5Fe_0.1	1.132 ± 0.003	101.68 ± 3.11	-48.60 ± 0.45	1.19	96.35	13.76	16.27 ± 0.71	567.64 ± 24.28	667.5	11.71 ± 0.03
PN-0.5Fe_0.2	1.324 ± 0.003	-121.52 ± 3.17	-71.34 ± 0.45	1.13	94.94	16.38	19.07 ± 0.69	663.15 ± 23.06	665.0	
PN-0.5Fe_1.1	1.089 ± 0.002	-42.65 ± 2.03	-48.66 ± 0.29	1.00	82.96	13.85	n.d.	n.d.	659.8	
PN-0.5Fe_1.2	1.040 ± 0.003	147.49 ± 2.57	-42.08 ± 0.37	1.15	93.98	14.15	n.d.	n.d.	659.5	
PN-0.5Fe_1.3	1.060 ± 0.002	80.80 ± 1.67	-44.14 ± 0.23	1.10	90.51	14.40	n.d.	n.d.	659.0	
PR-0.5Fe_0.1	1.183 ± 0.005	-23.50 ± 4.89	-53.81 ± 0.65	1.10	101.65	26.30	29.27 ± 2.06	983.97 ± 66.08	636.8	11.56 ± 0.05
PR-0.5Fe_0.2	1.327 ± 0.007	-120.77 ± 7.32	-63.27 ± 1.03	1.14	102.56	24.72	29.07 ± 2.42	973.08 ± 77.64	636.5	
PR-0.5Fe_1.1	1.232 ± 0.013	-79.63 ± 12.73	-50.71 ± 1.79	1.10	98.08	23.30	n.d.	n.d.	637.3	
PR-0.5Fe_1.2	1.190 ± 0.018	-36.12 ± 17.92	-45.13 ± 2.59	1.11	96.23	20.70	n.d.	n.d.	636.3	
PR-Leu-0.5Fe_0.1	1.128 ± 0.004	186.12 ± 3.71	-51.74 ± 0.50	1.25	108.70	26.47	15.15 ± 0.31	507.37 ± 10.10	634.8	11.61 ± 0.09
PR-Leu-0.5Fe_0.2	1.253 ± 0.005	-0.19 ± 4.76	-61.90 ± 0.65	1.19	104.13	26.08	16.53 ± 0.48	552.46 ± 15.35	635.3	
PR-Leu-0.5Fe_1.1	1.264 ± 0.003	-15.91 ± 3.16	-57.93 ± 0.43	1.19	103.33	25.31	15.38 ± 0.36	511.47 ± 11.72	630.3	
PR-Leu-0.5Fe_1.2	1.304 ± 0.003	-95.46 ± 3.50	-65.37 ± 0.47	1.14	100.63	25.45	14.85 ± 0.38	493.12 ± 12.24	626.8	
PR-Leu-0.5Fe_1.3	1.332 ± 0.004	-106.70 ± 3.67	-64.79 ± 0.49	1.16	103.05	26.93	15.92 ± 0.47	528.55 ± 15.09	626.0	

Table 4 All values measured or derived from the DSC data: fit parameters a, b and c from the Maier-Kelley fit (Eq. 3), glassy and liquid heat capacities c_{pg} and c_{pl}, respectively, configurational heat capacity C_p^{conf}, configurational entropy S^{conf}, the B_e parameter (Eq. 11), T_g^{Onset} and the mean value for the shift factor K_{Onset} of each melt series (Eq. 10)

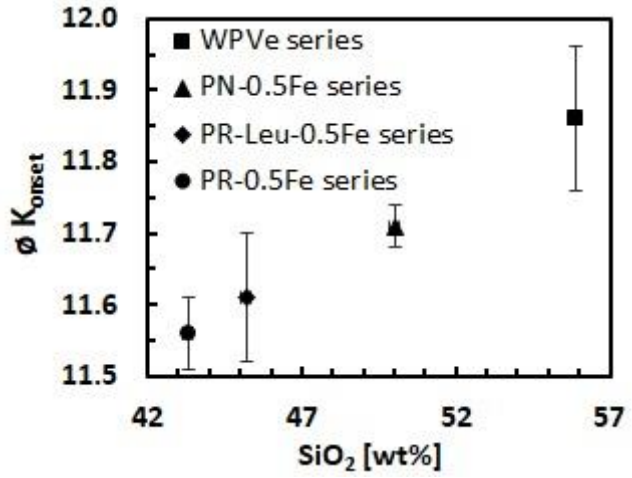

Fig. 5 Average of the shift factor K_{Onset} of each melt series vs SiO_2

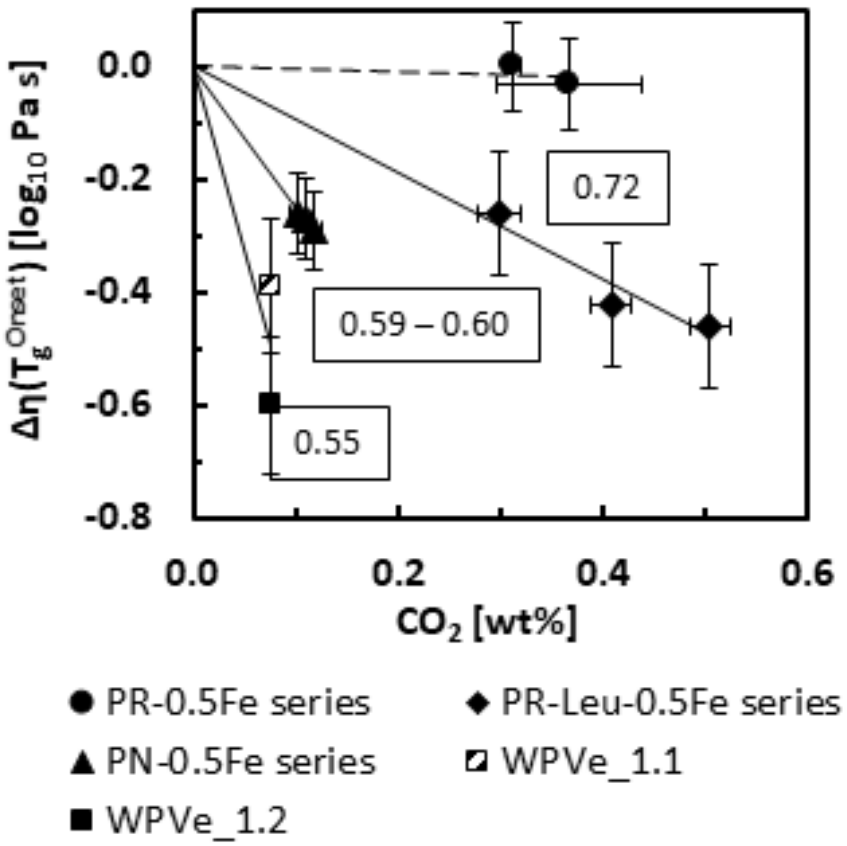

Fig. 6 The viscosity differences of the CO_2-bearing and CO_2-free melts of each series at T_g^{Onset} from DSC measurements vs CO_2 concentration. Numbers in rectangles next to the intrapolated lines of each melt series are γ as a value of the degree of polymerisation. The viscosity drop decreases with increasing γ and hence with increasing degree of depolymerisation.

The viscosity of the CO_2-bearing melts with approx. 0.10 to 0.12 wt% CO_2 of the PN-0.5Fe series decreases by approx. 0.27 log_{10} Pa s in comparison to PN-0.5Fe_0.1 at T_g^{Onset}.

The PR-Leu-0.5Fe_1.1 sample with a CO_2 concentration of ~0.30 wt% has a viscosity diminished by 0.26 log_{10} Pa s and the viscosities of PR-Leu-0.5Fe_1.2 and PR-Leu-0.5Fe_1.3 with an increased CO_2 content up to ~0.50 wt% CO_2 are reduced up to 0.46 log_{10} Pa s at T_g^{Onset} with respect to the PR-Leu-0.5Fe_0.1 sample.

A difference in viscosity of the PR-0.5Fe series is not detectable since the decrease in viscosity is 0.01 and 0.03 log_{10} Pa s for PR-0.5Fe_1.1 and PR-0.5Fe_1.2 compared to the CO_2-free PR-0.5Fe_0.1 melt which is within the error. However, the CO_2-bearing melts of the PR-0.5Fe series foamed during DSC measurements resulting in an incorrect evaluation of T_g^{Onset} and consequently to an incorrect calculated viscosity at T_g^{Onset}. Since the formation of bubbles due to exsolution of volatiles in the melt already occurs during the first calorimetric run, it shifts the glass transition range in the second run to higher temperatures and hence an increased T_g^{Onset} and diminishes the resulting differences in viscosity of the CO_2-free and CO_2-bearing melts.

The Adam-Gibbs theory combines the data from viscosity and DSC measurements and enables the calculation of the configurational entropy S^{conf}:

$$log_{10}\eta = A_e + \frac{B_e}{ln\,10\left[S^{conf}(T_g^{12}) + \int_{T_g^{12}}^{T} \frac{C_p^{conf}}{T} dT\right]T} \quad (11)$$

with A_e and B_e as constants, T_g^{12} – temperature at which the viscosity is 10^{12} Pa s in Kelvin (calculated using the Arrhenian Fit Eq. 5), T – temperature in Kelvin and C_p^{conf} – configurational heat capacity ($C_p^{conf} = C_{pl} - C_{pg}$; C_{pl} is directly measured by DSC and C_{pg} is extrapolated via Eq. 3) (Adam and Gibbs 1965; Richet 1984; Toplis et al. 1997; Webb 2008) which is valid with the assumption of no variations in S^{conf} at temperatures below T_g^{12}. The parameter A_e defines the viscosity at infinite temperature and is assumed to be constant for all compositions (i.e. Toplis et al. 1997; Toplis 1998; Giordano et al. 2008). In the present study, A_e is chosen to be - 4.00 log_{10} Pa s following the Maxwell relation $\tau = \eta_0/G$ (with τ – relaxation time, η_0 = time-independent Newtonian viscosity and G = elastic shear modulus) with $\tau_0 = 10^{-14}$ s (τ_0 = vibration frequency at infinite temperature) (Martinez and Angell 2001; Angell et al. 2003) and $G_\infty = 10 \pm 0.5$ GPa (G_∞ = shear modulus at infinite frequency) (Dingwell and Webb 1989). For a detailed discussion of A_e see Kleest et al. (2020) and references therein.

Eq. 11 fits both, the parameter B_e and the configurational entropy S^{conf} and the results are shown in Table 4. S^{conf} of the WPVe series, the PN-0.5Fe series and the PR-Leu-0.5Fe series are in a similar range (12.49 – 19.86 J mol^{-1} K^{-1}), and the PR-0.5Fe series has the highest S^{conf} (29.07 and 29.27 J mol^{-1} K^{-1}). The ratio B_e/S^{conf} indicates the changes of the potential energy barrier to viscous flow (Richet 1984; Toplis 1998; Webb 2005) and the smallest unit moving in a melt structure (Toplis 1998). Fig. 1C shows B_e/S^{conf} as a function of the CO_2 concentration and it is seen that the CO_2-bearing melts have a lower B_e/S^{conf} than the CO_2-free melts which is more pronounced for the WPVe series than for the PR-Leu-0.5Fe series with a drop of of $0.51x10^3$ and $0.29x10^3$ K, respectively. Hence, the CO_2-bearing melts needs to overcome a lower energy barrier to viscous flow.

Discussion

As shown in Figs. 1B, 3A and 6, the viscosity of the WPVe series apparently decreases by the addition of CO_2. The H_2O content of 0.12wt% in the CO_2-free samples rises to 0.17 and 0.18 wt% for WPVe_1.1 and WPVe_1.2, respectively (see Table 2). It is well studied that H_2O reduces the viscosity of a melt as discussed below. Giordano et al. (2008) developed a model to predict the melt viscosity at given temperatures depending on melt composition including the H_2O concentration (subsequently denominated as GRD08). GRD08 is applied to the phonolitic WPVe series to estimate the effect of H_2O on the viscosity. Corresponding to GRD08, an addition of 0.05 and 0.06 wt% H_2O lowers the viscosity by approx. 0.4 $\log_{10}$ Pa s in the low temperature – high viscosity range as investigated in this study. For the WPVe_1.1 melt, the viscosity decrease determined by the micropenetration technique and the viscosity at T_g^{Onset} agree with each other and is approx. 0.4 $\log_{10}$ Pa s (Figs. 3A and 6). The viscosities of the WPVe_1.2 melt determined with the micropenetration method plots nearly on those for the WPVe_1.1 melt (Fig. 3A). Corresponding to GRD08, the viscosity drop for WPVe_1.1 and WPVe_1.2 results from the H_2O content wherefore the CO_2 influence appears to vanish. On the other hand, the viscosity difference at T_g^{Onset} (Fig. 6) is approx. 0.6 $\log_{10}$ Pa s for WPVe_1.2 contrasting to 0.4 $\log_{10}$ Pa s based on GRD08 indicating a combined viscosity reducing effect of both volatiles H_2O and CO_2. This influence of H_2O seems to be more pronounced at lower temperatures demonstrated by the comparison of the micropenetration viscosity data and the viscosity at T_g^{Onset} (Figs. 3A and 6).

All CO_2-free samples of the PN-0.5Fe series and PR-0.5Fe series contain microcrystals (Table 2), thus the viscosity of the pure liquid should be less than that measured (i.e. Einstein 1906;

Roscoe 1952; Vetere et al. 2010). Klein et al. (2018) established a model for the calculation of the relative viscosity η_{rel} of crystal-bearing melts considering crystal fraction, crystal volume and shape. By means of the model, the decrease in viscosities of the pure liquid for both series is up to 0.06 $\log_{10}$ Pa s for the maximum crystal fraction of 0.04 in this study, what is within the measurement error.

However, the CO_2-free melts of both series show differences in their H_2O concentrations (Table 2). As mentioned above, H_2O affects the viscosity noticeably. Previous studies pointed out a viscosity decreasing effect of H_2O that is larger in the low temperature – high viscosity range than in the high temperature – low viscosity range. This viscosity reducing effect decreases with increasing amounts of H_2O and is more pronounced for more polymerised melts than for less polymerised melts. At 700 °C and in the range of H_2O concentration as presented in this study for the PN-0.5Fe and PR-0.5Fe series, the drop in viscosity is approx. 0.1 $\log_{10}$ Pa s for a shoshonitic melt (Vetere et al. 2007) or up to approx. 0.4 $\log_{10}$ Pa s for melts of the Campi Flegrei (Misiti et al. 2011). Whittington et al. (2000) observed a viscosity decrease of 0.20 $\log_{10}$ Pa s for an anhydrous tephrite (0.01 wt% H_2O) by the addition of 0.12 wt% H_2O. Robert et al. (2013) observed a viscosity decrease of approx. 3 $\log_{10}$ Pa s from a “dry” (0.01 wt% H_2O) to a 0.56 wt% H_2O bearing basaltic andesite at 700 °C.

For the CO_2-free melts of the PN-0.5Fe series, the H_2O contents are approx. the same within the error (Table 2) resulting in similar viscosities (Fig. 3) differing at the very limit of the measurement error. Fig. 6 suggests a CO_2-driven viscosity drop for this series at T_g^{Onset}. Taking into account the strong viscosity reducing effect of H_2O, it is not clearly predictable how CO_2 affects these melts.

The differences in viscosity of the CO_2-bearing melts of the PR-0.5Fe series appear to be negligible at T_g^{Onset} (Fig. 6). As mentioned above, the foaming of the CO_2-bearing melts of the PR-0.5Fe series falsify the results of the calorimetric experiments and consequently, it is not possible to state the effect of the influence of CO_2 on this melt composition.

The viscosities of the CO_2-free melts of the PR-Leu-0.5Fe series agree with each other (Fig. 3C). As a consequence, an increased amount of 0.01 wt% H_2O (Table 2) has no detectable influence on the viscosity of this melt series. A further addition of approx. 0.02 wt% H_2O as found in the CO_2-bearing melts of the PR-Leu-0.5Fe series (Table 2) is assumed also to have a negligible (within the ± 0.06 $\log_{10}$ Pa s error in measurement) effect on viscosity (Table 2). The viscosities of the CO_2-bearing melts with different CO_2 concentrations are within the error of each other (Figs. 3C and 6). The presented data indicate a viscosity decreasing effect by the

addition of CO_2 as seen in Figs. 1B, 3C and 6. However, this apparent viscosity drop grazes the extreme end of the precision of the measurements.

Based on the presented data, CO_2 concentrations up to ~0.50 wt% result in a slight to negligible decrease in viscosity. The overall observed viscosity drop of the phonolitic, tephri-phonolitic and tephritic melts is mainly caused by their H_2O content with this decrease in viscosity increasing when the degree of polymerisation (γ) increases (Fig. 6).

Geological importance for the PR and PN eruptions

Kleest et al. (2020) showed that the viscosities of the volatile-free melts of the Pozzolane Rosse and Pozzolane Nere event are higher than expected. They also demonstrated a viscosity decrease for the PR melt caused by assimilation of carbonate wall rock due to an enrichment in Ca^{2+}, and an additional reduction in melt viscosity following leucite crystallisation.

Based on the results of the present study, an incorporation of small amounts of CO_2 do not affect the melt viscosity to a great extent. In contrast, even a small H_2O content in the melt results in a detectable decrease in viscosity and hence, is more effective.

During the storage of the parental PR and PN magmas, crystal formation reaches contents up to 60 vol% documented by pyroclastic products (Freda et al. 2011). Kleest et al. (2020) calculated a resulting viscosity increase up to two orders in magnitude for a leucite content of 56 vol% after a model from Caricchi et al. (2007). Additionally, carbonate assimilation reaches values of 15 wt% (Iacono-Marziano et al. 2007) which clearly exceeds the solubility of CO_2 in the PR melt (Schanofski et al. 2019). Consequently, the melt becomes oversaturated in CO_2 resulting in the formation of bubbles as recorded in scoria layers with a vesicularity up to 50% (Giordano et al. 2006). Trolese et al. (2017) found emplacement temperatures of ignimbrites from the PR and PN eruptions of approx. 710 °C and 600 - 630 °C, respectively, and inferred that magma fragmentation starts at temperatures being approx. 100 °C higher. Since these fragmentation temperatures are near the glass transition for the CO_2-free PR-0.5Fe and PN-0.5Fe melts, the magma on the top of the vent is highly viscous or nearly rigid due to the large crystal content. It is suggested, that a sudden release of bubbles as a consequence of carbonate assimilation or depressurisation in the subjacent less viscous magma forces the magma plug out of the vent leading to magma fragmentation during the eruption and results in a highly explosive eruptive style. Similar findings are discussed by Freda et al. (2011) and Marra et al. (2009) for the PR and PN event and by Cross et al. (2014) for the Albano Maar volcanism, postulating free CO_2 triggering explosive eruptions at the CAVD.

Conclusion

The presented study concerns the viscosities of CO_2-bearing phonolitic, tephri-phonolitic, tephritic and foiditic melt compositions. The carbon is incorporated as CO_3^{2-} in the melts. With the exception for the foiditic melt, for which no data are reliable, the viscosity apparently decreases with the addition of CO_2. However, this drop in viscosity is overshadowed by the decrease in viscosity caused by small H_2O concentrations in the melts. This effect is more pronounced in the more polymerised melts. Although it is difficult to separate the effect of H_2O and CO_2 on the viscosity of theses melts, it would appear that CO_2 results in a small to negligible decrease in viscosity at these high viscosity conditions.

Acknowledgements

The funding of this research is ensured by the Deutsche Forschungsgemeinschaft grant No. WE 1801/15-1. Special thanks go to Dr. Sara Fanara, Dr. Max Schanofski and Dr. Burkhard Schmidt for their support at the IHPV and the FTIR. For technical assistance, we wish to thank Bettina Schlieper-Ludewig for her help with the viscosity, calorimetry and colorimetric measurements and Marina Horstmann for her help at the carbon sulphur analyser. Furthermore, we wish to thank Dr. Andreas Kronz and Jochen Gätjen for their aid at the electron microprobe as well as Andre Petitjean for the tricky sample preparation. And a great thanks to an anonymous reviewer, to Kelly Russell and to Dante Canil for their very constructive recommendations.

References

Adam G and Gibbs JH (1965) On the Temperature Dependence of Coorperative Relaxation Properties in Glass-Forming Liquids. J Chem Phys 43:139-146

Angell CA, Yue Y, Wang L-M, Colpey JRD, Borick S, Mosa S (2003) Potential energy, relaxation, vibrational dynamics and boson peak, of hyperquenched glasses. J Phys: Condensed Matter 15:1051-1068

Behrens H, Misiti V, Freda C, Vetere F, Botcharnikov RE, Scarlato P (2009) Solubility of H_2O and CO_2 in ultrapotassic melts at 1200 and 1250 °C and pressure from 50 to 500 MPa. Am Mineral 94:105-120

Benne D and Behrens H (2003) Water solubility in haplobasaltic melts. Eur J Mineral 15:803-814

Bigg PH (1967) Density of water in SI units over the range 0-40 °C. Brit J Appl Phys 18:521

Blank JG and Brooker RA (1994) Experimental studies of carbon dioxide in silicate melts: solubility, speciation and stable carbon isotope behaviour. In: Carroll M R and Holloway J R (eds) Volatiles in Magmas, vol 30. Reviews in Mineralogy. Mineralogical Society of America, Washington, 157-186

Blythe LS, Deegan FM, Freda C, Jolis EM, Masotta M, Misiti V, Taddeucci J, Troll VR (2015) CO_2 bubble generation and migration during magma-carbonate interaction. Contrib Mineral Petrol 169:article 42

Boari E, Avanzinelli R, Melluso L, Giordano G, Mattei M, De Benedetti AA, Morra V, Conticelli S (2009) Isotope geochemistry (Sr-Nd-Pb) and petrogenesis of leucite-bearing volcanic rocks from "Colli Albani" volcano, Roman Magmatic Province, Central Italy: inferences on volcano evolution and magma genesis. Bull Volcanol 71:977-1005

Botcharnikov RE, Behrens H, Holtz F (2006) Solubility and speciation of C-O-H fluids on andesitic melt at T = 1100-1300°C and P = 200 and 500 MPa. Chem Geol 229:125-143

Bourgue E and Richet P (2001) The effects of dissolved CO_2 on the density and viscosity silicate melts: a preliminary study. Earth Planet Sci Lett 193:57-68

Brearley M and Montana A (1989) The effect of CO_2 on the viscosity of silicate liquids at high pressure. Geochim et Cosmochim Acta 53:2609-2616

Bruno PPG, Cippitelli G, Rapolla A (1998) Seismic study of the Mesozoic carbonate basement around Mt. Somma-Vesuvius, Italy. J Volcanol Geotherm Res 84:311-322

Campagnola S, Vona A, Giordano G (2016) Crystallization kinetics and rheology of leucite-bearing tephriphonolite magmas from the Colli Albani volcano (Italy). Chem Geol 424:12-29

Caricchi L, Burlini L, Ulmer P, Gerya T, Vassalli M, Papale P (2007) Non-Newtonian rheology of crystal-bearing magmas and implications for magma ascent dynamics. Earth Planet Sci Lett 264:402-419

Carichhi L, Sheldrake TE, Blundy J (2018) Modulation of magmatic processes by CO_2 flushing. Earth Planet Sci Lett 491:160-171

Chevrel MO, Platz T, Hauber E, Baratoux D, Lavallée Y, Dingwell DB (2013) Lava flow rheology: A comparison of morphological and petrological methods. Earth Planet Sci Lett 384:109-120

Cross JK, Tomlinson EL, Giordano G, Smith VC, De Benedetti AA, Roberge J, Manning CJ, Wulf S, Menzies MA (2014) High level triggers for explosive mafic volcanism: Albano Maar, Italy. Lithos 190-191:137-153

Einstein A (1906) Eine neue Bestimmung der Moleküldimensionen. Annals Phys 19:289-306

De Rita D, Faccenna C, Funiciello R, Rosa C, (1995) Stratigraphy and volcano-tectonics. The Volcano of the Alban Hills. In: Trigila, R. (Ed.), Università degli Studi di Roma "La Sapienza", Rome, Italy, pp. 33-71.

Di Genova D, Romano C, Alletti M, Misiti V, Scarlato P (2014) The effect of CO_2 and H_2O on Etna and Fondo Riccio (Phlegrean Fields) liquid viscosity, glass transition temperature and heat capacity. Chem Geol 377:72-86

Dingwell DB, Knoche R, Webb SL (1992) The effect of B_2O_3 on the viscosity of haplogranitic liquids. Am Mineral 77:457-461

Dingwell DB and Webb SL (1989) Structural Relaxation in Silicate Melts and Non-Newtonian Melt Rheology in Geological Processes. Phys Chem Minerals 16:508-516

Dixon JE and Pan V (1995) Determination of the molar absorptivity of dissolved carbonate in basanitic glass. Am Mineral 80:1339-1342

Fine G and Stolper E (1986) Dissolved carbon dioxide in basaltic glasses: concentration and speciation. Earth Planet Sci Lett 76:263-278

Freda C, Gaeta M, Giaccio B, Marra F, Palladino DM, Scarlat P, Sottili G (2011) CO_2-driven large mafic explosive eruptions: the Pozzolane Rosse case study from the Colli Albani Volcanic District (Italy). Bull Volcanol 73:241-256

Giordano G, De Benedetti AA, Diana A, Diano G, Gaudioso F, Marasco F, Miceli M, Mollo S, Cas RAF, Funiciello R (2006) The Colli Albani mafic caldera (Roma, Italy): Stratigraphy, structure and petrology. J Volcanol Geotherm Res 155:49-80

Giordano G and Dobran F (1994) Computer simulations of the Tuscolano Artemisio´s second pyroclastic flow unit (Alban Hills, Latium, Italy). J Volcanol Geotherm Res 61:69-94

Giordano D and Russell JK (2017) The heat capacity if hydrous multicomponent natural melts and glasses. Chem Geol 461:96-103

Giordano D, Russell JK, Dingwell DB (2008) Viscosity of magmatic liquids: A model. Earth Planet Sci Lett 271:123-134

Goff F, Love SP, Warren RG, Counce D, Obenholzer J, Siebe C, Schmidt SC (2001) Passive infrared remote sensing evidence for large, intermittent CO_2 emissions at Popocatépetl volcano, Mexico. Chem Geol 177:133-156

Iacono Marziano G, Schmidt BC, Dolfi D (2007) Equilibrium and disequilibrium degassing of a phonolitic melt (Vesuvius AD 79 “white pumice”) simulated by decompression experiments. J Volcanol Geotherm Res 161:151-164

Kleest C, Webb SL, Fanara S (2020) Rheology of melts from the Colli Albani Volcanic District (Italy): a case study. Contrib Mineral Petrol 175:82

Klein J, Mueller SP, Helo C, Schweitzer S, Gurioli L, Castr JM (2018) An expanded model and application of the combined effect of crystal-size distribution and crystal shape on the relative viscosity of magmas. J Volcanol Geotherm Res 357:128-133

Kolzenburg S, Di Genova D, Giordano D, Hess KU, Dingwell DB (2018) The effect of oxygen fugacity on the theological evolution of crystallizing basaltic melts. Earth Planet Sci Lett 487:21-32

Maier CG and Kelley KK (1932) An equation for the representation of high-temperature heat content data. J Am Chem Soc 54:3243-3246

Marra F, Karner DB, Freda C, Gaeta M, Renne P (2009) Large mafic eruptions on Alban Hills Volcanic District (Central Italy): Chronostratigraphy, petrography and eruptive behaviour. J Volcanol Geotherm Res 179:217-232

Martinez L-M & Angell CA, (2001) A thermodynamic connection to the fragility of glass-forming liquids. Nature 410:663-667

Misiti V, Vetere F, Freda C, Scarlato P, Behrens H, Mangiacarpa A, Dingwell DB (2011) A general viscosity model of Campi Flegrei (Italy) melts. Chem Geol 290:50-59

Morizet Y, Nichols ARL, Kohn SC, Brooker RA, Dingwell DB (2007) The influence of H_2O and CO_2 on the glass transition temperature: insights into the effect of volatiles on magma viscosity. Eur J Mineral 19:657-669

Nowak M, Porbatzki D, Spickenbom K, Diedrich O (2003) Carbon dioxide speciation in silicate melts: a restart. Earth Planet Sci Lett 207:131-139

Ohlhorst S, Behrens H, Holtz F (2001) Compositional dependence of molar absorptivities of near-infrared OH- and H_2O bands in rhyolitic to basaltic glasses. Chem Geol 174:5-20

Pocklington HC (1940) Rough measurement of high viscosities. Proc Cambridge Phil Soc 36:507-508

Richet P (1984) Viscosity and configurational entropy of silicate melts. Geochim et Cosmochim Acta 48:471-483

Robert G, Knipping JL, Scherbarth S, Robertson TE, Stechern A, Behrens H, Whittington AG (2015) Heat capacity and viscosity of basaltic melts with $H_2O \pm F \pm CO_2$. Chem Geol 418:51-65

Robert G, Whittigton AG, Stechern A, Behrens H (2013) The effect of water on the viscosity of a synthetic calc-alkaline basaltic andesite. Chem Geol 346:135-148

Robie RA, Hemingway BS, Fischer JR (1978) Thermodynamic properties of minerals and related substances at 298.15 K and 1 bar (10^5 Pa) pressure and higher temperatures. US Geol Surv Bull 1452:428-446

Roscoe R (1952) The viscosity of suspensions of rigid spheres. Br J Appl Phys 3:267-269

Russell JK and Giordano D (2017) Modelling configurational entropy of silicate melts. Chem Geol 461:140-151

Schanofski M, Fanara S, Schmidt BC (2019) CO_2-H_2O solubility in K-rich phonolitic and leucititic melts. Contrib Mineral Petrol 174:52

Schrötter H.W., Klöckner H.W. (1979) Raman Scattering Cross Sections in Gases and Liquids. In: Weber A. (eds) Raman Spectroscopy of Gases and Liquids. Topics in Current Physics, vol 11. Springer, Berlin, Heidelberg

Schuessler JA, Botcharnikov RE, Behrens H, Misiti V, Freda C (2008) Oxidation state of iron in hydrous phono-tephritic melts. Am Mineral 93:1493-1504

Seifert R, Malfait WJ, Lerch P, Sanchez-Valle C (2013) Partial molar volume and compressibility of dissolved CO_2 in glassese with magmatic compositions. Chem Geol 358:119-130

Shand SJ (1927) The Eruptive Rocks. Wiley, Mew York NY

Shishkina TA, Botcharnikov RE, Holtz F, Almeev RR, Jazwa AM, Jakubiak AA (2014) Compositional and pressure effects on the solubility of H_2O and CO_2 in mafic melts. Chem Geol 388:112-129

Stevenson RJ, Dingwell DB, Webb SL, Bagdassarov NS (1995) The equivalence of enthalpy and shear stress relaxation in rhyolitic obsidians and quantification of the liquid-glass transition in volcanic processes. J Volcanol Geotherm Res 68:297-306

Stolper E (1982) Water in Silicate Glasses: An Infrared Spectroscopic Study. Contrib Mineral Petrol 81:1-17

Taylor GI (1932) The viscosity of a fluid containing small drops of another fluid. Proc R Soc London A 138:41-48

Thibault Y and Holloway JR (1994) Solubility if CO_2 in a Ca-rich leucitie: effects of pressure, temperature and oxygen fugacity. Contrib Mineral Petrol 116:216-224

Tobolsky AV and Taylor RB (1963) Viscoelastic properties of a simple organic glass. J Phys Chem 67:2439-2442

Toplis MJ (1998) Energy barriers to viscous flow and the prediction of the glass transition temperatures of molten silicates. Am Mineral 83:480-490

Toplis MJ, Dingwell DB, Hess K-U, Lenci T (1997) Viscosity, fragility and configurational entropy of melts along the join SiO_2-$NaAlSiO_4$. Am Mineral 82:979-990

Trolese M, Giordano G, Cifelli F, Winkler A, Mattei M (2017) Forced transport of thermal energy in magmatic and phreatomagmatic large volume ignimbrites: Paleomagnetic evidence from the Colli Albani volcano, Italy. Earth Planet Sci Lett 478:179-191

Troll VR, Hilton DR, Jolis EM, Chadwick JP, Blythe LS, Deegan FM, Schwarzkopf LM, Zimmer M (2012) Crustal CO_2 liberation during the 2006 eruption and earthquake events at Merapi volcano, Indonesia. Geophys Res Lett 39:11

Vetere F, Behrens H, Holtz F, Vilardo G, Ventura G (2010) Viscosity of crystal-bearing melts and its implication for magma ascent. J Mineralogical and Petrological Sci 105:151-163

Vetere F, Behrens H, Misiti V. Ventura G, Holtz F, De Rosa R, Deubener J (2007) The viscosity of shoshonitic melts (Vulcanello Peninsula, Aeolian Islands, Italy): Insight on the magma ascent in dikes. Chem Geol 245:89-102

Webb SL (2005) Structure and rheology of iron-bearing Na_2O-Al_2O_3-SiO_2 melts. Eur J Mineral 17:223-232

Webb SL (2008) Configurational heat capacity of Na_2O-CaO-Al_2O_3-SiO_2 melts. Chem Geol 256:92-101

Webb SL (2011) Configurational heat capacity and viscosity of (Mg, Ca, Sr, Ba)-Al_2O_3-SiO_2 melts. Eur J Mineral 23:487-497

Webb SL, Banaszak M, Köhler U, Rausch S, Raschke G (2007) The viscosity of Na_2O-CaO-Al_2O_3-SiO_2 melts. Eur J Mineral 19:681-692

White B and Montana A (1990) The Effect of H_2O and CO_2 on the Viscosisty of Sanidin Liquid at High Pressures. J Geophys Res 95:683-693

Whittington A, Richet P, Holtz F (2000) Water and the viscosity of depolymerized aluminosilicate melts. Geochim et Cosmochim Acta 64:3725-3736

Wilson AD (1960) The Micro-determination of Ferrous Iron in Silicate Minerals by a Volumetric and a Colorimetric Method. Analyst 85:823-827

Appendix A

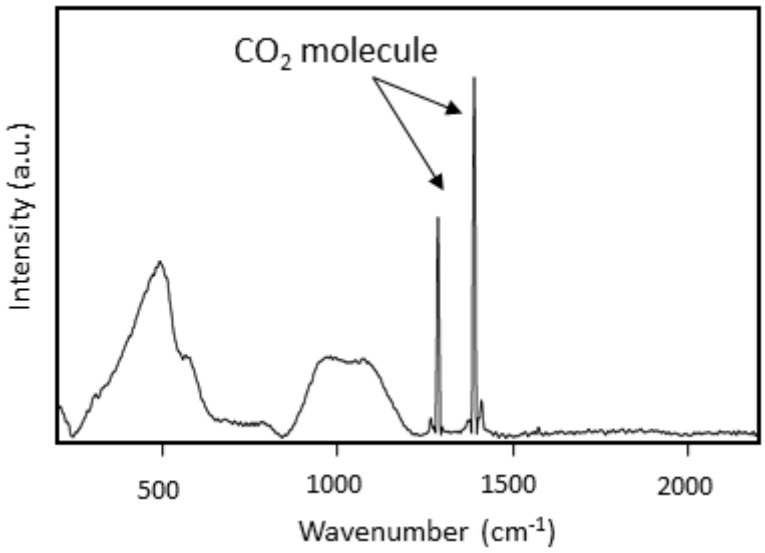

Fig. A1 Raman spectrum of a filled bubble from WPVe_1.1. The sharp peaks at 1286 and 1390 cm^{-1} are caused by molecular CO_2 indicating that the bubbles in the melts are filled with molecular CO_2.

Appendix B

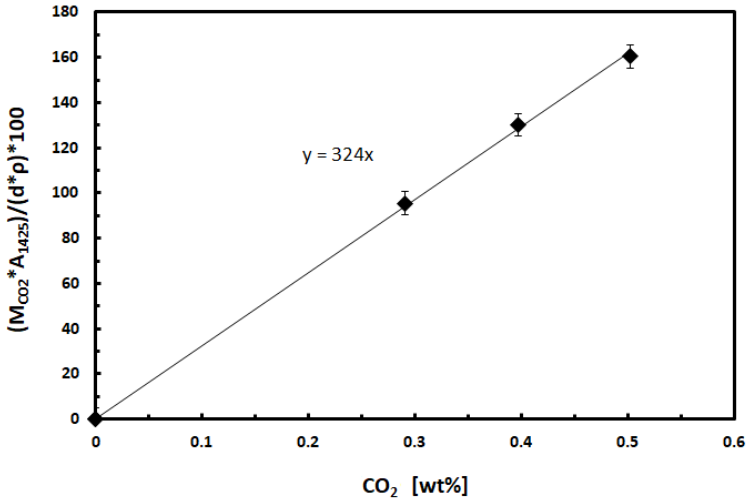

Fig. B1 Plot for the calibration of the absorption coefficient ε_{1425} for the PR-Leu-0.5Fe series. The CO_2-free spectrum of this series is subtracted from the CO_2-bearing ones. The absorbances of the CO_2-bearing melts are normalised by thickness and density and are plotted vs the total amount of CO_2 determined by the CS analysis. The slope of the regression line corresponds to ε_{1425} for this melt series.

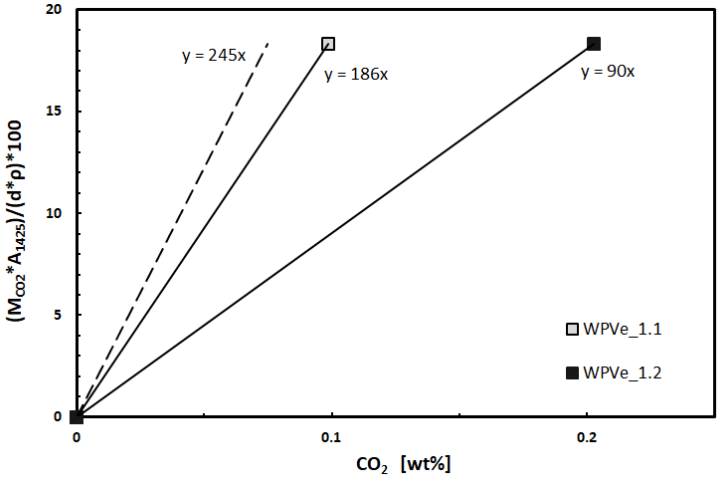

Fig. B2 Density and thickness normalised absorbance at 1425 cm^{-1} vs CO_2 concentration determined by the CS analysis for the CO_2-bearing melts WPVe_1.1 and WPVe_1.2 to calculate the absorption coefficient ε_{1425} for the WPVe series (continuous lines). Both samples contain bubbles filled with molecular CO_2 falsifying the value of ε_{1425}: the normalised absorbances of these samples are equal but have different amounts of total CO_2 measured by CS analysis what results in an underestimation of ε_{1425}. For comparison, the dashed line shows the theoretical line with ε_{1425} from Schanofski et al. (2019) who determined ε_{1425} for the same composition.

Appendix C

WPVe_0.1		WPVe_0.2		WPVe_1.1		WPVe_1.2		PN-0.5Fe_0.1		PN-0.5Fe_0.2		PR-0.5Fe_0.1	
T [°C]	$\log_{10}\eta$ [Pa s]	T [°C]	$\log_{10}\eta$ [Pa s]	T [°C]	$\log_{10}\eta$ [Pa s]	T [°C]	$\log_{10}\eta$ [Pa s]	T [°C]	$\log_{10}\eta$ [Pa s]	T [°C]	$\log_{10}\eta$ [Pa s]	T [°C]	$\log_{10}\eta$ [Pa s]
622.1	13.37	622.0	13.38	612.0	13.28	612.0	13.15	642.2	13.06	657.2	12.41	632.1	12.31
642.2	12.57	642.2	12.65	622.1	12.84	622.1	12.73	662.3	12.31	672.3	12.01	652.2	11.42
662.3	11.99	662.3	11.85	632.1	12.56	632.1	12.46	677.3	11.91	682.3	11.64	667.3	11.17
682.4	11.52	682.3	11.29	642.2	12.20	642.2	12.10	692.4	11.46	702.4	10.99	682.4	10.56
692.4	11.22	702.5	10.84	652.2	11.92	652.2	11.85	702.4	11.13	712.5	10.78	692.4	10.43
702.5	10.82	722.5	10.34	662.3	11.57	662.3	11.60	712.5	10.96	722.5	10.45	702.5	10.15
712.5	10.61	742.7	10.02	672.3	11.35	672.3	11.36	732.6	10.42	742.7	9.93	712.5	9.88
732.6	9.96	762.8	9.39	687.4	11.00	682.4	11.09	742.7	10.01	762.8	9.55	722.6	9.55
762.7	9.29	782.9	8.95	692.4	10.83	692.5	10.89	762.8	9.56	772.9	9.28	732.7	9.33
				702.5	10.59	702.5	10.62						

PR-0.5Fe_0.2		PR-Leu-0.5Fe_0.1		PR-Leu-0.5Fe_0.2		PR-Leu-0.5Fe_1.1		PR-Leu-0.5Fe_1.2		PR-Leu-0.5Fe_1.3	
T [°C]	$\log_{10}\eta$ [Pa s]	T [°C]	$\log_{10}\eta$ [Pa s]	T [°C]	$\log_{10}\eta$ [Pa s]	T [°C]	$\log_{10}\eta$ [Pa s]	T [°C]	$\log_{10}\eta$ [Pa s]	T [°C]	$\log_{10}\eta$ [Pa s]
622.3	12.45	612.0	13.20	612.0	12.98	602.0	13.38	602.3	13.28	602.3	13.38
652.2	11.60	622.1	12.78	627.1	12.45	622.1	12.51	612.4	12.94	612.4	12.82
667.3	10.86	632.1	12.34	642.2	11.74	632.5	11.92	622.4	12.45	632.5	11.89
672.3	10.75	642.2	11.80	652.2	11.30	642.2	11.48	632.5	11.90	642.5	11.35
682.4	10.62	652.2	11.34	662.3	10.84	652.6	11.11	642.5	11.50	652.6	11.07
692.4	10.30	662.3	10.82	672.4	10.41	662.3	10.68	652.6	10.99	662.6	10.63
702.5	10.04	672.4	10.42	682.4	10.08	672.4	10.24	672.7	10.11	672.7	10.19
712.5	9.84	682.4	10.01	692.4	9.69	682.4	9.87	682.6	9.85	682.7	9.80
722.6	9.57	692.4	9.65	702.5	9.32	692.4	9.51	692.8	9.38	692.8	9.42
		702.6	9.34	712.5	9.06	702.5	9.10	702.8	9.03	702.9	8.92
		712.6	8.96					712.9	8.68		

Table C1 Measured viscosity data of all melts (error = ± 0.06 $\log_{10}$ Pa s) at given temperature (error = ± 0.5 °C)

Appendix D

The parameters B_{VFT} and C_{VFT} of the Vogel-Fulcher-Tammann Equation (VFT Eq., Eq. 8) are listed in Table D1. The pre-coeffecient A_{VFT} is a constant and defines the viscosity at infinite temperature. For the presented calculation, A_{VFT} is assumed to be -4.00 $\log_{10}$ Pa s, since it is the same value for A_e in the Adam-Gibbs Equation (Eq. 11) and is discussed in the text and in more detail in Kleest et al. (2020). Forcing a curvature via the Vogel-Fulcher-Tammann Equation (Eq. 8) through the viscosity data in the narrow temperature range as investigated in this study results in VFT fragility (Eq. 9) being ~10% higher than that calculated using the Arrhenian equation (Eq. 5) as seen in Fig. D1. It is mentionable, that the more fragil a melt, the greater is the difference between the calculation of m via Eq. 5 and Eq. 8: the fragility of the melt WPVe_1.2 with the lowest value differ of 0.2 ($m_{Arrhenian}$ = 25.5 compared to m_{VFT} = 25.7) while the difference in fragility for the melt PR-Leu-0.5Fe_0.1 with the highest value is 3.2 ($m_{Arrhenian}$ = 41.2 compared to m_{VFT} = 44.4).

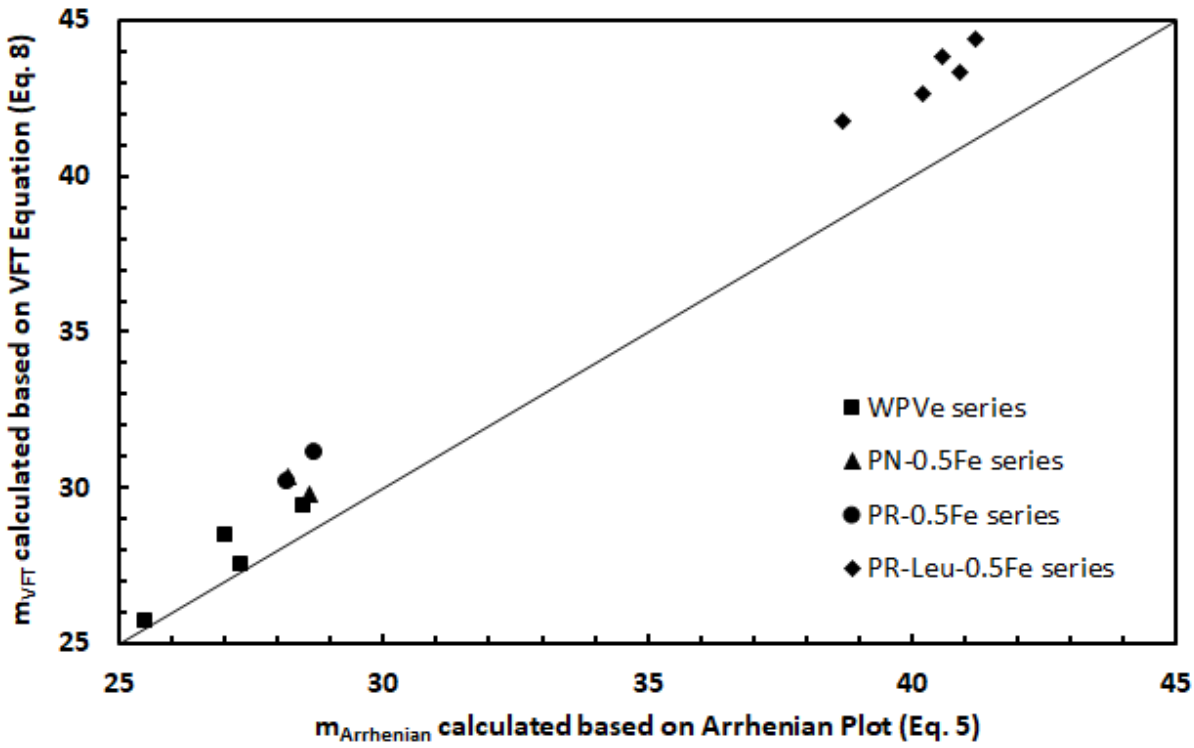

Fig. D1 Comparison of the fragilities calculated based on the Arrhenian plot (Eq. 5) and based on the VFT Equation (Eq. 8). The line represents exact agreement of the values.

	B_{VFT} [K]	C_{VFT} [K]	m_{VFT}
WPVe_0.1	8112.8 ± 198.5	428.5 ± 12.8	29.4
WPVe_0.2	8376.6 ± 191.6	411.2 ± 12.5	28.5
WPVe_1.1	8572.8 ± 132.8	387.2 ± 8.3	27.5
WPVe_1.2	9156.9 ± 156.2	348.9 ± 9.8	25.7
PN-0.5Fe_0.1	8123.6 ± 166.4	439.2 ± 10.8	29.8
PN-0.5Fe_0.2	7964.5 ± 117.4	445.9 ± 7.8	30.4
PR-0.5Fe_0.1	7531.1 ± 228.8	441.5 ± 15.5	31.1
PR-0.5Fe_0.2	7719.8 ± 266.9	425.9 ± 18.0	30.2
PR-Leu-0.5Fe_0.1	5224.9 ± 72.3	583.5 ± 4.7	44.4
PR-Leu-0.5Fe_0.2	5549.8 ± 403.7	561.0 ± 6.8	41.8
PR-Leu-0.5Fe_1.1	5402.0 ± 90.3	566.3 ± 5.9	42.6
PR-Leu-0.5Fe_1.2	5238.9 ± 93.4	575.4± 6.0	43.8
PR-Leu-0.5Fe_1.3	5298.6 ± 105.2	571.4 ± 6.8	43.3

Table D1 Fitted parameters B_{VFT} and C_{VFT} after the Vogel-Fulcher-Tammann Equation (Eq. 8) and the resulting fragility m_{VFT} after Eq. 9 for all investigated melts. The A_{VFT} constant is -4.00 $\log_{10}$ Pa s for all samples. For detailed discussion see text.

4 Influence of Fe^{2+}/Fe_{tot} on the viscosity of melts from the Colli Albani Volcanic District (Italy): foidite to phonolite

Preface

This 4th Chapter contains an article submitted on 29.10.2022 to "Contributions to Mineralogy and Petrology". To the date of the submission of this thesis, an answer with a decision about the article is not received.

This article is written by Christin Kleest and Prof. Dr. Sharon Webb and their contribution is shown in Fig. P1 and the corresponding author is Christin Kleest.

Author contribution:

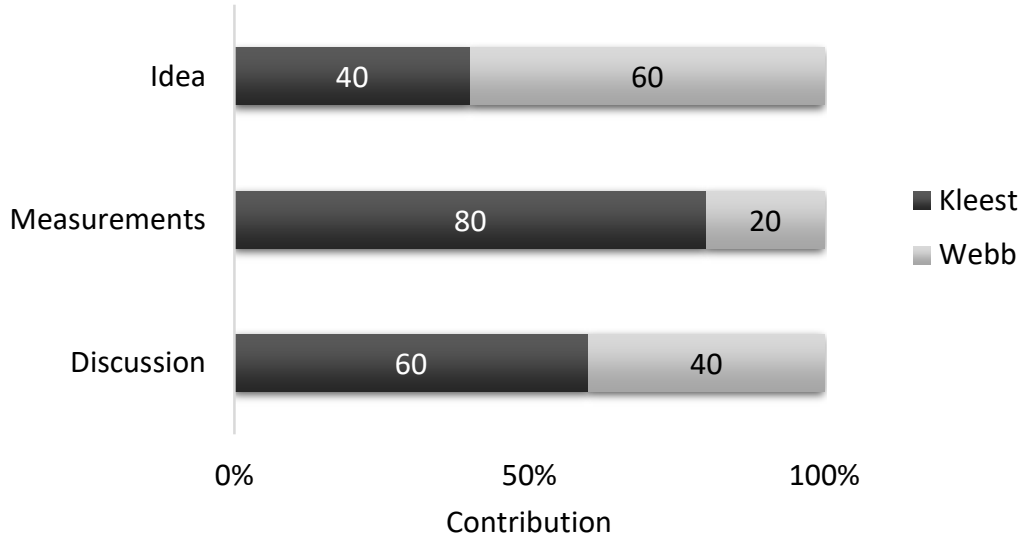

Fig. P1 Author contribution to the submitted scientific article of this 4th Chapter.

Abstract

Viscosity of a melt strongly depends on melt composition and the ratio of network modifiers to network former. In silicate melts, Fe exists as Fe^{2+} and Fe^{3+}, both affecting the viscosity in different manners: Fe^{2+} acts as a network modifier and lowers the viscosity whereas Fe^{3+} behaves as a network former and increases the viscosity. The Fe speciation strongly depends on the oxygen fugacity fO_2.

In this study, the viscosities of Fe-rich synthesised tephri-phonolitic, foiditic and tephritic melts from the Colli Albani Volcanic District (Italy) are investigated as a function of Fe^{2+}/Fe_{tot} in the glass transition range. Base glasses made in air at 1600 °C at $\log_{10} fO_2 = -0.68$ are re-equilibrated at $\log_{10} fO_2 = -4$ and -7 in a gas mixing furnace at mainly 1250 °C. Melts made in air and at $\log_{10} fO_2 = -4$ have nearly identical Fe^{2+}/Fe_{tot} due to the different experimental temperatures. T_g[12] of these melts drops by ~50 °C, ~30 °C and ~5 °C with an increase of Fe^{2+}/Fe_{tot} from ~0.45, ~0.39 and ~0.44 to ~0.76 for the tephri-phonolite, the foidite and the tephrite, respectively. These melts have H_2O concentrations up to 0.03 wt% and it is additionally shown that an increase up to 0.23 wt% H_2O overruns the viscosity reducing effect of the elevation in Fe^{2+}/Fe_{tot}. In addition, the viscosities of a phonolite from the Vesuvius are studied with Fe^{2+}/Fe_{tot} from ~0.41 to 0.87. In contrast to the other melts of this study, T_g[12] increases by 15 °C. However, this change in T_g[12] results from a depletion of ~14 mol% in Fe and network modifying alkali and alkaline-earth elements affecting the viscosity of this melt stronger than the increase in Fe^{2+}/Fe_{tot}.

Keywords: Viscosity, iron ratio, Colli Albani, glass transition, foidite, anhydrous melts

Introduction

The viscosity of a melt is the main property controlling magmatic processes like nucleation and forming of crystals and bubbles as well as the mass transfer in a melt and consequently the explosivity of an eruptive event. On the other hand, viscosity itself depends on composition, temperature, pressure and oxygen fugacity fO_2 (i.e. Webb et al 2007; Di Genova et al. 2014; Klein et al. 2018). In natural melts, there are multivalent components affecting viscosity. Among them, iron is the most abundant element existing as ferrous iron Fe^{2+} and ferric iron Fe^{3+} in silicate melts following the equilibrium reaction:

$$2FeO^{melt} + \frac{1}{2}O_2^{gas} \rightleftarrows Fe_2O_3^{melt} \quad (1)$$

(i.e. Kress and Carmichael 1991; Gaillard et al. 2003; Borisov et al. 2017). The iron speciation is strongly controlled by the oxygen fugacity fO_2 as a proxy for the activity of oxygen in a system and is given by the equilibrium:

$$\frac{1}{2}O_2 + 2e^- \rightleftarrows O^{2-} \quad (2)$$

(Ottonello et al. 2001). The free oxygen ion O^{2-} can be consumed or released to form metal oxides corresponding to Eq. 1. Previous studies observed an increasing Fe^{3+}/Fe_{tot} ratio and accordingly a decrease of Fe^{2+}/Fe_{tot} with increasing fO_2 for basaltic, andesitic and dacitic compositions (i.e. Cottrell and Kelley 2011; Dauphas et al. 2014; Kolzenburg et al. 2018). It is conventionally assumed that Fe^{3+} acts as a network former whereas Fe^{2+} is considered to be a network modifier in silicate melts. Consequently, the iron speciation affects the structure of a melt and the degree of polymerisation and hence its viscosity (i.e. Kress and Carmichael 1991; Liebske et al. 2003; Bouhifd et al. 2004; Knipping et al. 2015). Therefore, the knowledge of the Fe speciation in a silicate melt is important when regarding viscosity. Studies concerning the influence of the Fe ratio on viscosity exist and a few are presented here. Dingwell (1991) measured the viscosities of alkali- and alkaline-earth ferrosilicate liquids at high temperatures and observed a nonlinear decrease in viscosity at more reduced conditions accompanied with an increased Fe^{2+}/Fe_{tot}. Liebske et al. (2003) investigated the influence of the iron speciation on the viscosity of andesitic melts in the low temperature range and found a decrease in viscosity of ~1.6 $\log_{10}$ units with Fe^{2+}/Fe_{tot} increasing from 0.42 to 0.66 for 8.17 wt% FeO_{tot}. The viscosities of melts with iron- and alkali rich rhyolitic compositions studied by Stabile et al. (2016) and Di Genova et al. (2017) generally decrease with increasing Fe^{2+}/Fe_{tot} from 0.18 to 0.84 by ~0.7 $\log_{10}$ units or by ~0.5 $\log_{10}$ units with Fe^{2+}/Fe_{tot} increasing from 0.26 to 0.65 for 5.25 wt% FeO_{tot} and ~8 wt% FeO_{tot}, respectively. Kolzenburg et al. (2018) investigated basaltic and trachybasaltic melts that have been exposed to oxidised and reduced atmospheres. The viscosities of both compositions are higher at oxidised conditions with concomitant lower Fe^{2+}/Fe_{tot} with respect to the analogue melts produced at reduced conditions. A drop of Fe^{2+}/Fe_{tot} from 0.75 to 0.56 results in a viscosity increase of 0.04 – 0.07 $\log_{10}$ units for 12.01 wt% FeO_{tot} and a decrease in Fe^{2+}/Fe_{tot} from 0.63 to 0.39 increases the viscosity by 0.08 – 0.11 $\log_{10}$ units for 10.94 wt% FeO_{tot} for the basaltic and trachybasaltic composition, respectively.

Additionally, the decrease in viscosity with increasing Fe^{2+}/Fe_{tot} depends on the total Fe content in the melt.

Pyroclastic products of the Pozzolane Rosse event of the Colli Albani Volcanic District (CAVD) close to Rome (Italy) characterised by a silica-poor and K-rich composition rich in leucite have Fe contents up to nearly 10 wt% FeO_{tot} (Freda et al. 2011). Despite the silica undersaturation of the magma implying a low viscous lava flow, the eruptions are mostly highly explosive (Freda et al. 2011). Kleest et al (2020) showed that the viscosities of the Pozzolane Rosse composition (PR) and Pozzolane Nere composition (PN) of the CAVD are not that low as expected due to their enrichment in Ca^{2+} as a result of magma contamination caused by the assimilation of the carbonate wall rock (i.e. Iacono-Marziano et al. 2007a; Gaeta et al. 2009; Freda et al. 2011). The fO_2 for differentiated magmas of the youngest eruption cycle of the CAVD range from Ni-NiO to magnetite-haematite buffer (Freda et al. 2006).

In this study, the viscosities of synthetic equivalents of the PR and PN melts with different Fe ratios are investigated in the glass transition range. Original compositions are taken from Freda et al. (2011) and Campagnola et al. (2016), respectively, and a further composition by subtracting 4 mol% $KAlSi_2O_6$ from the PR melt is synthesised to study the residual PR melt after leucite crystallisation. All melts are made with the half amount of Fe to avoid crystallisation effects during measurements where Fe^{2+} is replaced by Mg^{2+} and Fe^{3+} by Al^{3+}. The studied melt compositions of the CAVD span from the tephri-phonolitic PN-0.5Fe series to a tephritic PR-Leu-0.5Fe series and finally to the foiditic PR-0.5Fe series. To represent the potassic end member of the Italian volcanism, the viscosity of a fourth synthetic equivalent of the phonolitic “white pumice” from the Vesuvius AD 79 eruption (WPVe series) after Iacona-Marziano et al. (2007b) is investigated. All melts are re-equilibrated at $fO_2 = 10^{-4.00}$ and $10^{-7.00}$ bar corresponding to approx. NNO+3 and NNO at 1250 °C, respectively, involving an increase in Fe^{2+}/Fe_{tot} with decreasing fO_2.

Methods

Starting materials and sample preparation

The base glasses WPVe, PN-0.5Fe and PR-0.5Fe are taken from Kleest et al. (2020) and the basic PR-Leu-0.5Fe melt is from Kleest and Webb (2021). These melts are made of previously dried powdered metal oxides and carbonates. This mixture was decarbonated at 1000 °C overnight and subsequently melted two times for 1h and finally for 4h in air ($\log_{10} fO_2 = -0.68$) at 1600 °C. For homogeneity, the melts are crushed and ground and mixed for 20 min between

the melting steps. Further experiments are done in a vertical gas mixing furnace with hydrogen H_2 and carbon dioxide CO_2 determining fO_2 at one total atmospheric pressure with $\log_{10} fO_2$ = -4 and $\log_{10} fO_2$ = -7 corresponding to approx. NNO+3 and NNO at 1250 °C, respectively. The H_2/CO_2 ratio for the fO_2 are taken from Deines et al. (1974). For the runs in the gas mixing furnace, the wire loop method of wrapping the sample with a platinum Pt wire is used. The Pt loop is pre-saturated in iron with a Fe-rich melt at the experimental conditions to avoid iron loss of the studied melt during the experiments. Previous investigations using a gas mixing furnace as used in the present study found the iron redox equilibrated after 8 hours at temperatures from 1275 °C to 1460 °C (Presnall and Brenner 1974; Kress and Carmichael 1988). To ensure complete redox equilibrium, all runs in the H_2/CO_2 furnace with $\log_{10} fO_2$ = -4 at 1250°C held for 20 hours. The experiments performed at $\log_{10} fO_2$ = -7 in the gas mixing furnace are also done for 20 hours at 1250°C for the PN-0.5Fe_NNO, PR-0.5Fe_NNO and PR-Leu-0.5Fe_NNO melts. Since the iron equilibrium for the WPVe_NNO sample is not reached under these conditions, this melt is synthesised at 1350°C for 120 hours at $\log_{10} fO_2$ = -7. All samples are quenched rapidly by dropping them down from the hot part of the furnace into water at ambient temperature. The re-equilibrated Fe ratio within the melt was determined for the inner and outer part of the sample and was found to be equal after the experimental runs.

Density

The determination of the density is based on the Archimedes´ Principle. The sample is weighted 10 times in air and in distilled water with a wetting agent that reduces the surface tension of water with a Mettler Toledo Excellence XP/XS analyse balance and is calculated by:

$$\rho = \frac{A}{A-B} * \rho_{H_2O} \quad (3)$$

with A – sample weight in air, B – sample weight in distilled water and ρ_{H_2O} – water density at ambient temperature after Bigg (1967).

Fourier transform infrared spectroscopy (FTIR)

FTIR measurements are performed with a Bruker Hyperion 3000 IR microscope, coupled with Bruker Vertex 70 FTIR spectrometer. For the determination on the H_2O concentrations, spectra are collected in the near-infrared range (NIR) from 2000 – 6000 cm^{-1} with a MCT detector cooled by liquid N_2, a W lamp and a CaF_2 beam splitter. Each spectrum consists of 100 scans

with a spatial resolution of 4 cm^{-1} and a spot size of 50 x 50 µm. The samples have parallel faces, are double polished and have a thickness of 200 – 300 µm.

Colorimetric micro-determination of the iron speciation

Wilson (1960) first developed this method for the determination of the iron speciation in silicate glasses that was modified by Schuessler et al. (2008). Approx. 6 – 16 mg powdered sample is dissolved in hydrofluoric acid HF. In solution, Fe^{2+} forms a reddish Fe(II)-bipyridyl-complex with the added 2:2´bipyridyl. In the UV/VIS spectroscopy, the reddish Fe(II)-bipyridyl-complex has an intensive absorption band at ~523 nm. This band is used for the determination of the Fe^{2+} content. Afterwards, Fe^{3+} is reduced to Fe^{2+} by hydroxylamine hydrochloride H_4NOCl to determine the total iron concentration. The iron ratio Fe^{2+}/Fe_{tot} is directly given by the ratio of the absorbances at ~523 nm. The UV/VIS measurements are performed with a AvaSpec-UV/VIS/NIR spectrometer and the software AvaSoft Version 8.3 from Avantes.

Viscometry

For viscosity measurements, the micropenetration technique is used with a Netzsch TMA 402 dilatometer. Samples are double polished with parallel faces. The base PR-Leu-0.5Fe melt has a thickness of 3 mm and a 2mm diameter spherical single sapphire crystal is used as the indenter. The melts that are re-equilibrated in the gas mixing furnace in more reduced atmospheres have thicknesses of 1.5 mm and the penetrating spherical single sapphire crystal is 1 mm in diameter. The measured viscosities range from $10^{8.54}$ Pa s to $10^{13.51}$ Pa s and are measured at temperatures from 620 to 800 °C in air for durations of 30 min up to 12 hours with applied forces of 0.05 to 10 N depending upon the melt viscosity. The viscosity is calculated from the penetration rate of the sapphire into the sample by:

$$\eta = \frac{0.1875\, Ft}{r^{0.5} l^{1.5}} \quad (4)$$

with F – the applied force, t – time, r – radius of the indent sphere, l – distance of indent (Pocklington 1940; Tobolsky and Taylor 1963; Dingwell et al. 1992). The temperature of the dilatometer is calibrated with the melting points of Bi (268.02 °C), Zn (417.02 °C), Al (659.02 °C), NaCl (800.05 °C) and Ag (951.09 °C) and the DDG1, a Na_2O-CaO-SiO_2 float glass from the Deutsche Glastechnische Gesellschaft, is used for standard measurements to get the precision of the dilatometer. The total error of the viscosity measurements is ± 0.06 $\log_{10}$ Pa s (1σ).

Results

Experimental conditions of the base glasses synthesised in air with WPVe, PN-0.5Fe and PR-0.5Fe from Kleest et al. (2020) as well as PR-Leu-0.5Fe from Kleest and Webb (2021) and the runs in the H_2/CO_2 gas mixing furnace are given in Table 1.

The chemical compositions of all base glasses analysed by the electron microprobe and the calculated chemical compositions of all melts are shown in Table 2 together with Fe^{2+}/Fe_{tot} determined by the colorimetric micro-determination and the resulting γ. γ is defined as (Na_2O + K_2O + CaO + MgO +FeO)/(Na_2O + K_2O + CaO + MgO + FeO + Al_2O_3 + Fe_2O_3) (Toplis et al. 1997; Webb et al. 2007) and represents the degree of polymerisation and consequently the structure of a melt. Within each series, Fe^{2+}/Fe_{tot} of the melts equilibrated in air and at $\log_{10} fO_2$ = -4 are nearly the same within the error due to the higher temperatures at which the samples in air are synthesised (Table 1). Fe^{2+}/Fe_{tot} of PR-Leu-0.5Fe and PR-Leu-0.5Fe_NNO+3 differ slightly, however, this does not influence γ and hence the melt structure (Table 2). Kress and Carmichael (1991) developed a model for the prediction of the Fe ratio as a function of melt composition, fO_2, temperature and pressure. Fig. 1 gives a comparison of Fe^{2+}/Fe_{tot} calculated by this model and the measured one with the colorimetric micro-determination.

It is seen that the model of Kress and Carmichael (1991) fits the Fe ratio of the investigated melts well. Fe^{2+}/Fe_{tot} for the CAVD melts equilibrated at $\log_{10} fO_2$ = -4 and -7 increases from 0.45 to 0.77 for the PN-0.5Fe series, from 0.39 to 0.75 for the PR-0.5Fe series and from 0.44 to 0.76 for the PR-Leu-0.5Fe series. This increase of the amount of the network modifying Fe^{2+} results in a decreased polymerisation of the melt structure which is shown by the 0.03 increase in γ for the PN-0.5Fe and PR-0.5Fe melts as well as an increase of 0.02 in γ for the PR-Leu-0.5Fe series. Contrary to the equivalents of the CAVD, the structure of the WPVe_NNO becomes more polymerised while Fe^{2+}/Fe_{tot} increases from ~0.40 to 0.87 (Table 2).

	$\log_{10} fO_2$ [bar]	T [°C]	t [h]	c(H_2O) [wt%]	ρ [g cm^{-3}]	comments
WPVe[1]	-0.68	1600	2x 1h and 1x 4h[1]	0.02 ± < 0.01[3]	2.48 ± 0.01	
WPVe_NNO+3	-4.00	1250	20	< 0.01 ± < 0.01[3]	2.48 ± 0.02	
WPVe_NNO	-7.00	1350	120	0.04 ± < 0.01[3]	2.45 ± 0.01	
PN-0.5Fe[1]	-0.68	1600	2x 1h and 1x 4h[1]	0.01 ± < 0.01[4]	2.58 ± 0.01	
PN-0.5Fe_NNO+3	-4.00	1250	20	0.01 ± < 0.01[4]	2.60 ± 0.03	crystals ~ 2vol%
PN-0.5Fe_ NNO	-7.00	1250	20	0.03 ± < 0.01[4]	2.61 ± 0.02	
PR-0.5Fe[1]	-0.68	1600	2x 1h and 1x 4h[1]	0.01 ± < 0.01[3]	2.70 ± 0.01	
PR-0.5Fe_ NNO+3	-4.00	1250	20	< 0.01 ± < 0.01[3]	2.70 ± 0.01	crystals < 1vol%
PR-0.5Fe_ NNO	-7.00	1250	20	0.01 ± < 0.01[3]	2.71 ± 0.01	
PR-Leu-0.5Fe[2]	-0.68	1600	2x 1h and 1x 4h[2]	0.01 ± < 0.01[4]	2.72 ± 0.01	
PR-Leu-0.5Fe_ NNO+3	-4.00	1250	20	0.01 ± 0.01[4]	2.78 ± 0.02	
PR-Leu-0.5Fe_ NNO	-7.00	1250	20	0.02 ± < 0.01[4]	2.74 ± 0.01	

[1] Between the melting steps, the glasses are ground for 20 min (Kleest et al. 2020)
[2] Between the melting steps, the glass is ground for 20 min (Kleest and Webb 2021)
[3] ε_{3550} = 67.0 ± 6.7 l*$mol^{-1}cm^{-1}$ (Stolper 1982)
[4] ε_{3550} = 63.9 ± 5.4 l*$mol^{-1}cm^{-1}$ (Behrens et al. 2009)

Table 1 Experimental conditions of the synthesis of the investigated melts: $\log_{10} fO_2$, temperature T, duration of the run as well as H_2O concentrations c(H_2O) determined by the FTIR and densities ρ for the melts. Errors of ρ and c(H_2O) are 1σ. All melts are made at 1 atm. The crystals in the melts of the PN-0.5Fe_NNO+3 and PR-0.5Fe_NNO+3 have grain sizes ranging from 7 to 20 µm and 3 to 7 µm, respectively, and a mean aspect ratio (= major axes/minor axes) of 1.30.

Electron microprobe analysis											
[wt %]	**SiO_2**	**Al_2O_3**	**Na_2O**	**TiO_2**	**FeO_{tot}**		**MnO**	**MgO**	**CaO**	**K_2O**	**total**
WPVe series[1]	55.91±0.16	21.47±0.10	5.29±0.07	0.30±0.03	2.72±0.05		0.13±0.02	0.41±0.01	3.25±0.05	9.48±0.08	98.96
PN-0.5Fe series[1]	50.01±0.16	22.41±0.10	2.50±0.06	0.63±0.02	5.82±0.08		0.19±0.02	3.25±0.03	5.47±0.06	8.92±0.08	99.20
PR-0.5Fe series[1]	43.30±0.15	19.84±0.10	3.04±0.06	0.92±0.04	7.46±0.09		0.20±0.02	5.44±0.04	10.55±0.09	8.47±0.08	99.22
PR-Leu-0.5Fe series[2]	45.20±0.16	18.65±0.10	3.68±0.06	1.14±0.03	5.88±0.08		0.25±0.02	6.16±0.06	13.05±0.09	4.77±0.06	98.78
Calculated compositions											
[mol %]	**SiO_2**	**Al_2O_3**	**Na_2O**	**TiO_2**	**FeO**	**Fe_2O_3**	**MnO**	**MgO**	**CaO**	**K_2O**	**Fe^{2+}/Fe_{tot}**	**γ [a]**
WPVe[1]	65.18±0.32	14.75±0.12	5.98±0.16	0.26±0.05	1.11±0.07	0.77±0.01	0.12±0.03	0.71±0.03	4.06±0.11	7.05±0.10	0.42±0.02	0.55
WPVe_NNO+3	65.11±0.40	14.75±0.14	5.99±0.20	0.24±0.02	1.08±0.02	0.81±0.02	0.16±0.02	0.73±0.01	4.07±0.07	7.05±0.12	0.40±0.02	0.55
WPVe_NNO[3]	67.99±0.44	15.25±0.16	4.35±0.17	0.26±0.02	1.10±0.02	0.08±0.01	0.11±0.02	0.65±0.01	3.81±0.07	6.40±0.11	0.87±0.08	0.51
PN-0.5Fe[1]	58.03±0.32	15.33±0.12	2.81±0.15	0.55±0.03	2.49±0.05	1.58±0.02	0.18±0.05	5.62±0.06	6.80±0.11	6.61±0.10	0.44±0.03	0.59
PN-0.5Fe_NNO+3	58.01±0.31	15.32±0.12	2.81±0.09	0.55±0.04	2.54±0.05	1.55±0.04	0.18±0.03	5.61±0.09	6.80±0.13	6.60±0.10	0.45±0.01	0.59
PN-0.5Fe_NNO	57.49±0.30	15.19±0.11	2.79±0.09	0.55±0.04	4.31±0.10	0.64±0.01	0.18±0.03	5.56±0.09	6.74±0.12	6.54±0.10	0.77±0.02	0.62
PR-0.5Fe[1]	49.29±0.31	13.31±0.12	3.35±0.09	0.79±0.04	2.56±0.05	2.27±0.04	0.19±0.03	9.23±0.09	12.86±0.13	6.15±0.10	0.36±0.03	0.69
PR-0.5Fe_NNO+3	49.24±0.26	13.30±0.10	3.35±0.10	0.78±0.05	2.77±0.04	2.16±0.04	0.19±0.03	9.22±0.10	12.85±0.17	6.14±0.09	0.39±0.01	0.69
PR-0.5Fe_NNO	48.61±0.26	13.13±0.10	3.31±0.10	0.77±0.05	5.25±0.10	0.88±0.01	0.19±0.03	9.11±0.10	12.69±0.17	6.07±0.09	0.75±0.02	0.72
PR-Leu-0.5Fe	49.97±0.22	12.15±0.10	3.94±0.10	0.94±0.05	2.12±0.04	1.66±0.04	0.24±0.03	10.16±0.10	15.45±0.17	3.36±0.09	0.39±0.02	0.72
PR-Leu-0.5Fe_NNO+3	49.91±0.27	12.13±0.10	3.94±0.10	0.94±0.04	2.39±0.04	1.52±0.03	0.23±0.03	10.14±0.15	15.43±0.16	3.36±0.06	0.44±0.01	0.72
PR-Leu-0.5Fe_NNO	49.48±0.27	12.03±0.10	3.91±0.10	0.94±0.04	4.09±0.08	0.65±0.01	0.23±0.03	10.05±0.15	15.30±0.16	3.33±0.06	0.76±0.02	0.74

[1] Reference: Kleest et al. (2020) [2] Reference: Kleest and Webb (2021)

[3] Calculated with atomic data from the µ-RFA corrected by means of a type calibration based on the analysis of approx. 50 glasses of known composition (in house standards)

[a] $\gamma = \frac{Na_2O+K_2O+CaO+MgO+FeO}{Na_2O+K_2O+CaO+MgO+FeO+Al_2O_3+Fe_2O_3}$

Table 2 Chemical compositions of the base glasses in wt% are determined by the electron microprobe analysis from Kleest et al. (2020) and Kleest and Webb (2021) with standard deviation of 1σ. Compositions in mol% are calculated on the basis of atomic data after the determination of the Fe ratio Fe^{2+}/Fe_{tot} via the colorimetric micro-determination with standard deviation of 1σ. Additionally, γ as an indicator of the degree of polymerisation is shown.

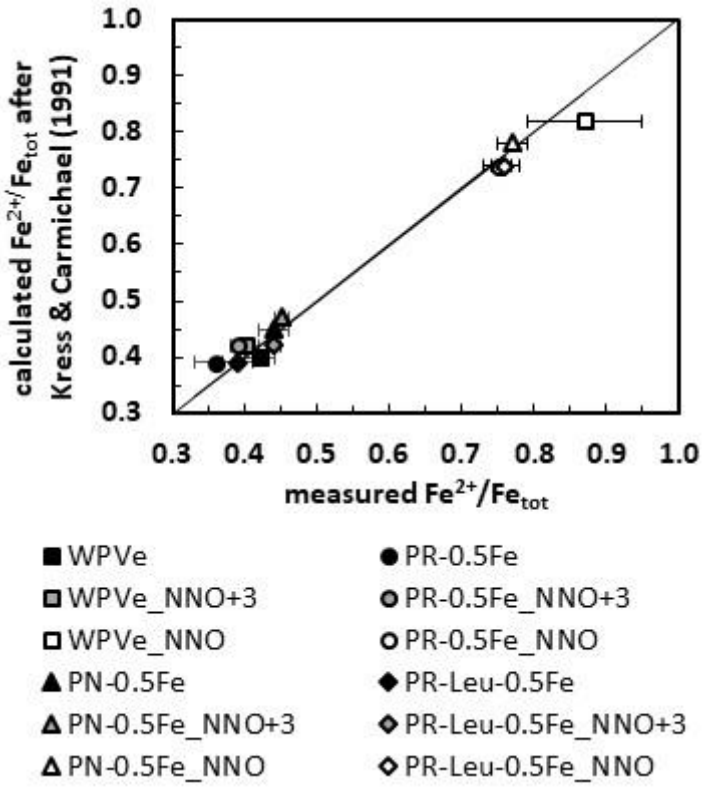

Fig. 1 Calculated Fe^{2+}/Fe_{tot} after Kress and Carmichael (1991) vs measured Fe^{2+}/Fe_{tot} with the 1:1 line for the melts of this study and the melts of the investigated series from Kleest et al. (2020)

Although the wire loop was Fe-saturated before the experimental run in the gas mixing furnace, the WPVe_NNO sample lost ~50% of its original iron content. Moreover, this melt lost ~14 mol% alkali and alkaline-earth elements and this overall loss in network modifying components leads to the observed increase in the degree of polymerisation with γ reduced from 0.55 to 0.51. All melts are free of crystals and bubbles with the exception of the melts PN-0.5Fe_NNO+3 and PR-0.5Fe_NNO+3 containing ~2 vol% and < 1 vol% crystals with grain sizes from 7 - 20 µm and 3 - 7 µm, respectively, and a mean aspect ratio (= major axes/minor axes) of 1.30.

Density

The densities ρ of the glasses at room temperature are shown in Fig. 2 and listed in Table 1. The lowest density glasses are those from the WPVe series (ρ = 2.45 – 2.48 g cm^{-3}), followed by the PN-0.5Fe series (ρ = 2.58 – 2.61 g cm^{-3}), the PR-0.5Fe series (ρ = 2.70 – 2.71 g cm^{-3}) and the PR-Leu-0.5Fe series (ρ = 2.72 – 2.78 g cm^{-3}). The densities of the PR-Leu-0.5Fe glasses differ slightly with various Fe^{2+}/Fe_{tot} without noticeable trend. However, altogether, there are no significant changes in the density as function of Fe^{2+}/Fe_{tot}.

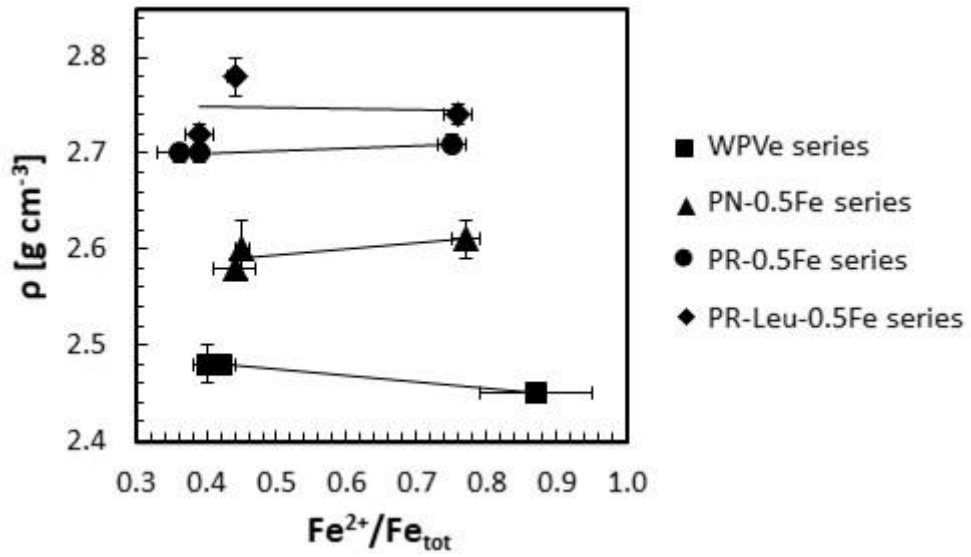

Fig. 2 Measured densities of the melts of this study and those from the study from Kleest et al. (2020) as a function of Fe^{2+}/Fe_{tot}

FTIR spectroscopy

The Lambert-Beer-law describes the relation between the concentration of a species and the absorbance of the IR spectrum:

$$c_i = \frac{M_i * A_j}{d * \rho * \varepsilon_j} * 100 \quad (5)$$

with c_i – concentration of the species *i* in wt%, M_i – molar mass of the species *i*, A_j – peak height of the absorbance of the band *j*, *d* – thickness of the sample in cm, ρ – density of the sample in g l^{-1}, ε – absorption coefficient in l mol^{-1} cm^{-1} (i.e. Stolper 1982; Thibault and Holloway 1994; Behrens et al. 2009).

For the investigation of the H_2O concentration, the absorbance at ~3550 cm^{-1} representing the fundamental OH stretching vibration is used (i.e. Stolper 1982; Ohlhorst et al. 2001; Behrens et al. 2009). The peak height is determined by subtracting a two-tangent baseline. The absorption coefficient ε_{3550} strongly depends on the chemical composition and is taken from previous studies: it is 67.0 ± 6.7 l mol^{-1} cm^{-1} for the phonolitic WPVe and foiditic PR-0.5Fe melt series (Stolper 1982) and 63.9 ± 5.4 l mol^{-1} cm^{-1} for the tephri-phonolitic PN-0.5Fe and tephritic PR-Leu-0.5Fe melt series (Behrens et al. 2009). Absorbances at 5200 cm^{-1} indicating the presence of H_2O molecules are not found in the spectra. Hence, H_2O is dissolved as OH^- only which is in agreement with previous studies that found H_2O to be dissolved as OH^- only

for total c(H_2O) < 0.5 wt% (i.e. Stolper 1982; Behrens et al. 2009; Schanofski et al. 2019). The melts of this study contain up to 0.04 wt% H_2O and are listed in Table 1.

Viscosity

The viscosity data of PR-Leu-0.5Fe and those of the investigated melts equilibrated at $\log_{10} fO_2$ = -4 and -7 are given in Table 3.

The Arrhenius equation

$$log_{10}\,\eta = A + \frac{B*10^4}{T} \quad (6)$$

with η – viscosity in Pa s, A and B as – fit parameters and T – temperature in Kelvin, is the best fit for the viscosity data in the studied temperature range and parameters are given in Table 4. Measured viscosities are displayed in Fig. 3 and data from Kleest et al. (2020) for the WPVe, PN-0.5Fe and PR-0.5Fe samples melted in air atmosphere are also shown. Fig. 3A shows the viscosities of the WPVe series. At 700 °C, the melt WPVe_NNO has the highest viscosity of 12.55 $\log_{10}$ Pa s, followed by WPVe_NNO+3 with a viscosity of 12.20 $\log_{10}$ Pa s and the WPVe has the lowest one with 12.01 $\log_{10}$ Pa s.

PN-0.5Fe_NNO+3 contains ~2 vol% crystals. The viscosity increasing effect of crystals in a melt is well studied (i.e. Einstein 1906; Roscoe 1952; Klein et al. 2018). After the model of Klein et al. (2018), calculating the relative viscosity as a function of crystallinity of a melt and the shape and the size of crystals, this crystal content increases the viscosity by < 0.03 $\log_{10}$ Pa s which is within the error of measurement and therefore not further discussed. PN-0.5Fe, PN-0.5Fe_NNO+3 and PN-0.5Fe_NNO have viscosities of 13.18, 12.27 and 11.15 $\log_{10}$ Pa s, respectively, at 700 °C (Fig. 3B).

PR-0.5Fe_NNO+3 has a crystal content of < 1 vol% increasing the viscosity negligibly by < 0.01 $\log_{10}$ Pa s after the model from Klein et al. (2018). The viscosities of the PR-0.5Fe series are shown in Fig. 3C: at 700 °C, PR-0.5Fe has a viscosity of 11.80 $\log_{10}$ Pa s, the viscosity of PR-0.5Fe_NNO+3 is 11.10 $\log_{10}$ Pa s and PR-0.5Fe_NNO is lowest at 10.39 $\log_{10}$ Pa s. Fig. 3D demonstrates the viscosities of PR-Leu-0.5Fe, PR-Leu-0.5Fe_NNO+3 and PR-Leu-0.5Fe_NNO with viscosities of 10.61, 10.33 and 10.18 $\log_{10}$ Pa s at 700 °C, respectively. With the exception of the WPVe series, a viscosity reducing trend is observed with a distinctly increased Fe^{2+}/Fe_{tot}.

WPVe_NNO+3		WPVe_NNO		PN-0.5Fe_NNO+3		PN-0.5Fe_NNO	
T [°C]	$\log_{10}\eta$ [Pa s]	T [°C]	$\log_{10}\eta$ [Pa s]	T [°C]	$\log_{10}\eta$ [Pa s]	T [°C]	$\log_{10}\eta$ [Pa s]
662.3	13.30	682.4	13.12	682.3	12.71	642.2	13.27
682.3	12.73	702.5	12.42	702.4	12.24	652.2	12.90
702.4	12.21	712.5	12.19	722.5	11.77	662.3	12.45
722.5	11.59	722.5	11.91	742.6	11.33	677.3	12.01
747.6	10.94	742.6	11.35	752.7	10.80	682.4	11.78
762.7	10.35	752.7	11.16	762.7	10.34	692.4	11.42
782.8	9.39	767.7	10.81	782.8	10.15	702.4	11.04
802.7	9.46	772.8	10.48	802.9	9.81	712.5	10.74
		792.9	10.10			717.5	10.52
						727.6	10.21
						737.6	9.94

PR-0.5Fe_NNO+3		PR-0.5Fe_NNO		PR-Leu-0.5Fe		PR-Leu-0.5Fe_NNO+3		PR-Leu-0.5Fe_NNO	
T [°C]	$\log_{10}\eta$ [Pa s]	T [°C]	$\log_{10}\eta$ [Pa s]	T [°C]	$\log_{10}\eta$ [Pa s]	T [°C]	$\log_{10}\eta$ [Pa s]	T [°C]	$\log_{10}\eta$ [Pa s]
662.3	12.14	622.1	13.29	643.2	13.21	632.1	13.51	622.1	13.34
682.3	11.62	632.1	12.64	652.9	12.81	642.2	12.84	652.2	12.51
692.4	11.30	652.2	12.01	663.3	12.06	662.2	11.84	662.3	11.92
712.5	10.92	662.3	11.81	673.3	11.72	672.3	11.68	672.3	11.56
732.6	10.28	672.3	11.50	683.4	11.34	682.3	11.10	682.4	10.89
752.7	9.61	692.4	10.66	693.1	10.83	692.4	10.69	692.4	10.32
762.8	9.34	702.5	10.33	703.2	10.49	702.5	10.10	702.5	9.86
		712.5	10.13	713.2	9.98	712.5	9.88	712.5	9.64
		722.6	9.57	723.6	9.67	722.6	9.37	722.6	9.35
		732.6	9.35	733.4	9.33	732.6	9.06	732.7	8.88
		742.7	8.83	743.8	8.89	742.7	8.54		

Table 3 Viscosity data of all melts re-equilibrated in the gas mixing furnace at $\log_{10} fO_2$ = -4 and -7 and data for PR-Leu-0.5Fe synthesised in air (error = ± 0.06 $\log_{10}$ Pa s) at given temperature (error = ± 0.5 °C)

	A [log_{10} Pa s]	B [K]	T_g^{12} [°C]	m
WPVe[1]	-14.80 ± 0.06	2.61 ± 0.01	700.4 ± 2.7	26.8
WPVe_NNO+3	-16.71 ± 0.04	2.81 ± 0.01	706.9 ± 2.7	28.7
WPVe_NNO	-15.68 ± 0.06	2.75 ± 0.01	719.5 ± 2.4	27.7
PN-0.5Fe[1]	-19.58 ± 0.19	3.19 ± 0.03	736.3 ± 3.5	31.6
PN-0.5Fe_NNO+3	-14.72 ± 0.32	2.63 ± 0.06	709.9 ± 5.9	26.7
PN-0.5Fe_NNO	-22.37 ± 0.06	3.26 ± 0.01	676.0 ± 1.1	34.4
PR-0.5Fe[1]	-22.52 ± 0.14	3.34 ± 0.02	694.2 ± 3.9	34.5
PR-0.5Fe_NNO+3	-16.68 ± 0.13	2.70 ± 0.02	669.6 ± 3.4	28.7
PR-0.5Fe_NNO	-22.42 ± 0.16	3.19 ± 0.02	653.4 ± 3.4	34.4
PR-Leu-0.5Fe	-30.16 ± 0.10	3.97 ± 0.01	668.0 ± 1.8	42.2
PR-Leu-0.5Fe_NNO+3	-30.87 ± 0.11	4.01 ± 0.01	662.0 ± 2.1	42.9
PR-Leu-0.5Fe_NNO	-29.49 ± 0.39	3.86 ± 0.05	657.2 ± 4.0	41.5

[1] from Kleest et al. (2020)

Table 4 Fit parameter for the Arrhenius Equation (Eq. 6), T_g^{12} and fragility m (Eq. 7)

Fragility

The fragility m is calculated by:

$$m = \frac{B*10^4}{T_g^{12}} \quad (7)$$

with B – parameter of the Arrhenius fit (Eq. 6) and T_g^{12} – the temperature at which the viscosity is 10^{12} Pa s in Kelvin and represents the deviation of a melt viscosity from the Arrhenian behaviour over wide ranging temperatures involving low and high viscosities (Toplis et al. 1997; Webb 2011). Determined fragilities are given in Table 4. It is lowest for the WPVe series (26.8 – 28.7) and highest for the PR-Leu-0.5Fe series (41.5 – 42.9). The PN-0.5Fe and PR-0.5Fe series have similar fragilities (26.7 – 34.5).

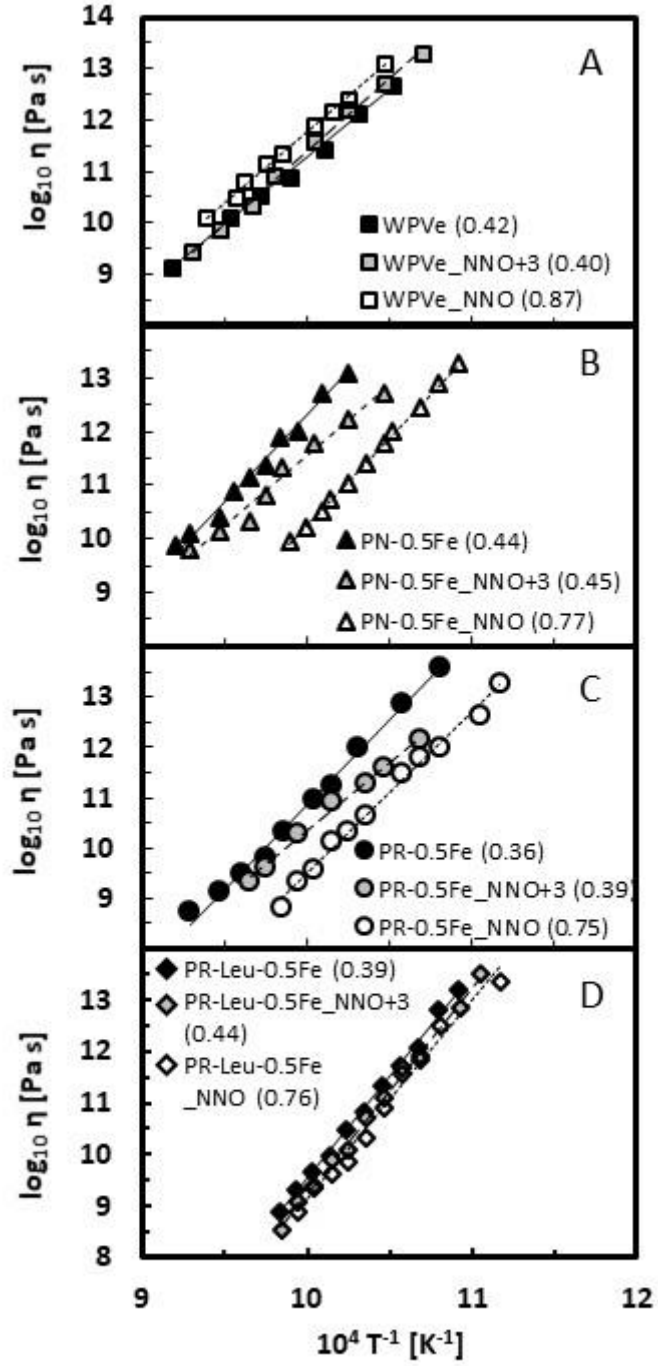

Fig. 3 Viscosities of the melts investigated in this study and those measured by Kleest et al. (2020) of A – the WPVe series, B – the PN-0.5Fe series, C – the PR-0.5Fe series and D – the PR-Leu-0.5Fe series. Fe^{2+}/Fe_{tot} of each melt is given in parenthesis. The overall effect of an increased Fe^{2+}/Fe_{tot} is a decrease in viscosity as seen in B, C and D. Note the deviation of this trend in the WPVe series (panel A), whose most reduced melt experienced loss of Fe and alkali and alkaline-earth elements.

Discussion

T_g^{12} (the temperature at which the viscosity is 10^{12} Pa s) for each melt are given in Table 4. Within each melt series, samples made in air and at $\log_{10} fO_2 = -4$ have nearly the same Fe^{2+}/Fe_{tot} within error as a consequence of the higher experimental temperatures at ambient atmosphere (Table 1). For these more oxidised melts of the WPVe series and PR-Leu-0.5Fe series, T_g^{12} differs by ~6 °C which is roughly within the error of ~3 °C. T_g^{12} of the more oxidised melts of the PN-0.5Fe series and PR-0.5Fe series equilibrated in air and at $\log_{10} fO_2 = -4$, both differ by ~25 °C despite identical Fe^{2+}/Fe_{tot} (Table 2) and same H_2O contents of ≤ 0.01 wt% (Table 1) within the series. ~2 vol% nanolites are formed in these melts during viscosity measurements. The measurements are performed by alternating high and low temperatures in order to observe possible increases in viscosity due to crystal growth in the melts. This process of nanolite growth is more pronounced in the melts made at $\log_{10} fO_2 = -4$ which would explain the different slopes of the Arrhenian fits (Fig. 3). This increase in crystallinity of these melts is calculated to increase viscosity by ~0.03 $\log_{10}$ Pa s (after Klein et al. 2018) and is therefore not further regarded since this value is within the ±0.06 $\log_{10}$ Pa s error of measurement. Hence, the differences in T_g^{12} for the oxidised melts of the PN-0.5Fe and PR-0.5Fe series are not clearly explainable.

The viscosity measurements were made in air, based on the assumption that the iron speciation would not change over the period of up to 8 hours at relatively low temperatures above T_g^{12} for the viscosity determination (Bouhifd et al. 2004; Stabile et al. 2016). During the measurements, Fe^{2+}/Fe_{tot} of the most reduced melts of each series slightly decreases by 0.03, 0.07, 0.06 and 0.08 for WPVe_NNO, PN-0.5Fe_NNO, PR-0.5Fe_NNO and PR-Leu-0.5Fe_NNO, respectively, indicating some oxidation occurred. However, this small decrease in Fe^{2+}/Fe_{tot} does not appear to affect the measured data as they do not alternate about or deviate from the straight line of the Arrhenian fit (Fig. 3).

Fig. 4 shows T_g^{12} vs Fe^{2+}/Fe_{tot} for all melts. Since Fe^{2+}/Fe_{tot} is mostly the same for the more oxidised melts, the average of T_g^{12} of these melts is used for comparison.

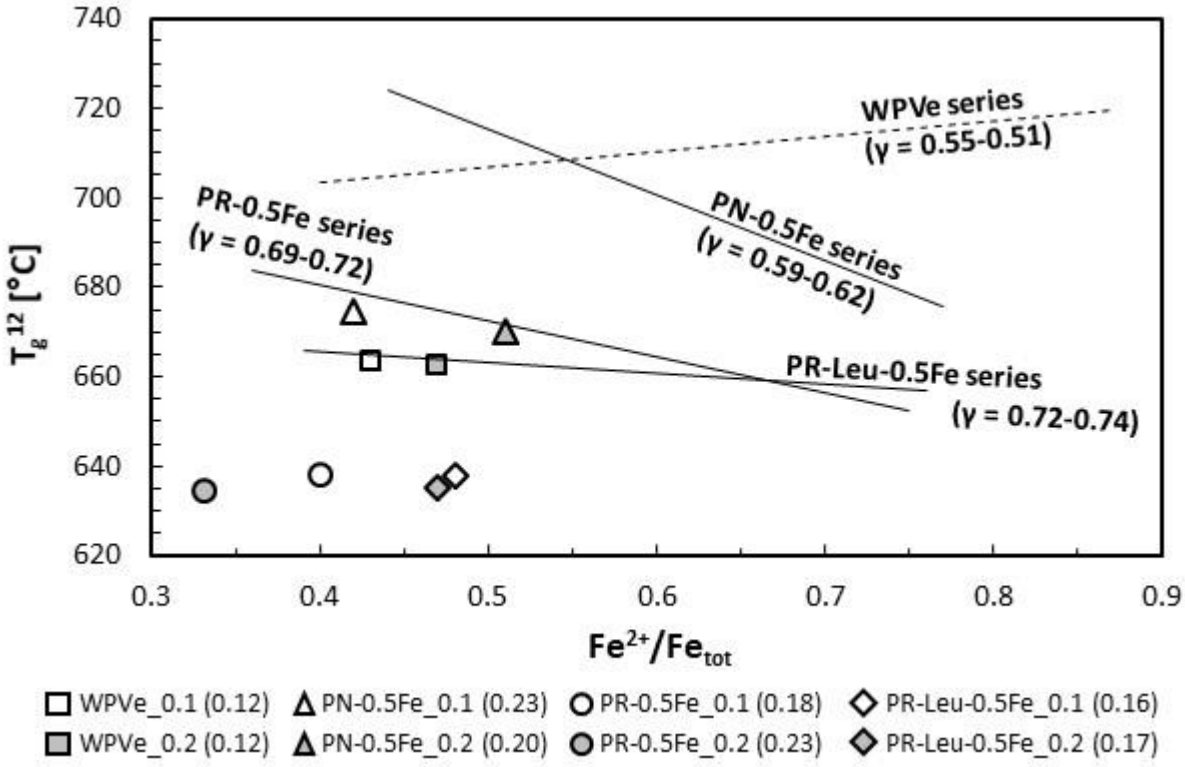

Fig. 4 T_g^{12} as a function of Fe^{2+}/Fe_{tot}. The lines represent the trend of the changes in T_g^{12} for the melts investigated in this study. The melt series are given at the lines and γ indicating the degree of polymerisation is given in parenthesis for each melt series in the order of more oxidised to the most reduced melts. The WPVe series gets more polymerised as a consequence of the loss of network modifiers although Fe^{2+}/Fe_{tot} increases. The CAVD melts get more depolymerised with elevated Fe^{2+}/Fe_{tot}. Furthermore, nominally anhydrous (< 0.5 wt% H_2O) melts of the same compositions from Kleest and Webb (2021) are added and H_2O concentrations are written in parenthesis in the legend. Note that symbols of the melts from Kleest and Webb (2021) do not plot on the trend line of the melt series to what they belong due to the elevated water contents.

The lines represent the changes in T_g^{12} between the more oxidised and the most reduced melts within each series. The decrease of T_g^{12} of ~50 °C is strongest for the PN-0.5Fe series with an increase of Fe^{2+}/Fe_{tot} from ~0.45 to 0.77. PR-0.5Fe has a T_g^{12} reduced by ~30 °C with an increase in Fe^{2+}/Fe_{tot} from ~0.38 to 0.75. An increase in Fe^{2+}/Fe_{tot} from 0.44 to 0.76 does not sufficiently affect T_g^{12} of the PR-Leu-0.5Fe melts since the difference of ~5 °C is within the ±4 °C error of T_g^{12}. An increased amount of Fe^{2+} results in an elevated Fe^{2+}/Fe_{tot} which is accompanied with a drop in T_g^{12}. These results are in agreement with the conventional assumption that Fe^{2+} behaves as a network modifier and hence, an increase in Fe^{2+}/Fe_{tot} includes an increased amount of network modifiers consequently increasing the degree of depolymerisation and hence decreases the viscosity of a melt (i.e. Dingwell 1991; Liebske et al. 2003; Stabile et al. 2016; Di Genova et al. 2017; Kolzenburg et al. 2018). The degree of

depolymerisation expressed by γ increases from 0.59 to 0.62, 0.69 to 0.72 and from 0.72 to 0.74 for the PN-0.5Fe series, the PR-0.5Fe series and the PR-Leu-0.5Fe series (Table 2), respectively, and consequently the viscosity decreases represented by T_g^{12} for these series (Fig. 4 and Table 4).

In contrast to the viscosity reducing effect of an elevated Fe^{2+}/Fe_{tot} for the PN-0.5Fe and PR-0.5Fe series, an increase of Fe^{2+}/Fe_{tot} from ~0.41 to 0.87 for the WPVe melts appears to increase T_g^{12} by ~15°C. This observation, indeed, is caused by structural changes due to the significant loss of Fe and network modifying alkalis and alkaline-earth elements resulting in a higher degree of polymerisation shown by a decrease in γ from 0.55 to 0.51 (Table 2). This overall decrease in network modifying elements affects the viscosity of the WPVe melts stronger than the relative increase of the network modifying Fe^{2+}.

As the total FeO content of the CAVD melts varies from ~6 wt% for the PN-0.5Fe and PR-Leu-0.5Fe series to ~7.5 wt% for the PR-0.5Fe series, the largest influence of Fe^{2+}/Fe_{tot} on T_g^{12} is expected for the PR-0.5Fe series with the highest Fe concentration. However, as pointed out in Fig. 4, the viscosity reducing effect introduced by an increase in Fe^{2+}/Fe_{tot} (illustrated by the slope of the lines) is most pronounced for the most polymerised melts of the PN-0.5Fe series followed by the less polymerised melts of the PR-0.5Fe series and minimises or even vanishes for the most depolymerised PR-Leu-0.5Fe melts (see γ in Table 2). Hence, the influence of the degree of polymerisation of the investigated melts on T_g^{12} is larger than the total FeO content. The original PR and PN melts contain ~9.5 wt% and ~7.3 wt% total FeO, respectively. The Fe^{2+}/Fe_{tot} determined for the synthetic melts with reduced Fe content in this study would lead to a further depolymerisation of the structure of the original melts with an increase in γ of 0.04 - instead of an increase in γ of 0.03 for the investigated equivalents having a lower Fe concentration. Consequently, the decrease in viscosity of the original melts due to an increase in Fe^{2+}/Fe_{tot} should be slightly larger than presented in this study.

The straight lines in Fig. 4 suggest a linear viscosity drop with increasing Fe^{2+}/Fe_{tot}. However, Dingwell (1991) and Liebske et al. (2003) demonstrated a nonlinear relation between viscosity reduction and increasing Fe^{2+}/Fe_{tot}. In the present study, it is not possible to state such a correlation since there are not enough data available.

Fe^{2+}/Fe_{tot} vs H_2O affecting viscosity

It is well known that H_2O in a melt reduces the viscosity. This effect is strongest within the first few amounts of H_2O and is more effective at low temperatures at which melts have high viscosities. Furthermore, this viscosity reducing effect is more intensive for more polymerised melts (i.e. Vetere et al. 2007; Misiti et al. 2011; Di Genova et al. 2013). Giordano et al. (2008) developed a model for the prediction of the temperature dependent viscosity of a melt as a function of the melt composition and volatiles including H_2O. However, this model does not consider the Fe ratio. Since the investigated melts of this study slightly vary in their H_2O contents the model from Giordano et al. (2008) (denoted GRD08 hereinafter) is used to estimate the influence of the H_2O concentrations of the melts to specify the sole influence of the increased Fe^{2+}/Fe_{tot} on the viscosity reduction.

After GRD08, an increase in the H_2O content from 0.01 to 0.03 wt% for the PN-0.5Fe melts (Table 1) decreases T_g^{12} by ~7 °C. The variations in H_2O concentrations from ~0.00 to 0.01 wt% as found in the PR-0.5Fe series and from 0.01 to 0.02 wt% within the PR-Leu-0.5Fe series, would lower T_g^{12} by ~3 °C which is within the error of T_g^{12} measurements and hence negligible. As a result, the observed drops in T_g^{12} of ~50 and ~30 °C for the PN-0.5Fe and PR-0.5Fe melt series, respectively, are mainly induced by the increases in Fe^{2+}/Fe_{tot} from ~0.40 to ~0.76.

The H_2O concentrations in the WPVe series differ between < 0.01 to 0.04 wt% (Table 1). After GRD08, this increase in H_2O would result in a decrease of T_g^{12} by ~10 °C. As discussed above, the measured increase in T_g^{12} is the consequence of changes to a more polymerised melt structure due to the loss of network modifiers which affects the viscosity more than the oppositional viscosity reducing influence of the increases in H_2O.

Kleest and Webb (2021) investigated the viscosities of melts of the same composition as in the present study with H_2O concentration up to 0.23 wt% and Fe^{2+}/Fe_{tot} ranging from 0.33 to 0.51 which are additionally shown in Fig. 4. These variations in the Fe ratio are not considered since the influence of H_2O clearly overruns the effects of these small differences in Fe^{2+}/Fe_{tot}. As obviously seen in Fig. 4, higher H_2O contents drastically reduce T_g^{12} of all melts. H_2O concentrations of 0.12 wt% in the WPVe_series decreases viscosity by ~40°C with respect to WPVe and WPVe_NNO+3. An addition of up to 0.22 wt% H_2O as given for the PN-0.5Fe and PR-0.5Fe melts from Kleest and Webb (2021) decreases T_g^{12} by ~50 and ~40 °C, respectively, in comparison with the melts made in air and at $\log_{10} fO_2 = -4$. This drop in T_g^{12} is slightly more as that caused by the increased Fe^{2+}/Fe_{tot} present in this study. Although the increase in H_2O is approximately the same for both melt series, the drop in T_g^{12} is more pronounced for the more polymerised melts of the PN-0.5Fe series than for the PR-0.5Fe melts (see γ in Table 2). The

PR-Leu-0.5Fe melts solely have a noticeable reduction in T_g^{12} of ~30 °C caused by H_2O concentrations up to 0.17 wt% whereas the increase in Fe^{2+}/Fe_{tot} has an insignificant influence on T_g^{12}. As a consequence, H_2O concentrations in the investigated melts are a crucial parameter when regarding viscosity. It is shown that even small amounts of H_2O up to 0.23 wt % reduce the viscosity more effectively than increases in Fe^{2+}/Fe_{tot} from ~0.41 to 0.76.

Conclusion

In the present study it has be shown that an increase in Fe^{2+}/Fe_{tot} decreases the viscosity of the tephri-phonolitic PN-0.5Fe and the foiditic PR-0.5Fe melts. An elevated Fe^{2+}/Fe_{tot} of the tephritic PR-Leu-0.5Fe series does not influence the viscosities of these samples significantly. Consequently, this viscosity reducing effect of increased Fe^{2+}/Fe_{tot} is more pronounced for the more polymerised PN-0.5Fe melts and appears to vanish for the least polymerised PR-Leu-0.5Fe melts. Samples of the WPVe series show an increase in T_g^{12}. This changes, however, are caused by the loss of Fe and network modifying alkalis and alkaline earth elements. Although the melts are nominally anhydrous, it is additionally pointed out that amounts of H_2O up to 0.23 wt% decrease the viscosity more effectively than an increase in Fe^{2+}/Fe_{tot} of these melts.

Acknowledgement

This research is enabled by the Deutsche Forschungsgemeinschaft with grant No. WE 1801/15-1. We are grateful to Dr. Burkhard Schmidt for his help with the gas mixing furnace and for the discussion of the FTIR spectra. We thank Dr. Andreas Kronz and Jochen Gätjen for their support at the electron microprobe. For the help with the colorimetric Fe determination we thank Bettina Schlieper-Ludewig and Andre Petitjean for the tricky sample preparation.

References

Behrens H, Misiti V, Freda C, Vetere F, Botcharnikov RE, Scarlato P (2009) Solubility of H_2O and CO_2 in ultrapotassic melts at 1200 and 1250 °C and pressure from 50 to 500 MPa. Am Mineral 94:105-120

Bigg PH (1967) Density of water in SI units over the range 0-40 °C. Brit J Appl Phys 18:521

Borisov A, Behrens H, Holtz F (2017) Effects of strong network modifiers on Fe3+/Fe2+ in silicate melts: an experimental study. Contrib Mineral Petrol 172:34

Bouhifd MA, Richet P, Besson P, Roskosz M, Ingrin J (2004): Redox state, microstructure and viscosity of a partially crystallized basalt melt. Earth Planet Sci Lett 218:31-44

Cottrell E and Kelley KA (2011) The oxidation state on Fe in MORB glasses and oxygen fugacity of the upper mantle. Earth Planet Sci Lett 3053:270-282

Dauphas N, Roskosz M, Alp EE, Neuville DR, Hu MY, Sio CK, Tissot FLH, Zhao J, Tissandier L, Médard E, Cordier C (2014) Magma redox and structural controls on iron isotope variations in Earth´s mantle and crust. Earth Planet Sci Lett 398:127-140

Deines P, Nafziger RH, Ulmer GC, Woermann E (1974) Temperature-oxygen fugacity tables for selected gas mixtures in the system C-H-O at one atmosphere total pressure. Bull Earth Mineral Sci, experimental station, 88:1-129

Di Genova D, Romano C, Alletti M, Misiti V, Scarlato P (2014) The effect of CO_2 and H_2O on Etna and Fondo Riccio (Phlegrean Fields) liquid viscosity, glass transition temperature and heat capacity. Chem Geol 377:72-86

Di Genova, Romano C, Hess KU, Vona A, Poe BT, Giordano D, Dingwell DB, Behrens H (2013) The rheology of peralkaline rhyolites from Pantelleria Island. J Volcanol Geotherm Res 249:201-216

Di Genova D, Vasseur J, Hess KU, Neuville DR, Dingwell DB (2017) Effect of oxygen fugacity on the glass transition, viscosity and structure of silica- and iron-rich magmatic melts. J Non-Cryst Solids 470:78-85

Dingwell DB (1991) Redox viscometry of some Fe-bearing silicate melts. Am Mineral 76:1560-1562

Dingwell DB, Knoche R, Webb SL (1992) The effect of B_2O_3 on the viscosity of haplogranitic liquids. Am Mineral 77:457-461

Einstein A (1906) Eine neue Bestimmung der Moleküldimensionen. Annals Phys 19:289-306

Freda C, Gaeta M, Giaccio B, Marra F, Palladino DM, Scarlat P, Sottili G (2011) CO_2-driven large mafic explosive eruptions: the Pozzolane Rosse case study from the Colli Albani Volcanic District (Italy). Bull Volcanol 73:241-256

Freda C, Gaeta M, Karner DB, Marra F, Renne PR, Taddeucci J, Scarlato P, Christensen JN, Dallai L (2006) Eruptive history and petrologic evolution of the Albano multiple maar (Alban Hills, Central Italy). Bull Volcanol 68:567-591

Gaeta M, Di Rocco T, Freda C (2009) Carbonate Assimilation in Open Magmatic Systems: the Role of Melt-bearing Skarns and Cun´mulate-forming Processes. J Petrol 50:361-385

Gaillard F, Schmidt B, Mackwell S, McCammon C (2003) Rate of hydrogen-iron redox exchange in silicate melts and glasses. Geochim et Cosmochim Acta 67:2427-2441

Giordano D, Russell JK, Dingwell DB (2008) Viscosity of magmatic liquids: A model. Earth Planet Sci Lett 271:123-134

Iacono-Marziano G, Gaillard F, Pichavant M (2007a) Limestone assimilation and the origin of CO_2 emissions at the Alban Hills (Central Italy): constraints from experimental petrology. J Volcanol Geotherm Res 166:91-105

Iacono Marziano G, Schmidt BC, Dolfi D (2007b) Equilibrium and disequilibrium degassing of a phonolitic melt (Vesuvius AD 79 “white pumice”) simulated by decompression experiments. J Volcanol Geotherm Res 161:151-164

Kleest C and Webb SL (2021) Influence of CO_2 on the rheology of melts from the Colli Albani Volcanic District (Italy) – foidite to phonolite. Contrib Mineral Petrol 176:92

Kleest C, Webb SL, Fanara S (2020) Rheology of melts from the Colli Albani Volcanic District (Italy): a case study. Contrib Mineral Petrol 175:82

Klein J, Mueller SP, Helo C, Schweitzer S, Gurioli L, Castr JM (2018) An expanded model and application of the combined effect of crystal-size distribution and crystal shape on the relative viscosity of magmas. J Volcanol Geotherm Res 357:128-133

Knipping JL, Behrens H, Wilke M, Göttlicher J, Stabile P (2015) Effect of oxygen fugacity on the coordination and oxidation state of iron in alkali bearing silicate melts. Chem Geol 411:143-154

Kolzenburg S, Di Genova D, Giordano D, Hess KU, Dingwell DB (2018) The effect of oxygen fugacity on the rheological evolution of crystalizing basaltic melts. Earth Planet Sci Lett 487:21-32

Kress VC and Carmichael ISE (1988) Stoichiometry of the iron oxidation reaction in silicate melts. Am Mineral 73:1267-1274

Kress VC and Carmichael ISE (1991) The compressibility of silicate liquids containing Fe_2O_3 and the effect of composition, temperature, oxygen fugacity and pressure on their redox state. Contrib Mineral Petrol 108:82-92

Liebske C, Behrens H, Holtz F, Lange RA (2003) The influence of pressure and composition on the viscosity of andesitic melts. Geochim et Cosmochim Acta 67:473-485

Misiti V, Vetere F, Freda C, Scarlato P, Behrens H, Mangiacarpa A, Dingwell DB (2011) A general viscosity model of Campi Flegrei (Italy) melts. Chem Geol 290:50-59

Ohlhorst S, Behrens H, Holtz F (2001) Compositional dependence of molar absorptivities of near-infrared OH- and H_2O bands in rhyolitic to basaltic glasses. Chem Geol 174:5-20

Ottonello G, Moretti R, Marini L, MV Zuccolini (2001) Oxidation state of iron in silicate glasses and melts: a thermochemical model. Chem Geol 174:157-179

Pocklington HC (1940) Rough measurement of high viscosities. Proc Cambridge Phil Soc 36:507-508

Presnall DC and Brenner NL (1974) A method for studying iron silicate liquids under reducing conditions with negligible iron loss. Geochim et Cosmochim Acta 88:1785-1788

Roscoe R (1952) The viscosity of suspensions of rigid spheres. Br J Appl Phys 3:267-269

Schanofski M, Fanara S, Schmidt BC (2019) CO_2-H_2O solubility in K-rich phonolitic and leucititic melts. Contrib Mineral Petrol 174:52

Schuessler JA, Botcharnikov RE, Behrens H, Misiti V, Freda C (2008) Oxidation state of iron in hydrous phono-tephritic melts. Am Mineral 93:1493-1504

Stabile P, Webb S, Knipping JL, Behrens H, Paris E, Giuli G (2016) Viscosity of pantelleritic and alkali-silicate melts: Effect of Fe redox state and Na/(Na + K) ratio. Chem Geol 442:73-82

Stolper E (1982) Water in Silicate Glasses: An Infrared Spectroscopic Study. Contrib Mineral Petrol 81:1-17

Tobolsky AV and Taylor RB (1963) Viscoelastic properties of a simple organic glass. J Phys Chem 67:2439-2442

Toplis MJ, Dingwell DB, Hess K-U, Lenci T (1997) Viscosity, fragility and configurational entropy of melts along the join SiO_2-$NaAlSiO_4$. Am Mineral 82:979-990

Vetere F, Behrens H, Misiti V. Ventura G, Holtz F, De Rosa R, Deubener J (2007) The viscosity of shoshonitic melts (Vulcanello Peninsula, Aeolian Islands, Italy): Insight on the magma ascent in dikes. Chem Geol 245:89-102

Webb SL (2011) Configurational heat capacity and viscosity of (Mg, Ca, Sr, Ba)-Al_2O_3-SiO_2 melts. Eur J Mineral 23:487-497

Webb SL, Banaszak M, Köhler U, Rausch S, Raschke G (2007) The viscosity of Na_2O-CaO-Al_2O_3-SiO_2 melts. Eur J Mineral 19:681-692

Wilson AD (1960) The Micro-determination of Ferrous Iron in Silicate Minerals by a Volumetric and a Colorimetric Method. Analyst 85:823-827

5 Concluding remarks

To summarise the results presented in the previous Chapters, it is assumed that the CAVD melts PN-0.5Fe, PR-0.5Fe as well as PR-Leu-0.5Fe – whose viscosities are determined as a function of CO_2 concentration and Fe speciation – are representative for the melt compositions with the original Fe content PN, PR and PR-Leu, respectively, and are discussed to behave as the original compositions.

Findings

To address the previously emerged questions, the main findings made in the present studies are:

- the viscosities of the PN and PR melts are not as low as assumed only based on the estimations from the TAS diagram due to their high content of the alkaline-earth elements,
- the enrichment of CaO as a consequence of the wall rock assimilation results in a decrease in melt viscosity,
- the CO_2 dissolved as CO_3^{2-} in the melts has a negligible to slightly reducing effect on the viscosity,
- the viscosity of the residual liquid melt PR-Leu decreases when leucite crystallises,
- a decrease in Fe^{2+}/Fe_{tot} of the melt as it rises from the magma chamber to the surface leads to an increase of the viscosity of the CAVD melts and
- even small amounts of H_2O drop the viscosity of the melts noticeably.

The studied PR melts demonstrate different stages of its magmatic evolution and the investigations of their rheological behaviour give the possibility to present a basic model of the processes causing the high explosivity of this event. In contrast, the compositions of the PN and WPVe melts represent one magmatic stage of these eruptions only and therefore, it is not possible to give a model of magma evolution of these volcanic events.

Evolution of the PR melt viscosity

Based on the data presented here, the viscosity continuously decreases during the magma evolution from the composition of the uncontaminated magma – without any assimilation of the carbonate wall rock (PR-CaO) – to the melt composition after contamination by the carbonate host rock in which the magma chamber is embedded (PR) to the residual liquid after the crystallisation of 4 mol% leucite (PR-Leu): as a consequence of the enrichment in the network modifying component CaO due to the assimilation of the carbonate wall rock, the viscosity of the PR melt decreases. Since CaO is not that effective in reducing the contaminated melt viscosity as alkalis, the viscosities are not that low as assumed based on the TAS diagram only, without considering alkaline-earth elements. A further critical feature for an estimation of the melt viscosity is the Fe speciation especially for Fe-rich melt compositions as investigated in the present study since the Fe speciation changes during magma ascent with detectable influence on the melt viscosity as briefly discussed below.

The viscosity of the residual melt PR-Leu decreases additionally due to the depletion of the network forming components SiO_2 and Al_2O_3 caused by leucite crystallisation resulting in a more depolymerised melt structure. As shown by the determined viscosities, these reduced SiO_2 and Al_2O_3 concentrations of PR-Leu affect the viscosity stronger than the depletion of the network modifying K_2O also consumed by the formation of leucite crystals.

The given CO_2 concentrations of this study appear to decrease the viscosity of these melts minimal or even negligibly. In contrast, the increased fraction of the network forming ferric iron due to (some) oxidation of ferrous iron as the consequence of an increasing fO_2 during magma ascent results in an increase of the viscosity of the PR melt.

Hence, the addition of a CO_2-rich fluid with a concomitant decrease of Fe^{2+}/Fe_{tot} affect the melt oppositely during magma ascent. However, since the CO_2 effect on the viscosity of the PR melt seems to be small to negligible, the Fe oxidation due to increasing fO_2 affects the viscosity stronger than the incorporated CO_2 for Fe^{2+}/Fe_{tot} investigated in this study resulting in an increased viscosity at the eruptive temperature what needs additionally to be considered for an estimation of the explosive style of a volcanic event.

On the other hand, as soon as H_2O is incorporated into the melt, its viscosity is reduced noticeably. Although there are no indications for magmatic or meteorological H_2O that could drive the explosivity of the PR event during eruptive conditions (Marra et al. 2009 and references therein; Freda et al. 2011), even small amounts of H_2O affect the viscosity of the melts stronger than CO_2 or varying Fe^{2+}/Fe_{tot}.

The residual PR liquid after leucite crystallisation (PR-Leu) is the most depolymerised melt among the investigated ones and its viscosity is less affected by changes in the CO_2 concentration and Fe speciation.

PR melt viscosity vs PR eruption

Fig. 1 demonstrates a simplified scheme of the proposed processes within the magma during storage and ascent and possible reasons driving the explosivity of the PR eruption.

Assuming that progressive crystallisation of the magma leads to successive depolymerisation of the residual liquid, its viscosity continues to decrease what promotes uprising of bubbles and degassing. So, an early effusive emission of the low viscous melt is comprehensible documented by a thin and poorly vesiculated lava flow unit underlying the leucite-rich pyroclastic flow deposits emitted explosively during the following eruption (i.e. Marra et al 2009; Freda et al. 2011). The beginning lava effusion leads to a depressuration in the magma resulting in significant bubble formation since the CO_2 solubility decreases with decreasing pressure (i.e. Thibault and Holloway 1994; Schanofski et al. 2019). However, it can be assumed that bubbles already formed during magma storage over a long pre-eruptive period since the input of the CO_2-rich fluid by the assimilation of up to 15 wt% carbonate wall rock (Iacono-Marziano et al. 2007) exceeds the CO_2 solubility in a leucitic melt, i.e. ~0.85 wt% at 300 MPa (Schanofski et al. 2019).

The pyroclastic flow deposits of the explosive phase show leucite contents up to 60 vol% with euhedral and skeletal habit (Marra et al. 2009; Freda et al. 2011) demonstrating crystal growth during magma storage as well as syn-eruptive leucite formation, respectively. A crystallinity of 0.6 is the critical value (at least for spherical crystals) at which a melt changes its rheological "viscous state" to a "rigid solid state" (i.e. Marsh 1981). Consequently, it can be assumed that this crystal-rich melt acts like a highly viscous to an even solid plug at the top of the magma chamber preventing further magma emission. The extensive bubble formation due to the sudden depressuration after the first lava emission induces an overpressure within the magma body accompanied by an increase of the magma volume and an upward movement of the bubbles due to its lower density.

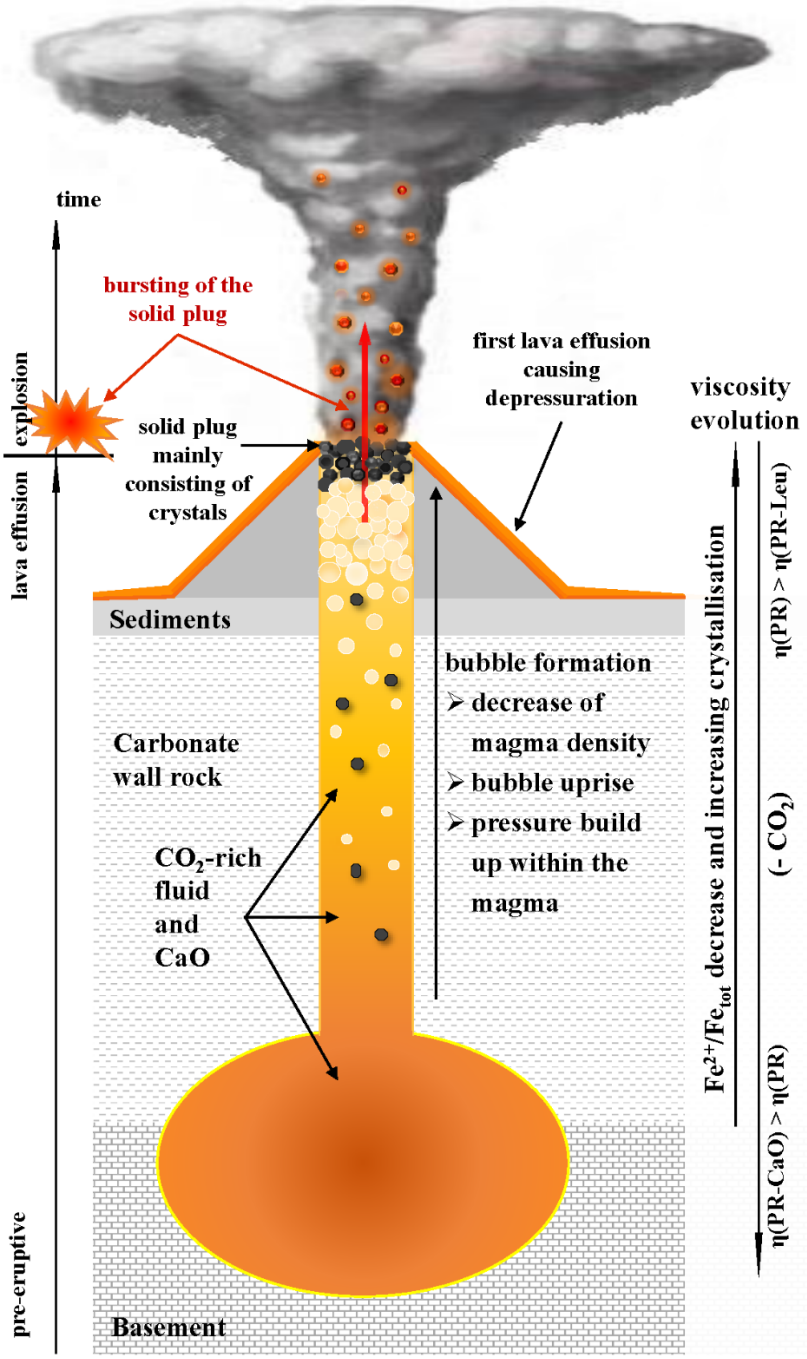

Fig. 1 Simplified scheme of possible processes within the PR magma leading to an explosive eruption. The heights and lengths of geological sequences and magmatic edifice are roughly shown without spatial scaling to emphasise the suggested processes causing the explosivity of this eruption! The presence of bubbles (light circles), crystals (dark symbols) and lava fragments (reddish to red symbols) and their locations are not complete and the exact temporal and spatial conditions are not given. At the surface - above the sediments -, two magmatic stages are demonstrated: 1st: the solid plug at the top of the conduit after the first lava emission that hinders further effusive lava emission and, 2nd: the failure of this solid plug due to the pressure in the magma caused by upward moving bubbles and its explosive shooting out of the vent (red arrow in the middle of the conduit and the volcanic column). The column on the right sight shows effects on viscosity during magmatic processes in meaning of "increase" or "decrease" with the highest viscosity at the arrowhead. The eruption column is redrawn after Science History Images/Alamy Stock Foto, Fig.-ID: G157EW from the photograph Spencer Sutton.

Consequently, the plug formed by the crystal-rich magma was shot out explosively of the vent by the escaping bubbles fragmentating the lava during the eruption. Since the assimilation and decarbonation of the wall rock takes place even during the eruption (Freda et al. 2008; Freda et al. 2011), the magma is continuously supplied with free CO_2, forming bubbles and building up pressure within the melt feeding the explosive style of the eruption.
Consequently, the magma of the PR eruption is a three-phase-system consisting of solid crystals (i.e. leucite), a liquid residual melt (i.e. PR-Leu) and a gaseous CO_2-rich fluid. The interaction of these three components with a low viscous residual liquid, a dramatic viscosity increase by the crystals and the overpressure induced by the volatile phase climaxes in a highly violent explosion erupting a large volume of pyroclastic material.

Outlook

During the research of the presented study, some questions could not be answered completely while others came up. For a better understanding of the sources causing the explosive style of the PN and PR eruptions, more detailed studies are necessary:

- how do greater amounts of CO_2 affect the viscosity up to the maximal soluble concentration of CO_2 in these tephri-phonolitic and foiditic melts, respectively?
- however, what is the CO_2 solubility in the residual melt after leucite crystallisation (PR-Leu) and how does this CO_2 content influence the residual melt viscosity?
- how large is the viscosity increasing effect of the crystal content that is found in the pyroclastic flow deposits of the PN and PR melts?
- how does the crystallisation of further solid phases besides leucite found in the pyroclastic flow deposits (i.e. clinopyroxene (Freda et al. 2011)) influence the viscosity of the PN and PR magmas?
- what is the influence of the latent heat induced by the extensive crystallisation on the melt viscosity,
- how do further Fe ratios caused by changing fO_2 affect the viscosity of the melts during magma ascent?
- what is the Fe ratio and its influence of the melt viscosity at the eruptive temperatures?
- and, in particular, how do different amounts of bubbles influence the viscosity of these melts and what is their effect on the eruption styles of the volcanic PN and PR events?

But not only geological demands remain, also experimental and methodological questions appeared during the research that need to be clarified.

1) Some glasses whose viscosity should be measured as a function of CO_2 concentration contained bubbles. To determine the influence of CO_2 on the viscosities of these melts only – without estimating the bubble effect by the means of models – it is necessary to synthesise them bubble free.
2) Other CO_2 bearing but bubble free glasses disintegrated during viscosity measurements or foamed during DSC measurements before reaching the temperature of interest preventing determination of the viscosity or heat capacities in the T_g range, respectively. It is a challenge to avoid these effects during these measurements to get reliable data.
3) The re-equilibrated Fe ratio of the more depolymerised melts PN-0.5Fe, PR-0.5Fe and PR-Leu-0.5Fe was observed after 20 h in the gas mixing furnace at the given conditions within the whole sample. In contrast, the same conditions were not sufficient to reach a homogeneous re-equilibrium of the Fe speciation within the most polymerised melt WPVe. Hence, an experimental series of varying experimental conditions could improve the recent understanding of the kinetics of those melts.

References

Freda C, Gaeta M, Giaccio B, Marra F, Palladino DM, Scarlat P, Sottili G (2011) CO_2-driven large mafic explosive eruptions: the Pozzolane Rosse case study from the Colli Albani Volcanic District (Italy). Bull Volcanol 73:241-256

Freda C, Gaeta M, Misiti V, Mollo S, Dolfi D, Scarlato P (2008) Magma-carbonate interaction: An experimental study on ultrapotassic rocks from Alban Hills (Central Italy). Lithos 101:397-415

Iacono-Marziano G, Gaillard F, Pichavant M (2007) Limestone assimilation and the origin of CO_2 emissions at the Alban Hills (Central Italy): constraints from experimental petrology. J Volcanol Geotherm Res 166:91-105

Marra F, Karner DB, Freda C, Gaeta M, Renne P (2009) Large mafic eruptions on Alban Hills Volcanic District (Central Italy): Chronostratigraphy, petrography and eruptive behaviour. J Volcanol Geotherm Res 179:217-232

Marsh BD (1981) On the crystallinity, probably occurrence, and rheology of lava and magma. Contrib Mineral Petrol 78:85-98

Schanofski M, Fanara S, Schmidt BC (2019) CO_2-H_2O solubility in K-rich phonolitic and leucititic melts. Contrib Mineral Petrol 174:52

Science History Images:
www.alamy.de/stockfoto-typen-von-vulkanausbruchen-vulkanianische-eruption-eine-kurze-heftige-relativ-kleine-explosion-der-zahflussigen-magma-die-eruption-ergibt-sich-aus-der-explosion-eines-steckers-aus-lava-in-einem-vulkanischen-rohr-oder-der-bruch-des-lava-dome-plinianische-eruption-grosste-103992529.html

Thibault Y and Holloway JR (1994) Solubility if CO_2 in a Ca-rich leucitie: effects of pressure, temperature and oxygen fugacity. Contrib Mineral Petrol 116:216-224